



HAL
open science

Novel materials for electrochemical energy storage in supercapacitors.

Sergey N. Pronkin

► **To cite this version:**

Sergey N. Pronkin. Novel materials for electrochemical energy storage in supercapacitors.. Material chemistry. Université de Strasbourg, 2021. tel-03836909

HAL Id: tel-03836909

<https://theses.hal.science/tel-03836909v1>

Submitted on 2 Nov 2022

HAL is a multi-disciplinary open access archive for the deposit and dissemination of scientific research documents, whether they are published or not. The documents may come from teaching and research institutions in France or abroad, or from public or private research centers.

L'archive ouverte pluridisciplinaire **HAL**, est destinée au dépôt et à la diffusion de documents scientifiques de niveau recherche, publiés ou non, émanant des établissements d'enseignement et de recherche français ou étrangers, des laboratoires publics ou privés.



Distributed under a Creative Commons Attribution 4.0 International License



Novel materials for electrochemical energy storage in supercapacitors

Garant: Dr. Cuong Phamm-Huu (ICPEES)

Sergey N. Pronkin

A thesis presented for the degree of
Habilitation of Research

Institute of Chemistry and Processes for Energy, Environment,
and Health (ICPEES), UMR-7515
University of Strasbourg, France

JURY

Prof. Aziz Dinia, IPCMS, Strasbourg
Dr. Frederick Favier, ICGM, Montpellier
Dr. Camélia Matei Ghimbeu, IS2M, Mulhouse
Prof. Philippe Serp, ENSIACET, Toulouse
Dr. Katia Araujo Da Silva, ICCF, Clermont-Ferrand

*Hat man sein **warum?** des Lebens,
so verträgt man sich fast mit jedem **wie?***

*One who has his **Why?** in life,
will overcome any **How?***

FREIDRICH NIETZCHE, 1888

Contents

Summary of the work	4
Lists of variables, constants, and abbreviations	8
Author's Curriculum Vitae	11
Introduction	19
1 Electrochemical energy storage	24
1.1 Electrochemical energy storage devices	24
1.2 Supercapacitors	28
1.2.1 Electrode-electrolyte interface	29
1.2.2 Electrochemical double-layer capacitors	34
1.2.3 Phenomena of pseudocapacitance	37
1.2.4 Pseudocapacitors and ion-insertion batteries	43
1.3 Impedance of electrochemical electrode/electrolyte interface	45
1.3.1 Impedance of the flat electrode/electrolyte interface.	47
1.3.2 Models of impedance of rough electrode/electrolyte interface	49
1.3.3 Generalized staircase model of impedance of porous electrode materials.	53
1.4 Conclusions	70
2 Carbon electrode materials	74
2.1 0D-carbon	75
2.2 1D-carbon	76
2.3 2D-carbon	77
2.3.1 Chemical exfoliation of graphite	78
2.3.2 Sonochemical exfoliation of graphite	80
2.3.3 Graphene-like carbon in supercapacitors	81
2.3.4 Case study: Graphene-like carbon from sugar/salt mixture	82
2.4 3D-carbon	85
2.4.1 Case study: activated carbon from ripe fig fruit	87
2.5 Conclusions	91

3	Transition Metal Oxide (TMO) electrode materials	93
3.1	General aspects	93
3.2	Conductivity of TMO	98
3.3	Electrochemical stability and structural integrity of TMO	106
3.3.1	TMO stable in wide pH range: RuO ₂ , TiO ₂	108
3.3.2	TMO stable in acidic pH: oxides of W and Mo	110
3.3.3	TMO stable in neutral and weak alkaline pH: oxides of Mn, Fe, Co, Ni	112
3.3.4	Impedance of porous electrode/electrolyte interface with pseudo- capacitive behavior	129
3.4	Conclusions	131
4	Future projects	134
4.1	Bio-sourced activated carbon	135
4.2	TMO/C composite materials	136
4.3	Electrochemical study of supercapacitors performance	138
	Acknowledgements	140

Summary of the work

Abstract (English)

Transition toward energy systems based on the renewable primary sources, such as solar energy and wind, is a pressing challenge of our time. Considering an intermittent character of these sources, the efficient and reversible energy storage devices are the crucial components of future energy grids. Electrochemical energy storage devices (EESD), namely batteries, supercapacitors, and hybrid cells, offer high reversibility and efficiency of energy storage, compact structure, and zero operation emission. The performance of EESD strongly depends on the properties of electrode materials, in particular on their specific energy density, electronic and ionic conductivities, specific surface area (SSA), its surface interaction with an electrolyte. Electrode materials should be electrochemically stable and keep structural integrity upon charging/discharging cycles. Finally, from the viewpoint of sustainable development, the main components of these materials should be fabricated from relatively abundant and preferably non-toxic sources.

Two classes of materials play a key role for EESD: carbon materials and transition metal oxides (TMO). The present work has a goal to analyze the dependence of the performance of these materials as electrodes for supercapacitors on their structural properties in order to (i) point out the key determining parameters and (ii) offer a guidelines for further development of electrode materials.

After brief introduction in the Chapter , the principles of electrochemical energy storage in supercapacitors are considered in the Chapter 1. Main types of mechanisms of charge storage, namely, charging of interfacial double layer and pseudocapacitance are discussed. The differences between two main classes of supercapacitors, namely, electrochemical double layer capacitors (EDLCs) and pseudocapacitors, are presented. The criteria discerning the performance of electrode materials in supercapacitors and ion intercalation batteries are outlined. Finally, the model of an impedance of porous electrode materials is presented, and influence of various structural parameters on the

electrochemical properties of materials is evaluated.

In the Chapter 2, carbon electrode materials are considered for supercapacitor application. Their main advantages (electronic conductivity, chemical stability, high SSA) and shortcomings (low surface specific capacitance) are highlighted. Carbon materials are classified by their geometry as 0D (nano-onions), 1D (nanotubes, nanofibers), 2D (graphene based) and 3D (activated carbon). Last two classes are considered in more details as the most promising candidates for supercapacitors. In particular, it is concluded that open porous structure with strong contribution of micropores and easy accessibility of electrolyte, as well as the presence of graphitic domains capable to host intercalated ions, are favorable for high capacitance of carbon electrodes.

In the Chapter 3, transition metal oxides (TMO) are presented as a materials for supercapacitors. The influence of their conductivity (both electronic and ionic) and electrochemical stability on their performance is evaluated. By analyzing Pourbaix diagrams of different metals, TMO are classified by their stability at different pH: oxides, stable at any pH (RuO_2 , TiO_2), stable at acidic pH (WO_3 , MoO_3), and stable at neutral/alkaline pH (oxides of Co, Fe, Mn). Particular attention is paid to the spinel oxides of Fe (Fe_3O_4) and Mn (Mn_3O_4). The strategies to improve the performance of TMO/C composites, namely preparation of substituted spinel oxides, are discussed.

Finally, in the chapter 4, main directions of further work in the field of electrode materials for supercapacitors are proposed.

- Development of bio-sourced and waste-sourced activated carbon materials with controlled porous structure.
- Solid state synthesis of ternary spinel oxides of type $\text{M}_x\text{Fe}_{2-x}\text{O}_4$, where $\text{M}=\text{Mn}^{2+}$, Ca^{2+} , Cu^{2+} , Zn^{2+} .
- Development of detailed model of an impedance of porous electrodes considering both micro- and macrostructure of electrode material.

Resume (Français)

La transition vers des systèmes énergétiques basés sur des sources primaires renouvelables, telles que l'énergie solaire et l'énergie éolienne, est un défi urgent de notre époque. Compte tenu du caractère intermittent de ces sources, les dispositifs de stockage d'énergie efficaces et réversibles sont les composants essentiels des futurs réseaux énergétiques. Les dispositifs de stockage d'énergie électrochimique (EESD), à savoir les batteries, les supercondensateurs et les cellules hybrides, offrent une réversibilité et une efficacité du stockage d'énergie élevées, une structure compacte et une zéro émission de fonctionnement. Les performances de ces dispositifs dépendent fortement des propriétés des matériaux d'électrode, en particulier de leur densité d'énergie spécifique, conductivités électronique et ionique, surface spécifique (SSA) et l'interaction de surface avec un électrolyte. Les matériaux d'électrodes doivent être électrochimiquement stables et conserver leur intégrité structurale lors des cycles de charge/décharge. Enfin, du point de vue du développement durable, les principaux composants de ces matériaux doivent être fabriqués à partir de sources relativement abondantes et de préférence non toxiques.

Deux classes de matériaux jouent un rôle clé pour les EESD : les matériaux en carbone et les oxydes de métaux de transition (TMO). Le présent travail a pour but d'analyser la dépendance des performances de ces matériaux en tant qu'électrodes pour supercondensateurs par rapport à leurs propriétés structurales afin (i) de mettre en évidence les paramètres déterminants et (ii) d'offrir des lignes directrices pour le développement futur des matériaux d'électrode.

Après une brève introduction dans le chapitre , les principes du stockage d'énergie électrochimique dans les supercondensateurs sont examinés dans le chapitre 1. Les principaux types de mécanismes de stockage de charge, à savoir la charge de la double couche interfaciale et la pseudocapacitance, sont discutés. Les différences entre les deux principales classes de supercondensateurs, à savoir les condensateurs à double couche électrochimique (EDLC) et les pseudocondensateurs, sont présentées. Les critères permettant de discerner les performances des matériaux d'électrode dans les supercondensateurs et les batteries à intercalation ionique sont exposés. Enfin, le modèle d'impédance des matériaux d'électrode poreux est présenté, et l'influence de divers paramètres structurels sur les propriétés électrochimiques des matériaux est évaluée.

Dans le chapitre 2, les matériaux d'électrode en carbone sont considérés pour l'application de supercondensateurs. Leurs principaux avantages (conductivité électronique, stabilité chimique, SSA élevée) et inconvénients (faible capacité spécifique de surface) sont mis en évidence. Les matériaux en carbone sont classés selon leur géométrie : 0D (nano-

oignons), 1D (nanotubes, nanofibres), 2D (carbon à base de graphène) et 3D (carbon actif). Les deux dernières classes sont considérées plus en détail comme les candidats les plus prometteurs pour les supercondensateurs. En particulier, il est conclu que la structure poreuse ouverte avec une forte contribution des micropores et une accessibilité facile de l'électrolyte, ainsi que la présence de domaines graphitiques capables d'accueillir des ions intercalés, sont favorables à une capacité élevée des électrodes de carbone.

Dans le chapitre 3, les oxydes de métaux de transition (TMO) sont présentés comme des matériaux pour les supercondensateurs. L'influence de leur conductivité (électronique et ionique) et de leur stabilité électrochimique sur leurs performances est évaluée. En analysant les diagrammes de Pourbaix de différents métaux, les TMO sont classés selon leur stabilité à différents pH : oxydes, stables à tout pH (RuO_2 , TiO_2), stables à pH acide (WO_3 , MoO_3), et stables à pH neutre/alcalin (oxydes de Co, Fe, Mn). Une attention particulière est accordée aux oxydes spinelles de Fe (Fe_3O_4) et de Mn (Mn_3O_4). Les stratégies visant à améliorer les performances des composites TMO/C, à savoir la préparation d'oxydes de spinelle substitués, sont discutées.

Enfin, dans le chapitre 4, les principales directions des travaux futurs dans le domaine des matériaux d'électrode pour les supercondensateurs sont proposées.

- Développement de matériaux en charbon actif bio-sourcés et issus de déchets avec une structure poreuse contrôlée.
- Synthèse à l'état solide d'oxydes spinelles ternaires de type $\text{M}_x\text{Fe}_{2-x}\text{O}_4$, où $\text{M}=\text{Mn}^{2+}$, Ca^{2+} , Cu^{2+} , Zn^{2+} .
- Développement d'un modèle détaillé de l'impédance des électrodes poreuses prenant en compte la micro et la macrostructure du matériau de l'électrode.

Preamble

List of general variables

- A - surface area, cm^2
 C_g - mass specific capacitance, F/g
 C_s - surface specific capacitance, $\mu\text{F}/\text{cm}^2$
 C_V - volume specific capacitance, F/cm^3
 C_{dl} - capacity of interfacial double layer, F
 C_i - concentration of i^{th} -component in solid or in electrolyte, mol/cm^3
 C_p - specific heat capacitance, $\text{J} \cdot \text{mol}^{-1} \cdot \text{K}^{-1}$
 d - diameter of particles, or pores, m
 D - diffusion coefficient, cm^2/s
 m - mass of an electrode material, g
 Q_c - maximal theoretical charge storage, C/g
 E - mass specific energy density, W.h/kg
 E - electrode potential, V
 f - AC modulation frequency, Hz
 I - current passing through electrode, A
 \vec{I} - AC modulated interfacial current, A
 i - surface specific current density, A/cm^2 ⁽¹⁾
 i_m - mass specific current density, A/g
 l - length of a pore, m
 \vec{E} - AC-modulated electrode potential, V
 P - mass specific power density, W/kg
 R - serial resistance, Ohm
 SSA - mass specific surface area, m^2/g

¹ i is also an imaginary unit in the equations related to electrochemical impedance

T - temperature, K
 V - voltage of operation of a supercapacitor device, V
 v - linear potential modulation rate, mV/s
 \vec{Z} - electrochemical interfacial impedance, Ohm
 δ - intercalation factor (stoichiometric to oxide structural unit)
 ρ - material density, g/cm³
 ω - angular frequency, rad/s
 σ - conductivity, Ohm⁻¹.cm⁻¹
 ϕ - phase shift angle between potential stimulus \vec{E} and signal \vec{I}

List of constants

$F = 96498$ C/mol - the Faraday constant
 $\epsilon_0 \approx 8.854187 \cdot 10^{-12}$ F/m - the vacuum permittivity
 $R = 8.314$ J/mol.K - the universal gas constant

List of abbreviations

AC - Activated Carbon
BET - Brunauer-Emmet-Teller (referred to the method of SSA measurements based on BET adsorption isotherm)
CV - Cyclic Voltammetry
EDL - Electrical Double Layer
EDLC - Electrochemical Double Layer Capacitor
EESD - Electrochemical Energy Storage Devices
EIS - Electrochemical Impedance Spectroscopy
GCPL - Galvanostatic Cycling with Potential Limits
IHP - Inner Helmholtz Plane
NHE - Normal Hydrogen Electrode
OHP - Outer Helmholtz Plane
ORR - Oxygen Reduction Reaction
PEDOT:PSS - poly(3,4-ethylenedioxythiophene) polystyrene sulfonate polymers mixture
PZC - Potential of Zero Charge
PVA - Polyvinyl alcohol

SEM - Scanning Electron Microscopy
SSA - Specific Surface Area
TMO - Transition Metal Oxides
TEM - Transmission Electron Microscopy
XPS - X-ray Photoelectrons Spectroscopy
XRD - X-ray diffraction

Author's Curriculum Vitae

Academic degree:	Dr.
Academic rank:	Assistant Professor (Maître de Conférence)
Name:	Sergey Pronkin
E-Mail:	sergey.pronkin@unistra.fr
Date and place of birth:	17.05.1976 in Moscow, Russia
Citizenship:	Russian
Current position:	Assistant Professor (Maître de Conférence) in the European Engineering School of Chemistry, Polymers and Materials, University of Strasbourg (ECPM-Unistra), Strasbourg, France
Current teaching affiliation:	European Engineering School of Chemistry, Polymers and Materials, University of Strasbourg (ECPM-Unistra), Strasbourg, France
Current research affiliation:	Institute of Chemistry and Processes for Energy, Environment and Health (ICPEES), Strasbourg, France

Professional experience

September 2009 – now	Assistant Professor in the European Engineering School of Chemistry, Polymers and Materials, University of Strasbourg (ECPM-Unistra) / Institute of Chemistry and Processes for Energy, Environment and Health (ICPEES), Strasbourg, France
-------------------------	---

February 2007 –
August 2009

Researcher in the group of Prof. Dr. Elena Savinova, Laboratory of Materials, Surfaces and Processes for Catalysis (LM-SPC) (now Institute of Chemistry and Processes for Energy, Environment and Health (ICPEES)), Strasbourg, France
Research topic: "Spatially ordered arrays for fuel cell reactions"

May 2005 –
January 2007

Post-doctoral researcher in the group of Electrocatalysis and Fuel Cells of Prof. Dr. Elena Savinova, Boreskov Institute of Catalysis, Novosibirsk, Russia
Research topic: "Electrochemistry and electrocatalytic properties of supported Pd mono- and bimetallic nanoparticles"

October 2001 –
March 2005

Post-doctoral researcher (Humboldt fellowship 2001-2003) in Electrochemistry group of Priv. Doz. Th. Wandlowski, Institute of Thin Films and Interfaces, Research Center Jülich, Jülich, Germany
Research topic: "Nanostructured Pd, Rh and Pt electrodes as model systems for the search of structural effects in electrocatalysis"

Highest educational degree

PhD in Electrochemistry, 2000, Department of Electrochemistry, Moscow State University, Moscow, Russia. Thesis "The nanostructure of platinum electrocatalysts and their electrochemical properties".

Supervisor: Prof. Galina A. Tsirlina

Other educational degree

University degree in higher education and teaching (Diplôme d'Université Pédagogie dans l'Enseignement Supérieur), 2018, University of Strasbourg. Thesis "Modification of a course of chemical kinetics to hybrid format: advantages and challenges".

Scientific publications

Book chapters	2
Scientific papers	40
Current h-factor:	23 (Web of Science)
Web of Science ResearcherID:	A-7395-2010
ORCID ID:	0000-0002-6981-7831

Scientific interests

Electrochemical material science:

preparation and electrochemical characterization of composite electrode materials,
electrodeposition,
anodization,
impedance spectroscopy

Electrochemical energy storage devices:

supercapacitors,
metal oxide / carbon / polymer composites

Electrocatalysis:

bimetallic catalysts,
metal-support interaction,
kinetics of electrocatalytic processes,
FTIR spectroelectrochemistry

Tutorship

Co-tutorship of PhD students:

Xiong Zhang, ICPEES, 2019 – now, co-tutorship with Dr. Pham-Huu Cuong

Wei Wang, ICPEES, 2016-2019, co-tutorship with Dr. Pham-Huu Cuong

Pierre-Alexandre Gross, ICPEES, 2010-2013, co-tutorship with Dr. Valerie Keller and Prof. Elena Savinova

Tutorship

Tutorship of master students:

Emilie Rojtmann, National High School of Chemistry of Mulhouse, Mulhouse, France, April 2021 – August 2021 (Project COM-Gra, M1 internship)

Boya Wu, University of Strasbourg, Strasbourg, France, February 2020 – July 2020 (Project COM-Gra, M2 internship)

Omar Rahmouni, Mohamed V University, Rabat, Morocco, February 2019 – July 2019 (Project ERASMUS-MediSol, M2 internship)

Ayoub Mahdi Elyaagoubi, Mohamed V University, Rabat, Morocco, February 2018 – July 2018 (Project ERASMUS-MediSol, M2 internship)

Mohhamed Salloma, Helwan University, Helwan, Egypt, September 2017 – February 2018 (Project ERASMUS-MediSol, M2 internship)

Pierre-Alexandre Gross, University of Strasbourg, Strasbourg, France, March 2009 – July 2009 (M1 internship), February 2010 – June 2010 (M2 internship)

Yeuk-Ting Law, University of Strasbourg, Strasbourg, France, March 2007 – July 2007 (M1 internship), February 2008 – June 2008 (M2 internship)

Authorship of Courses

Courses in European Engineering School of Chemistry, Polymers and Materials (ECPM), University of Strasbourg, Strasbourg, France:

- "Mathematics for chemists" for Classe Préparatoire Intégrée (integrated preparatory class)
- "Chemical kinetics", online (Moodle) course

Fellowships

2001 – 2003

Alexander von Humboldt foundation fellowship

Selected publications

Book chapters

1. Maillard F., Pronkin S.N., Savinova E.R. Influence of size on the electrocatalytic activities of supported metal nanoparticles in fuel cell-related reactions. In: Handbook of Fuel Cells (eds. Vielstich W., Gasteiger H.A., Yokokawa H.), Vol. 5, Chapter 7. Wiley, 2009
2. Maillard F., Pronkin S.N., Savinova E.R. Size Effects in Electrocatalysis of Fuel Cell Reactions on Supported Metal Nanoparticles. In: Fuel Cell Catalysis: a Surface Science Approach (eds. Koper M., Wieckowski A.). Wiley, 2009

Selected scientific papers

1. Ba H., Wang W., Pronkin S., Romero T., Baaziz W., Nguyen-Dinh L., Chu W., Ersen O., Pham-Huu C. Biosourced foam-like activated carbon materials as high-performance supercapacitors. *Advanced Sustainable Systems* 2018, 2, 1700123. <https://doi.org/10.1002/adsu.201700123>
2. Kéranguéven G., Faye J., Royer S., Pronkin S.N. Electrochemical properties and capacitance of Hausmannite Mn₃O₄ – carbon composite synthesized by in situ autocombustion method. *Electrochimica Acta* 2016, 222, 755-764. <https://doi.org/10.1016/j.electacta.2016.11.032>

3. Lopez L., Kim Y., Jierry L., Hemmerle J., Boulmedais F., Schaaf P., Pronkin S., Kotov N.A. Electrochemistry on stretchable nanocomposite electrodes: dependence on strain. ACS Nano 2018, 12, 9, 9223-9232. <https://doi.org/10.1021/acsnano.8b03962>
4. Pardieu E., Pronkin S., Dolci M., Dintzer T., Pichon B.P., Begin D., Pham-Huu C., Schaaf P., Begin-Colin S., Boulmedais F. Hybrid layer-by-layer composites based on a conducting polyelectrolyte and Fe₃O₄ nanostructures grafted onto graphene for supercapacitor application. Journal of Materials Chemistry A 2015, 3, 22877-22885. <https://doi.org/10.1039/C5TA05132K>
5. Ba H., Wang W., Tuci G., Pronkin S.N., Weinberg C., Nguyen-Dinh L., Giambastiani G., Pham-Huu C. Tridimensional few-layer graphene-like structures from sugar-salt mixtures as high-performance supercapacitor electrodes. Materials Today Energy 2018, 10, 118-125. <https://doi.org/10.1016/j.mtener.2018.08.015>

Scientific projects (2009 - now)

As project leader:

Project code	Project title	Funding agency	Duration	Total funding / funding of ICPEES
INFINE	"Synthesis and control of interactions in new fluorinated inorganic oxide-carbon nanocomposites for electrode materials design	ANR, France	2021-2025	501.6 kEuro / 155.9 kEuro ICPEES
MMO-Grace	"Mixed metal oxide / graphene composite electrode materials for electrochemical storage devices"	CNRS, France	2019	10 000 Euro (all ICPEES)

COM-Gra	"Metal oxide – graphene composites: new materials for supercapacitor electrodes"	MICA-Carnot, Alsace, France	2020	48 000 Euro / 26 000 Euro ICPEES
---------	--	-----------------------------	------	----------------------------------

As project participant:

Project code	Project title	Funding agency	Duration	Total funding / funding of ICPEES
ANR-06-CEXC-004-01	"Novel spatially ordered nanomaterials for the energy conversion"	ANR, France	2006-2009	799 000 Euro
EU-DEMMEA	"Understanding the degradation mechanisms of membrane-electrodeassembly for high temperature PEMFCs and optimization of individual components"	European Union	2008-2012	220 000 Euro
STEPPEES	"Nanotubes de TiO2 ordonnées pour le développement de photoanodes pour la production d'hydrogène sous illumination solaire"	CNRS, France	2008-2011	115 000 Euro
NIE	"Nanostructures en Interaction avec leur Environnement"	FRC, France	2012-2014	119 000 Euro
HELACAM	"Hydrogen electrocatalysis in alkaline media"	ERA-NET.RUS	2012-2014	30 000 Euro

PMNA	"Développement de la pile combustible H ₂ /O ₂ à membrane échangeuse d'anions à base de catalyseurs sans platine à basse température (30° – 80° C)"	Région Alsace, France	2013-2015	103 000 Euro
BioSenseDress	"Développement de biocapteurs enzymatiques nanofibreux: vers les pansements intelligents"	MICA, Alsace, France	2018	50 000 Euro

Introduction

Electrochemical energy storage devices (EESD), namely, batteries and supercapacitors, play ever growing role in the local and global energy networks. Their advantages are high reversibility and storage efficiency, compact versatile size and functioning with zero emission. Comparing to supercapacitors, batteries have higher energy storage capacities up to few 100 W.h/kg. It is due to a charge storage mechanism involving electrochemical reactions and cation intercalation into the bulk of the material of electrodes. In supercapacitors, a charge is stored at the interface between electrode and electrolyte or in its vicinity. This results in lower energy densities of supercapacitors, i.e. ca. 10-50 W.h/kg [1]. However, as interfacial charge storage process is significantly faster and more reversible than bulk electrochemical reaction, supercapacitors have (in comparison to batteries):

- faster charging time (from few min to few s),
- higher power output (ca. $1 - 10^2$ kW/kg),
- much better capacity retention in charging/discharging cycles (above 80% for more than 10^5 cycles),
- no memory effect.

Due to these advantages, supercapacitors are used as power buffers in electrical grids, kinetic energy recuperation devices in hybrid cars, power sources for small rechargeable electrical tools and defibrillators, and have many other applications [2].

A crucial strategy for performance improvement of supercapacitors is a development of novel electrode materials with optimized composition and structure. For high performance, electrode materials have to provide

- high electronic conductivity,
- high specific surface area of electrode/electrolyte interface,
- high accessibility of electrode surface for electrolyte species,
- high mechanical and (electro-)chemical stability.

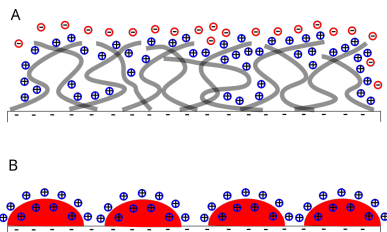


Figure 1: The mechanism of charge storage in supercapacitors (A) by ions adsorption at interface, (B) by ion adsorption and insertion into the electrode material.

Nowadays, carbon-based materials are most commonly used due to their highly adjustable morphology, high abundance and potential of scale-up production. The charge is stored on carbon/electrolyte interface via formation of electrical double layer by physisorption of electrolyte ions and reversible reduction/oxidation of carbon surface functional groups [3] (Fig.1A).

The supercapacitors with carbon electrodes are often referred to as *electrochemical double-layer capacitors* or EDLCs. Carbon is an abundant and non-toxic material. The development of bio-sourced carbon materials is especially beneficial for sustainable development [4]. The limiting factor of carbon-based electrodes performance is a relatively low surface specific charge capacitance (ca. $15 \mu\text{F}/\text{cm}^2$). The highest theoretical specific surface area of single-sheet graphene is ca. $2630 \text{ m}^2/\text{g}$ [5], which translates into highest achievable mass specific capacitance of carbon-based electrode $C_g \approx 500 \text{ F}/\text{g}$, or ca. $35 \text{ W.h}/\text{kg}$ (for symmetrical capacitor with 1 V voltage range). However, even model laboratory carbon electrodes demonstrate specific capacitance in the range $100\text{-}200 \text{ F}/\text{g}$ due to lower surface utilization compared to ideal single-sheet graphene electrode [6]. Scaling up materials to real-type capacitor devices results in further losses of performance due to inhomogenous geometry of electrodes and imperfect contact with electrolyte. Nevertheless, careful adjustment of the morphology of carbon materials may provide the values of energy capacitance above $10 \text{ W.h}/\text{kg}$ [7].

Transition metal oxides (TMOs) are used separately or together with carbon as another type of materials for supercapacitors. The main advantage of TMOs is that a charge can be stored by reversible surface and sub-surface redox reactions and intercalated electrolyte cations into sub-surface layer of TMOs (Fig.1B). These

mechanisms, often referred to as “pseudocapacitance”, provide higher interfacial and mass specific capacitancies [8]. Hence, TMO-based supercapacitors are also called *pseudocapacitors*. In particular, RuO₂ electrodes show specific capacitance above 900 F/g; however, RuO₂ is a toxic and expensive material. Relatively high mass specific capacitance was also reported for oxides of Mn (above 600 F/g) and Ni (up to 1000 F/g in hydrated amorphous form) [9]. The most common obstacles for TMO electrodes utilization in supercapacitors are their low electronic conductivity and degradation of performance due to loss of conductivity during oxidation/reduction cycles.

The most promising strategy toward novel electrode materials is a development of composites of TMOs with high capacitance and carbon materials with high conductivity (TMO/C composites). Performance of the composite materials depends on the properties (e.g. composition, crystalline structure, morphology) of both TMO and carbon, as well as on the efficiency of mixing of the components.

The present work is dedicated to the recent advancements in the development of new types of electrode materials for supercapacitors. Particularly, the electrode materials, developed in ICPEES with active participation of the author, are discussed in details. The goals of the work are:

- to outline the factors determining the performance of different classes of electrode materials for supercapacitors, namely, carbon materials and TMO/C composites,
- to propose the guidelines for further improvement of electrochemical performance of carbon materials and TMO/C composites.

For carbon materials, this work is focused on graphene-based (2D) carbons, and activated (3D) carbon materials. In particular, the bio-sourced activated carbon with high specific surface area (SSA) above 2000 m²/g and specific capacitance of 340 F/g developed in ICPEES [10] is presented. A facile synthesis of the few layers graphene (FLG), worked out in ICPEES [11], is also discussed in details. This synthesis results in a material with lower SSA but comparable specific capacitance of 314 F/g due to optimized porous and graphitic structure.

For TMO/C composites, the work focuses on application of spinel oxides of Fe and Mn. Namely, a composite Fe₃O₄@graphene:PEDOT/PSS, developed in

ICPEES-ICS-IPCMS² is described. This is a composite of Fe₃O₄ magnetite nanoparticles on graphene as storage component and PEDOT/PSS (poly(3,4-ethylenedioxythiophene) / polystyrene sulfonate polymers mixture) layers as structurizing component [12]. The specific capacitance of 153 F/g was obtained even for thick layers of this material (up to 20 μm), demonstrating efficient utilization of storage components due to hierarchical layered structure. The other type of composite materials, discussed in the work, was developed in ICPEES [13], and consists of 10-25 nm nanoparticles of hausmannite Mn₃O₄ oxide uniformly mixed with carbon XC-72. This material demonstrated outstanding capacitance above 250 F/g.

The current work is organized as follows. Chapter 1 gives a general description of electrochemical supercapacitors. In particular, the main principles, characteristics, and parameters, determining supercapacitor performance are presented. The formation of an electrical double layer and the pseudocapacitance phenomenon are discussed. Special attention is given to the impedance spectroscopy as a tool for characterizing interfacial processes. The mathematical models of an impedance of porous electrodes are described.

Chapter 2 deals with the carbon electrodes for supercapacitors. Various types of carbon materials are reviewed and classified by their geometry. Graphene type carbon and porous bio-sourced activated carbon are described in more details, focusing on the materials developed in ICPEES with participation of the author [11, 10].

Chapter 3 is devoted to the TMO and TMO/C composites which are utilized in supercapacitor electrodes. A review of various types of TMO is given with the focus on binary oxides and spinel oxides. The composite materials with oxides of Fe and Mn developed in ICPEES with participation of the author [12, 13] are described.

In Chapter 4 the main directions of further development of the present work are discussed. In particular, the synthesis of activated and porous carbon materials from biological sources and domestic wastes is presented as a prospective approach for sustainable development. The synthesis of TMO/C materials with substituted spinel oxides, M_xFe_{2-x}O₄, where M = Mn²⁺, Cu²⁺, Zn²⁺, Ca²⁺, is proposed as a promising approach toward composite electrode materials for pseudocapacitors. Finally, further development of electrochemical techniques for characterization of

²ICS : Institut de Charles Sadron (Strasbourg); IPCMS : Institut de Physique et Chimie de Matériaux de Strasbourg

electrode materials, based on the model of interfacial impedance, is discussed.

Chapter 1

Electrochemical energy storage

1.1 Electrochemical energy storage devices

Nowadays more than 40% of primary energy sources are consumed by the production of *electricity*. In 2015 world electricity was predominantly (>81%) produced from fossil sources: coal (41%), natural gas (21%), oil (5.4%), and nuclear fuels (13.5%) [14]. The reserves of these sources allow to generate relatively cheap electricity in amount that can be to a large extent adjusted according to immediate needs. Nevertheless, there is a global trend driven by the need of sustainable development to replace these sources by renewable primary energy sources, such as hydroplant, solar, and wind energy. This trend is caused by limited availability and uneven mondial distribution of fossil fuels, as well as strong negative environmental impact of electricity production from them.

Renewable energy sources are obviously more abundant, if not unlimited, comparing to fossil fuels. However, wide scale electricity generation from renewable sources is yet held back by high production price including costs of materials and installations, maintenance and repairs [15]. However, these obstacles will be overcome by continuously improving technologies and "merit-order" effect. The latter is related to a constant increase in the share of renewable energy production [16, 15, 17].

Regardless of electricity production sources, either fossil or renewable, ever-growing world demands of electricity require development of efficient electricity storage technologies and devices. Indeed, electricity production from fossil fuels is predominantly concentrated in large power plants, thus requiring transport of

electricity to final users. The domestic demands of the electricity fluctuate strongly over the course of the day and throughout the week. Thus, an electricity grid between a production plant and final users requires efficient electricity storage devices. Same is true for electricity production at hydroplants. On the other hand, electricity production from solar or wind energy can be more localized, even to the scale of a single household, thus easing up the restrictions of complex electricity grids. However, both solar and wind energy availability is also fluctuating strongly, both geographically and temporarily (over the course of a day, a season, a year), thus, requiring reversible electricity storage facilities.

Electrochemical energy storage devices (EESD), namely, supercapacitors (also known as ultracapacitors) and batteries, provide a possibility of reversible electricity storage by electrochemical phenomena occurring at electrode/electrolyte interface and in the bulk of electrode and electrolyte. Comparing to mechanical energy storage devices (e.g. flywheel), electrochemical storage devices provide higher energy density, better reversibility. In comparison to compressed air storage and pumped hydropower storage devices, EESD have the advantage of zero emission operation [18].

Most important characteristics of performance of an electrochemical storage device are following:

- mass specific or gravimetric, charge capacitance C_g of a device (in A.h/kg, or mA.h/g for batteries, in F/g for supercapacitors),
- maximal operational voltage V (in V),
- mass specific energy density E (in W.h/kg), defined as an amount of electrical energy that can be stored in a device per its mass unit,
- mass specific power P (in W/kg), defined as an amount of energy that can be provided by a device in a unit of time per its mass unit,
- retention or cyclability (in %), defined as a loss of specific energy capacity of a device after a given number of full charge/discharge cycles performed at a given charge/discharge rate,
- price of energy stored (for example, in Euro/kW.h).

Mass specific characteristics presented above are most often used for comparison of the performance of different electrode materials in EESD. Besides electrodes,

EESD also contain components, such as electrolyte, separator, current collector, which contribute to the mass of device without adding energy storage density. Thus, the mass contribution of electrode materials should be predominant, requiring utilization of relatively thick electrode layers. For proper evaluation of the performance of thick layers of electrode materials in real devices, it is also important to study volume specific characteristics (C_V, E_V, P_V), i.e. characteristics calculated per volume unit [19].

Optimal characteristics of electrochemical storage devices varies significantly according to their type of application [20].

- Mobile devices (telephones, computers) require relatively low power output, but high specific energy for long autonomy. On the other hand, for these applications the price acceptance range is relatively high: 2-10 Euro/kW.h, which is 20-100 times higher than the regular price of kW.h in an electrical grid.
- Autonomous means of transportation (cars, buses, trains) require high specific energy capacitance in the range of few tens of kW.h/kg in order to provide few hundreds of kilometers of transportation.
- For stationary (domestic or industrial) applications, a wide range of power output is required in order to ensure uninterrupted functioning of facilities: from few hundreds of W to few tens of MW.

There is no single type of electrochemical storage device that corresponds to this wide variety of demands. In many cases, including automotive transportation, a combination of different types of EESD is very beneficial. For example, combining high energy density batteries with high power output capacitors improves efficiency of energy storage in electrical cars and smart energy grids [21]. Table 1.1 summarizes the range of the typical characteristics for various types of electrochemical energy storage devices. More details can be seen in Fig.1.1 [1].

In this work we focus on novel electrode materials for a particular type of EESD, namely, supercapacitors. In the following section, the principles of supercapacitors, and their similarities and differences comparing to other types of EESD are discussed.

Storage device	Voltage, V	Specific Energy, W.h/kg	Specific Power, W/kg	Typical charge / discharge time	Life span
Capacitors	up to 10^3	10^{-1} – 10^{-2}	$> 10^5$	ms	unlimited
Supercapacitors	1-3	≈ 10	$\approx 10^4$	s - ms	at least 80% retention in 10^5 cycles
Batteries	1-3	$> 10^2$	$\approx 10 - 10^2$	h - s	at least 80% retention in 10^3 cycles

Table 1.1: Typical range of characteristic parameters of electrochemical storage devices.

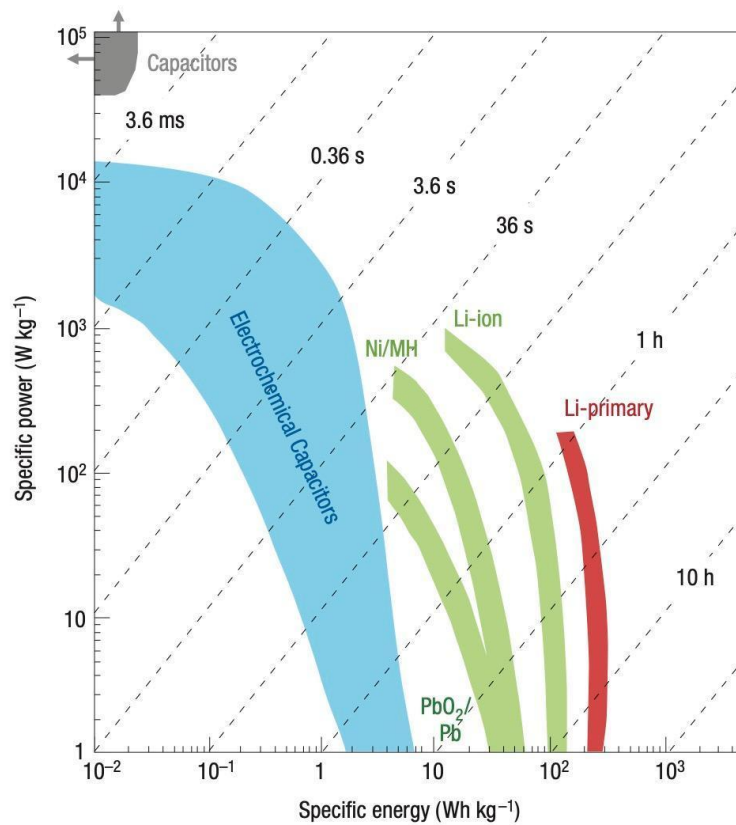


Figure 1.1: Ragone plots for electrochemical energy storage devices [1].

1.2 Supercapacitors

Supercapacitors (also known as ultracapacitors) are the devices with specific energy and power characteristics intermediate between solid state electrostatic capacitors and batteries. Supercapacitors are capable to store significantly more energy comparing to solid state capacitors. On the other hand, in comparison with batteries, they can provide much higher power outputs, being charged and discharged much more rapidly, and sustain up to 100 times more charge/discharge cycles without significant loss of performance. Another advantages of supercapacitors over batteries are the wider operational temperature range (down to -40°C) and safer operation [22]. Outstanding reversibility of supercapacitors, short charging time, and high power output make them optimal storage devices for following applications:

- energy backup systems,
- kinetic energy recovery systems,
- portable high power electric tools,
- defibrillators.

A capacitor is an electric device which under the application of voltage V stores electrical charge Q between two conducting plates separated by an insulator. Capacity C is defined as a charge stored per applied voltage:

$$C = \frac{Q}{V}. \quad (1.1)$$

Capacity C depends on the area of electrodes A , distance d between electrodes, and the dielectric constant ε of the insulator between the electrodes:

$$C = \frac{\varepsilon\varepsilon_0}{d}A, \quad (1.2)$$

where $\varepsilon_0 = 8.854 \cdot 10^{-12}$ F/m is the electric constant (vacuum permittivity).

As mentioned above, from the practical point of view it is also important to define mass-specific capacitance of the device: $C_g = C/m$ (in F/g), where m is a mass of the capacitor. Mass specific energy E and specific power P are given by

(1.3) and (1.4):

$$E = \frac{C_g V^2}{2}, \quad (1.3)$$

$$P = \frac{V^2}{4mR_{ESR}}. \quad (1.4)$$

Here R_{ESR} is an equivalent serial resistance of a capacitor.

Table 1.2 gives some typical values of ε for various solid dry insulators, utilized in solid state capacitors, and water. Due to mechanical properties of solid insulators, smallest practical distance d between the electrodes of solid state capacitors has an order of μm . Thus, solid state capacitors offer surface specific capacitance C_s , defined as a capacity per surface area of electrode $C_s = C/A$, in the range of 10^{-9} F/cm^2 .

In contrast to solid state capacitors, in electrochemical capacitors the electrodes are separated by an electrolyte, for example, an aqueous solution of an inorganic salt. In this case, the applied voltage is limited by the potential range of stability of a solvent; for example, for water this range is 1.23 V. Thus, electrochemical capacitors have much lower working voltage range V , and, lower specific power P , see eq.(1.4), than solid state capacitors. However, electrochemical capacitors have significantly higher specific capacitance, providing higher range of specific energy E despite of lower V . High specific capacitance of electrochemical capacitors is related to the formation of *electrical double layer* at the interface between electrode and electrolyte, which will be explained in the next subsection.

1.2.1 Electrode-electrolyte interface

Physical models of an interface between an electrode (electronic conductor) and a liquid electrolyte (ionic conductor) have been developed during the last century

Insulator	ε
Dry air	1
Paper	$\approx 2-3$
Resins	$\approx 4-5$
Glass	≈ 10
Ceramics	$\approx 20-30$
Water	≈ 80

Table 1.2: Typical dielectric constants ε for some insulators.

[23, 24]. Electrolyte is considered as a homogeneous media containing cations and anions, as well as dipoles of a solvent. Electrolyte species are interacting with electrode via electrostatic force (physisorption) or chemical interaction (chemisorption). This results in a potential-dependent adsorption of electrolyte species at the interface. At a certain potential of electrode, anions and cations are adsorbed in the quantities which provide equal values for negative and positive charges. Therefore, total charge at the interface is equal to 0, and this particular potential is called *potential of zero charge* E_{pzc} . The value of E_{pzc} depends on the electrode properties (in particular, on E_F - the Fermi level of electrons in the electrode material) and the interaction of electrolyte species with the electrode surface. It means that the value of E_{pzc} is specific for a given electrode/electrolyte system.

If the electrode potential is different from E_{pzc} , for example if $E > E_{pzc}$, then the adsorption of anions and the negative-end orientation of solvent dipoles are predominant, resulting in a negative charge accumulated at the electrolyte side of the interface. This negative charge is compensated by the same value of excessive positive charge inside the electrode. The electrolyte species distribution at the interface is depicted in Fig.1.2.

A distribution of electrolyte species on the electrode/electrolyte interface results in the formation of the *electrical double layer* (EDL) which consists, as the name suggests, of 2 layers of adsorbed species.

First, closest to the electrode surface, there is a layer of adsorbed species which have partially lost their mobility due to an interaction with charged electrode surface. This is the so-called *dense layer*, or the *Helmholtz layer*. If the interaction is strong enough, electrolyte ions partially lose their solvation shells and approach electrode surface to a very short distance of few Å, thus forming the *inner Helmholtz plane*, IHP. This phenomena results from the *specific adsorption* of ions, which is more common for anions than for cations, because the latter are in general more strongly solvated. Specific adsorption may also involve partial transfer of a charge to/from an adsorbed ion. This phenomena is important for supercapacitors electrodes, because it is a part of the *pseudocapacitance* phenomena, which will be considered in more details in the Subsection 1.2.3.

If energy of ion interaction with electrode material is not strong enough for partial loss of solvation shell, then the solvated ions are located at the plane which is distanced further from the electrode surface. This plane is called *outer Helmholtz plane* (OHP). The distance between the electrode surface and the OHP ("thick-

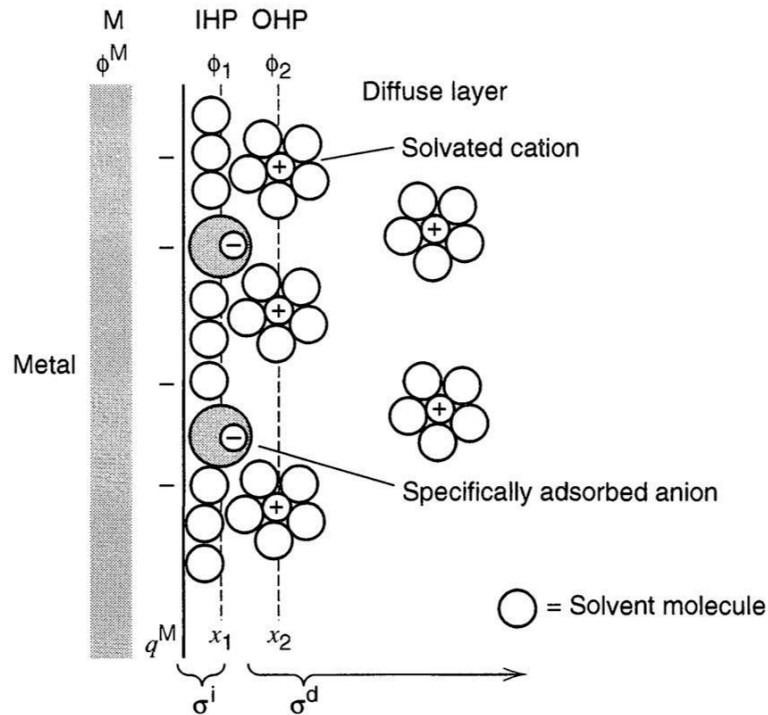


Figure 1.2: A model of metal/electrolyte interface [24].

ness" of the Helmholtz layer) depends on the nature of the electrode and the electrolyte. This thickness is determined mostly by the size of solvated ions and has values in the range of 0.4-0.8 nm [23].

The electric field created by excess charge at the electrode side of interface is, in general, not confined within the OHP and propagates further into the electrolyte. The propagation of the field results in preferential adsorption of ions with an opposite charge to the electrode. These ions are solvated and mobile due to thermal movement, and they form the second part of the EDL: the *diffuse layer* (the *Gouy-Chapman layer*). Contrary to the Helmholtz layer, the thickness of the Gouy-Chapman layer depends strongly on the electrolyte concentration and temperature. The thickness of Gouy-Chapman layer spans from ca. 1 nm for concentrated electrolytes up to few tens of nm for diluted solutions.

Summing up, a modulation of electrode potential results in adsorption/desorption of electrolyte species and accumulation of a certain charge at the electrode/electrolyte interface. Thus, from the electrochemical point of view, the EDL acts as a capacitor, where electrode makes one plate and the ions of the electrolyte form another

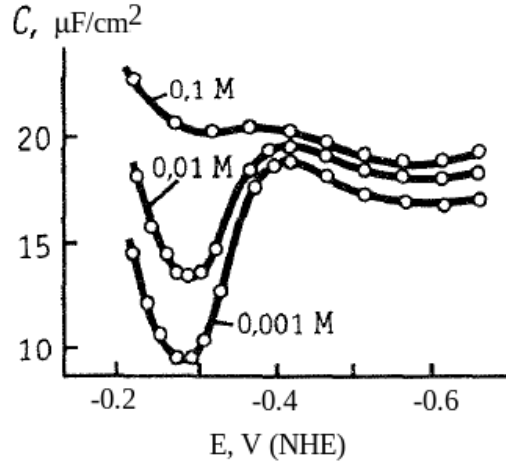


Figure 1.3: Dependence of the EDL capacitance formed on the Bi electrode in aqueous KF solutions with different concentrations [23].

plate. As the EDL is formed by serial connection of the Helmholtz and Gouy-Chapman layers, its capacity C_{dl} is given as follows:

$$\frac{1}{C_{dl}} = \frac{1}{C_H} + \frac{1}{C_{GC}}, \quad (1.5)$$

where C_H and C_{GC} are the capacities of the Helmholtz and Gouy-Chapman layers correspondingly.

As one can see in Fig.1.3, the capacity of the Gouy-Chapman layer C_{GC} depends on the electrode potential: C_{GC} is the lowest at $E = E_{pzc}$ due to the shortest electric field propagation from the electrode to the electrolyte. C_{GC} also depends on the electrolyte concentration: the thickness of the Gouy-Chapman layer is larger in less concentrated solutions, resulting in the lower C_{GC} (see (1.2)). The equation (1.5) indicates that the total capacity of the EDL is determined by its smallest part, which is C_{GC} for diluted solutions and $E \approx E_{pzc}$. Thus, the interfacial capacitance C_{dl} is higher in concentrated electrolytes. The dependence of C_{dl} on the potential is weaker in concentrated electrolytes, but nevertheless observable.

This dependence of electrochemical interfacial capacitance on the electrode potential and electrolyte concentration is reflected in cyclic voltammograms (CV). For solid state capacitors, the diagram of the charging current I depending on the linearly changing applied voltage V (i.e. cyclic voltammogram $I-V$) is square-like. This shape of CV reflects the fact that the capacitance of a solid state capaci-

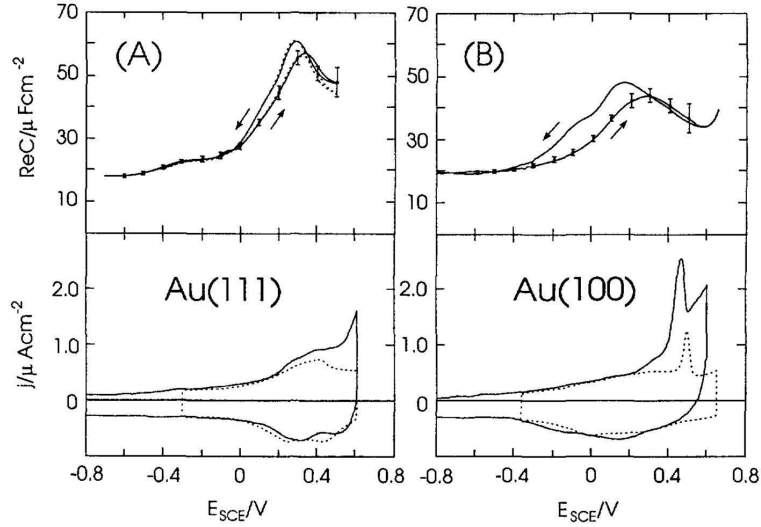


Figure 1.4: Dependence of the interfacial capacitance (top) and corresponding CV curves (bottom) of Au single crystal electrodes: (A) Au(111) and (B) Au(100), measured in 1 mM HClO₄ + 0.1 M KClO₄ (solid lines), in 0.1 M KClO₄ (dashed lines) [25].

tor C does not depend on the applied voltage V . However, as a capacitance of an electrochemical interface depends on an electrode potential E (Fig.1.4(A,B)), the resulting CV have more complex shapes. Thus, the charging current I depends on the potential E , as well as on the composition of electrolyte and even crystallographic orientation of the solid electrode surface (Fig.1.4(C,D) [25]).

For the analysis of interfacial capacitance of electrode materials with complex structure, we can assume that in concentrated electrolyte solutions the thickness of EDL does not strongly depend on the potential, and can be estimated to be ca. 1-2 nm. Considering a high value of water dielectric constant $\epsilon \approx 80$, the surface specific capacitance of an electrochemical electrode/electrolyte interface can be estimated using (1.2) as $C_s \approx 2 \cdot 10^{-5} \text{ F.cm}^{-2} = 20 \mu\text{F.cm}^{-2}$. This value is in a good agreement with typical values experimentally observed for metal/electrolyte interfaces (Fig. 1.3, 1.4). It is important to emphasize that this value is more than 3 orders of magnitude higher than the value of C_s for solid-state capacitors. Thus, electrochemical capacitors offer several orders higher energy density (see Fig.1.1), which explains the name "supercapacitors". Depending on the mechanism of charge storage and involved interfacial processes, two classes of supercapacitors are generally distinguished: electrochemical double layer capacitors (EDLC) and pseudocapacitors.

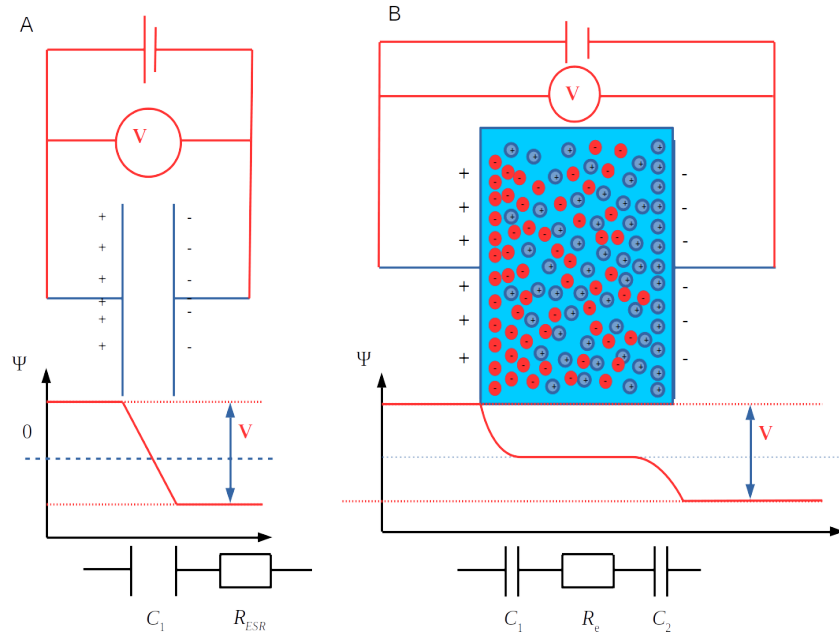


Figure 1.5: The scheme of a distribution of the electrical potential between the electrodes of a solid state capacitor (A) and an EDLC (B).

1.2.2 Electrochemical double-layer capacitors

Fig.1.5 depicts the distribution of the electrical potential between two parallel electrodes of a solid state capacitor and an EDLC. Contrary to a solid state capacitor, an EDLC device is in fact a serial combination of two capacitors, corresponding to the EDL formed at both of electrodes (see equivalent circuits in Fig.1.5(A) and 1.5(B)). The capacity C of the circuit shown in Fig.1.5(B) is given by a serial combination of capacitors:

$$\frac{1}{C} = \frac{1}{C_1} + \frac{1}{C_2}. \quad (1.6)$$

In a symmetric EDLC, the identical electrodes are used at both sides, i.e. $C_1 = C_2$, therefore the total capacity is equal to the half of the capacity of one electrode $C = C_1/2$.

The supercapacitor circuit contains also R_e element, which is the electrical resistance of an electrolyte. The electrolyte is confined in a solid porous separator (polymer, fiber (paper, cotton) or ceramic) to prevent short-circuiting of the capacitor. In general, R_e has a strongest and predominant contribution to the equivalent serial resistance R_{ESR} of the capacitor. The contributions from the

other components, such as the electrodes and contacts, are optimized to have much lower values. The electrolytes with high ionic concentrations are generally used to ensure high ionic conductivity and sufficient amount of ions to form the EDL at the large surface area interface. From the practical point of view, preferable electrolytes should have low viscosity and volatility of solvent, low toxicity, and low cost [22]. There are 3 types of electrolytes generally used in supercapacitors.

- Aqueous electrolytes. Apart from obvious advantages of aqueous electrolytes, such as easy handling and low costs, water has very high dielectric constant ε , which results in high interfacial capacitance and high solubility of inorganic ionic compounds. It allows to use highly concentrated electrolytes with high ionic conductivity in the range of ca. $1 \text{ Ohm}^{-1} \cdot \text{cm}^{-1}$. Viscosity of aqueous electrolytes is often decreased by adding soluble polymers (for example, polyvinyl alcohol (PVA)) in order to prevent leakage and avoid water evaporation. Apparently, the aqueous electrolytes cannot be utilized below freezing point, which limits the operational temperature range of a supercapacitor.

The main disadvantage of aqueous electrolytes is relatively narrow potential range of solvent stability limited thermodynamically to 1.23 V. Thus, the EDLC with aqueous electrolytes usually have operational voltage range V equal or below 1 V. Considering that specific energy (see (1.3)) is proportional to V^2 , the limited voltage operation window is a significant disadvantage of utilization of aqueous electrolytes in supercapacitors.

- Organic electrolytes. Acetonitrile (AN) and propylene carbonate (PC) are two most commonly used organic solvents in supercapacitors. Their physicochemical properties are compared with water in the Table 1.3. Organic solvents allow to extend the working temperature range, and, what is more important, the voltage range, which can be as high as 3.5 V [9]. However, organic solvents have lower dielectric constants, resulting in the lower interfacial capacities. Tetrafluoroborate salts of tetraalkylammonium are commonly used as ionic components of electrolyte with organic solvents due to their relatively high solubility.

Ionic conductivity of these electrolytes is ca. $\approx 0.01\text{-}0.06 \text{ Ohm}^{-1} \cdot \text{cm}^{-1}$, which is lower than that of aqueous electrolytes due to lower mobility and solubility of ionic compounds. In organic electrolytes the ionic transport is slower comparing to aqueous electrolytes. This results, in particular, in much

Solvent	Formula	Dielectric constant ϵ	Melting point $t_m, ^\circ\text{C}$	Boiling point $t_b, ^\circ\text{C}$
Water	H ₂ O	80	0	100
Acetonitrile	H ₃ C–CN	38.8	-46	81.3
Propylene carbonate	H ₃ C–C ₃ H ₃ O ₃	64	-48.8	242

Table 1.3: Physicochemical properties of solvents most commonly used in supercapacitors

stronger decrease in volumetric capacitance of the material with increase of its thickness [26]. Thus, despite having significantly higher specific energy for thin (lab-scale) film electrodes, supercapacitors with organic electrolytes often have lower specific energy and power. Also, organic electrolytes are significantly more difficult to handle due to their strong hydroscopicity: water content below 3-5 ppm is needed to maintain the properties of organic electrolytes.

- Ionic liquids (IL). IL are organic salts with a high low melting temperature. In particular, the room temperature ionic liquids remain in liquid state at ambient conditions and can be used as an electrolyte for supercapacitors. The advantages of IL as electrolytes are: (i) the wide voltage operation range (up to 6V [22]), (ii) the low volatility, (iii) the wide temperature range (down to -95°C), and (iv) the adjustable properties by design of chemical structure of cation and/or anion [27].

The main disadvantages are: (i) low ionic conductivity comparing to aqueous electrolytes (similar to concentrated organic electrolytes), and (ii) high costs of synthesis and handling.

Short thickness of the EDL allows to use the materials with highly developed surface as the electrodes for EDLC, for example, highly porous carbon materials (see Fig.1A). Carbon materials offer mass specific surface area (SSA) as large as $3000 \text{ m}^2/\text{g}$ [7]. On the other hand, carbon/electrolyte interface has lower surface specific capacitance in comparison to metal/electrolyte interface, i.e. below $20 \mu\text{F}\cdot\text{cm}^{-2}$ [28]. For a single-layer sp^2 carbon graphene sheet, the value of $13.5 \mu\text{F}\cdot\text{cm}^{-2}$ is predicted and expected to decrease with the thickness of the carbon stack down to ca. $5 \mu\text{F}\cdot\text{cm}^{-2}$ for graphite structure. Thus, for carbon materials with highly developed SSA, the specific capacitance is expected to be in the range

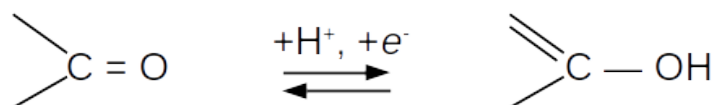


Figure 1.6: Schematic equation of quinone - hydroquinone surface redox transformation.

150-675 F/g. In the Chapter 2 different types of carbon materials utilized in EDLC will be discussed.

1.2.3 Phenomena of pseudocapacitance

The pseudocapacitors are the capacitor devices relying on the pseudocapacitance as a main mechanism of a charge storage. The phenomena of pseudocapacitance is explained below.

In EDLC the charge is stored at the electrode/electrolyte interface due to the electrochemical adsorption of electrolyte ions, i.e. due to the formation of interfacial electrochemical double layer. This is the case when the material of an electrode is electrochemically inert under the applied potential, i.e. no change in oxidation state of any component of electrolyte or electrode occurs during the potential modulation. As the interfacial capacitance in concentrated solutions does not strongly depend on the potential (Fig.1.3), the shape of the CV curves for these electrodes is close to rectangular. This indicates that the current of charging/discharging of double layer is nearly constant, i.e. is practically independent from potential.

However, many of electrode materials undergo surface electrochemical transformations at a certain potential. The following electrochemical phenomena can occur: oxidation/reduction of surface oxides, partial charge transfer to/from adsorbed electrolyte species (for example, electrochemical adsorption/desorption of atomic hydrogen).

For carbon surfaces, the characteristic surface redox transformation is related to the presence of quinone-type groups on partially oxidized surface [29] (Fig.1.6). These groups are responsible for the reversible quinone-hydroquinone electrochemical transition [3], reflected by an appearance of distinct peaks on the CV curves around $E_0 = 0.668 \text{ V (NHE)}$. This potential is claimed to be the equilibrium

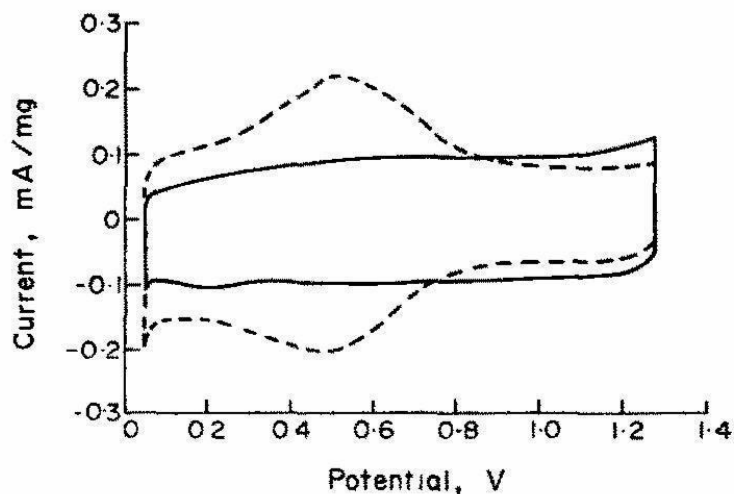


Figure 1.7: CV curves of carbon Vulcan-2700 measured in 1M H_2SO_4 at 14 mV/s, before (solid lines) and after (dashed lines) electrochemical oxidation in 96% H_3PO_4 at 160°C for 45 hours [29].

potential for surface quinone-hydroquinone redox couple (Fig.1.7). The presence of this reversible redox transition results in the potential-dependent charge transfer to/from the electrode. As this redox reaction is reversible, it provides another mechanism of charge storage upon potential modulation similar to the double layer interfacial capacitance. Thus, this phenomenon is referred to as "pseudocapacitance".

Pseudocapacitance increases the total capacitance of electrode/electrolyte interface. For example, redox reaction (1.6) requires $1 e^-$ per 1 quinone-type surface group. For various types of Vulcan carbon, the surface density of the quinone groups has been estimated as 0.09-1.11 %*wt.* [29] or 10^{-10} - 10^{-11} mol \cdot cm $^{-2}$ (by the author's estimations), depending on the oxidation state of carbon surface. Thus, according to the Faraday law, Vulcan carbon pseudocapacitance, related to presence of quinone surface groups, provides additional 1-10 $\mu\text{F}\cdot\text{cm}^{-2}$ as calculated for 1 V potential range. This contribution is comparable with the EDL capacitance value of carbon surface.

A low surface specific capacitance of sp^2 carbon surface can be increased in the presence of heteroatoms of non-metal elements at the interface, such as N, S, B. The effect of N-doping on the properties of carbon materials, in particular, the improvement of charge storage capacitance, is studied most thoroughly [30].

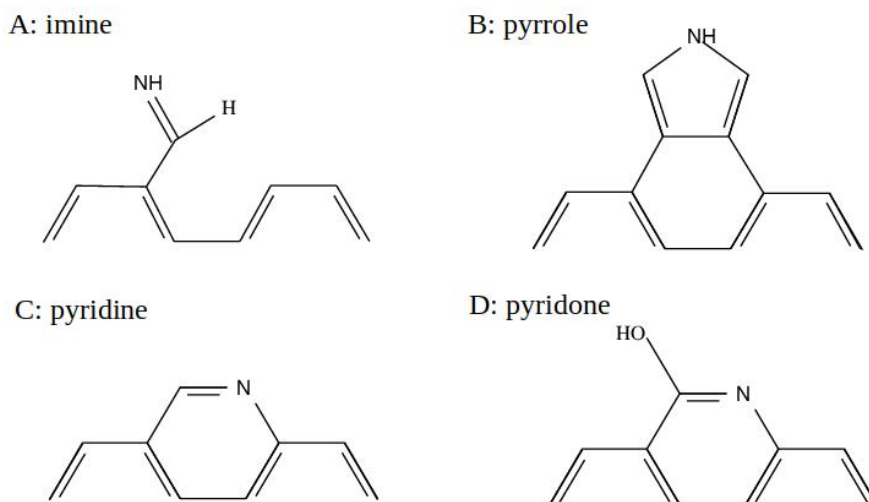


Figure 1.8: Some functional N-containing groups that can be formed at the carbon/electrolyte interface (Fig. adapted from [31]).

Nitrogen can be incorporated into the carbon structure in various coordination states. These states are characterized by their specific electronic configurations as reflected by N1s XPS BE (binding energy) values: pyridine (398.4 ± 0.2 eV), imine (398.8 ± 0.2 eV), pyrroles (400.6 ± 0.2 eV), pyridones (400.6 ± 0.2 eV) and oxidized nitrogen (nitrito/nitroso groups) (400.7 ± 0.2 eV) [31], see Fig.1.8. An increase in charge storage capacitance due to the presence of N atoms can be caused by the following effects.

- **Better wettability of carbon surface.** Nitrogen increases the polarization of surface bonds [30], and, in general, increases hydrophilicity of the carbon surface. This effect is, however, claimed to be minor [32]: a higher capacitance of a B-doped carbon electrode comparing of an N-doped electrode is reported, despite better wettability of the latter.
- **Better conductivity.** Nitrogen is more electronegative than carbon and provides additional electron into π -conjugated electron state, resulting in increased conductivity. However, nitrogen disturbs otherwise uniform carbon structure, resulting in possible decrease in conductivity. Thus, N-doping of carbon can have both positive and negative influence on conductivity, and, in general, an optimal composition and type of functionalization must be found.

For example, N-doping of carbon nanofibers up to 3.1%_{wt.} N resulted in an increase of their conductivity by more than 50%. However, further increase in N-content up to 8.2%_{wt.} resulted in ca. 33% lower conductivity in comparison to the pristine material [33]. It is important to note that in general carbon materials in supercapacitors already have high conductivity, and an increase in conductivity due to N-doping does not significantly influence their performance [32].

- **Pseudocapacitance.** The N-doped carbon electrodes are known to have strongly enhanced activity in the electrocatalytic oxygen reduction reaction (ORR) [34, 35, 36] comparing to the bare carbon electrodes. The exact nature of active sites on the surface of N-doped carbon electrocatalysts is still debated. However, the enhancement of the activity by N-doping has been attributed to (i) increased polarisation of chemical bonds at electrode/electrolyte interface and (ii) adjustment of the conjugated carbon π -electrons density [35]. Altogether, these effects result in stronger interaction of electrolyte components with carbon surface, facilitating their adsorption and further redox transition. It has been argued [32] that these effects are also responsible for the enhanced intercalation of electrolyte components (H^+OH^-) in the sub-surface interfacial region and further into the bulk of carbon materials. The enhanced intercalation results in increase of the charge related to pseudocapacitance phenomena. In fact, it has been claimed that the enhanced interaction between electrolyte species and carbon surface is the main reason for increasing charge capacitance for the N-doped carbon electrodes.

Contrary to the EDL capacitance, the pseudocapacitance is not confined to the electrode/electrolyte interface but can propagate further into the bulk of the electrode. An impressive example is a hydrogen cation intercalation into carbon in acidic electrolytes, which was studied in details on activated carbon CH900-200 ACC (Japan), SSA = 1520 m²/g [37, 38]. It was concluded that the maximal capacitance of intercalation, obtained by prolonged (several hours) galvanostatic cathodic polarization, corresponds to the reversible formation of a stoichiometric compound "hydrogen carbide" C₆H, i.e. to the storage of 1 e⁻ per 6 carbon atoms:



This intercalation provides the maximal contribution of pseudo-capacitance for the studied CH900-200 carbon equal to 942.8 F/g. This results in outstanding total specific capacitance 1114.3 F/g, which is, to the best of author's knowledge, is the highest specific capacitance reported for carbon electrodes. However, the hydrogen intercalation into carbon requires the acid-induced swelling of carbon graphite structure, which is a slow process. In [38] a model of charge storage pseudocapacitance in activated carbon limited by slow solid-state diffusion of intercalated hydrogen was proposed. The estimated diffusion coefficient of hydrogen in carbon has a value $D \approx 5 \cdot 10^{-17} \text{ cm}^2/\text{s}$. This value is few orders of magnitude lower than the one reported for solid-state diffusion coefficients of Li^+ cations in the graphite anode of Li batteries [39, 40]. Such slow diffusion makes the above mentioned high capacitance of the CH900-200 ACC impractical.

Another important difference between the EDL capacitance and pseudocapacitance is the strong dependence of the latter on the electrode potential. The pseudocapacitance is the strongest at the potential corresponding to the reversible potential of redox transformation E_0 . This fact is reflected by the pronounced pair of redox peaks on the CV curve around E_0 . This pair of peaks is centered around E_0 , and the peaks separation depends on the rate of the process [41]. The CV peaks separation is equal to ca. 60 mV for the fast redox transformation which is not limited by the solid-state diffusion, e.g. the surface redox transitions (Fig.1.7). However, if the process is strongly controlled either by the slow kinetics of the interfacial charge transfer or by the solid-state diffusion, then the peaks separation can be as strong as few hundreds of mV (Fig. 1.9). The strong dependence of C_g on the electrode potential makes misleading its utilization as a characteristic for the performance of a supercapacitor electrode material [42]. At the potential range around E_0 , C_g has much higher values than expected for the EDL capacitance. However, these high C_g values are observed only in a limited range of the electrode potential. According to (1.3), a limited potential range provides a low energy density despite the high C_g values. Thus, in general, the energy density is a better characterization parameter for the efficiency of pseudocapacitance materials.

The pseudocapacitance is a main phenomenon involved in the charge storage in metal oxide materials, which form the second biggest class of materials for supercapacitors electrodes [1, 22, 9, 43]. Similarly to the oxidized carbon surface, the atoms of metal at or in the vicinity of the electrode surface can undergo a reversible

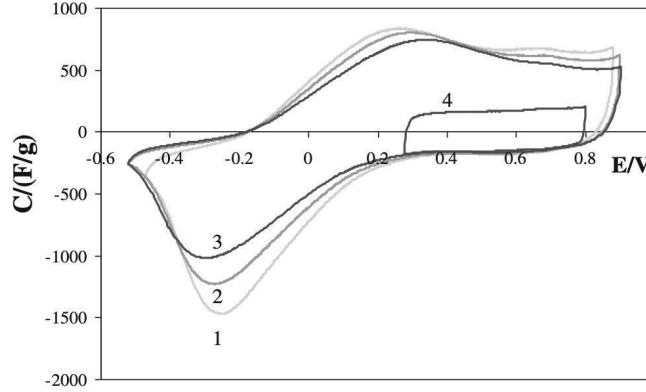


Figure 1.9: The capacitance-potential curves of the activated carbon CH900-200 in 48% H_2SO_4 measured at the potential sweep rates 0.5 mV/s (1), 1 mV/s (2), 2 mV/s (3,4). The pairs of peaks in the range of -0.4 .. 0.4 V correspond to the hydrogen intercalation, according to (1.7) [37].

redox transformation due to the variability of oxidation states for transition metals. In comparison to the carbon, the percentage of metal sites available for the redox transformation is much higher: every metal atom is capable to change its oxidation degree and participate in the charge storage. This phenomenon provides significantly higher pseudocapacitance values for metal oxides comparing to carbon materials. The values above 900 F/g are routinely observed for the RuO_2 -based electrode materials, which are the ones of the best performing oxide materials for supercapacitors. As for the carbon electrodes, different mechanisms of pseudocapacitance of the metal oxides can be proposed: the surface redox-transitions and the intercalation. However, these mechanisms are related for the metal oxides. For example, for RuO_2 , which is the most studied metal oxide supercapacitor material, the redox transition is described by the reaction (1.8) [44]:



The transformation degree and the stored charge are characterized by the intercalation parameter δ , $0 < \delta < 1$. The reaction starts as the electroreduction of the RuO_2 surface and then propagates into the bulk of oxide. According to (1.8), this process can be also considered as the H-intercalation. There is also an ongoing discussion on the possibility of the intercalation of another electrolyte cations beside H^+ , for example, K^+ . The exact nature of the pseudocapacitance phenomena for various types of oxide materials is discussed in details in the Section 3.

Before starting the discussion on the particular types of electrode materials for supercapacitors, the important difference between batteries and pseudocapacitors is outlined in the next Subsection.

1.2.4 Pseudocapacitors and ion-insertion batteries

The cation intercalation is an important mechanism of pseudocapacitance in the materials for supercapacitor. The cation intercalation is also a charge storage mechanism in the batteries: in particular, the Li^+ cations are intercalated into the graphite cathodes in the conventional Li batteries [45]:



Apparent similarities between redox intercalation reactions (1.7) and (1.9) require the definition of the criterion to distinguish between the electrodes behavior of batteries and supercapacitors [8, 42]. It is important to emphasize that the main differences in the performance of batteries and supercapacitors are the higher power output and the cyclability of the latter. Thus, the intercalation reaction in supercapacitors should be relatively fast and not induce the significant structural changes of the electrode material.

In general, the intercalation reaction can be expressed as:



Here Ct^+ is an electrolyte cation, δ is an intercalation parameter, M is an intercalated host material, and $\text{M}-\text{Ct}_\delta$ is an interfacial layer of M with the intercalated cation. The rate of this reaction can be expressed by the equation [40], which is similar to the general Butler-Volmer equation combined with the Frumkin isotherm:

$$i = i_0 \left((1 - \delta) e^{-(1-\alpha)g\delta} e^{(1-\alpha)f(E-E_0)} - \delta e^{\alpha g\delta} e^{-\alpha f(E-E_0)} \right). \quad (1.11)$$

Here i is a current density of the intercalation reaction, i_0 is an exchange current density of the intercalation reaction, α is a symmetry factor ($\alpha = 0.5$ for reversible intercalation [40]), g is the constant of the Frumkin isotherm, characterizing the lateral interaction between the intercalated ions ($g < 0$ for attractive interaction and $g > 0$ for repulsive interaction), $f = F/RT$, E is an electrode potential, and

E_0 is a equilibrium potential of the reaction (1.10).

If the potential is changed relatively slow (slow sweep rate or slow charging current), then δ corresponds to the potential-dependent equilibrium between intercalation and de-intercalation according to the Frumkin isotherm:

$$\frac{\delta}{1-\delta} = e^{f(E-E_0)} e^{-g(\delta-0.5)}. \quad (1.12)$$

Let us note that the equations (1.11) and (1.12) are given for the electrode/electrolyte interface. These equations are valid only if the solid state diffusion is sufficiently fast, so that the gradient of δ within the bulk of host material is negligible and is not influencing interfacial processes. In [40] it is shown that for the Li intercalation into Li_xCoO_2 the model is valid at the sweep rate range of 10-50 $\mu\text{V/s}$. At a faster potential change the solid phase diffusion influences and controls the rate of interfacial process. Therefore, the equations (1.11) and (1.12) are no longer valid.

In order to evaluate the reversibility of an intercalation reaction, Simon et al. [8] proposed to analyze the dependence of the CV peaks current density j on the potential sweep rate v : $j = av^b$. The power b is an experimental quantitative criteria of the reversibility. The value of b is changing, depending on the rate-determining step of intercalation process. Namely, $b = 1$ for the reversible interfacial reaction and $b = 0.5$ for the reaction limited by the semi-infinite diffusion of the reagents. For example, the data of [37] for the capacitance of CH900-200 shows the constancy of the charging current normalized by the potential sweep rate v , i.e. $b = 1$. Thus, according to the criteria [8], the studied carbon electrode acts as a supercapacitor electrode.

However, it should be noticed that even the battery electrode materials can demonstrate reversible electrochemical behavior in agreement with the equations (1.11) and (1.12) at sufficiently low rate of the potential change. As it has been mentioned above, this was observed experimentally for the Li^+ intercalation to Li_xCoO_2 [40] at the sweep rates below 50 $\mu\text{V/s}$ and to the graphite at the sweep rates below 4 $\mu\text{V/s}$.

Thus, the reversibility of the intercalation reaction cannot be the only criterion that allows to classify a material as a supercapacitor electrode material. As mentioned above, the high power output and capacitance retention are the main performance criteria to distinguish supercapacitors from batteries. Thus, the tests of reversibility of charging/discharging have to be performed at the conditions,

which are expected for the supercapacitor operations: i.e. the charging time of the order of a minute (60C in terms of the Li batteries characterisation). For example, for a capacitor with the operational potential range of 1V, such charging time suggests the rate of potential cycling of ca 16.7 mV/s; or, for the case of galvanostatic cycling and the specific capacitance of 120 F/g it suggests the charging current of 2 A/g. If the characterization of electrode performance is done under these conditions and reversible behavior is observed, then it can be concluded that the electrode material behaves as a capacitor, even though if the mechanism of the charge storage involves the intercalation reaction.

The performance of the materials as the supercapacitor electrodes can be studied in various configurations (cells with 2 or 3 electrodes, membrane separator or liquid electrolytes) and by various electrochemical techniques. The most commonly used techniques are the cyclic voltammetry (CV) and the galvanostatic charging with potential limits (GCPL). Another important electrochemical technique allowing detailed study of processes on the electrode/electrolyte interface is the electrochemical impedance spectroscopy (EIS). A comparison of the capacitance analysis using these 3 groups of methods (CV, GCPL, EIS) was given in [46]. It was concluded that the methods provides consistent data, however a special care (specific to each of the methods) should be taken to ensure the validity of the results. The EIS, in particular, requires a relatively small potential modulation (few mV) and, in general, a multi-parameter model to extract the relevant data. Under these conditions, the EIS provides the most detailed insight into the interfacial processes. Thus, in the next section, the EIS is discussed in details. Particularly, a model of the impedance of porous electrodes is presented. The model is applied to predict the optimal structures of electrode materials for the best performance in supercapacitors.

1.3 Impedance of electrochemical electrode/electrolyte interface

The electrochemical impedance spectroscopy is a powerful tool for studying the processes on the electrode/electrolyte interface [47]. The interfacial impedance is measured as a function relating the modulating electrode potential $\vec{E} = E_0 \cdot \sin(\omega t)$ and the current passing through the electrode/electrolyte interface $\vec{I} = I_0 \cdot \sin(\omega t +$

ϕ_0):

$$\vec{Z}(\omega) = \frac{\vec{E}(\omega)}{\vec{I}(\omega)}. \quad (1.13)$$

Here $\omega = 2 \cdot \pi f$ is an angular frequency, f is a modulation frequency, and ϕ is a phase shift angle between \vec{E} and \vec{I} . As discussed above, a modulation of the electrode potential may result in a number of interfacial processes, which are generally classified as non-faradaic and faradaic. In a non-faradaic process neither electrolyte species, nor electrode components change their oxidation states, i.e. there is no redox (faradaic) process. Generally, 3 types of interfacial processes may occur.

- **Adsorption/desorption.** The adsorption of ions on the electrode surface results in the formation of the EDL [23] and accumulation of the charge on the interface, similar to the charge accumulation in a capacitor. Thus, the interfacial impedance of the process is given as

$$\vec{Z}_C = \frac{1}{i\omega C_{dl}}, \quad (1.14)$$

where C_{dl} is a EDL capacitance. C_{dl} can be calculated as $C_{dl} = C_s \cdot A$, where A is a surface area of the electrode/electrolyte interface. C_s is a surface specific interfacial capacitance, which depends on the nature of the interface and is generally found in the range of 5-30 $\mu\text{F}/\text{cm}^2$. According to (1.14), the phase angle of \vec{Z}_C is $\phi = 90^\circ$ (Fig.1.10(1)).

- **Interfacial charge transfer.** If at least one component of an electrolyte or an electrode changes its oxidation state due to the potential modulation, then the redox faradaic process occurs at the electrode/electrolyte interface:



If the electrode potential is close to the equilibrium potential $E_{\text{Ox/Red}}^0$ and the potential modulation is small, then \vec{I} changes linearly with \vec{E} , similarly to Ohm's law. Thus, the impedance of the interfacial charge transfer can be evaluated as the charge transfer resistance R_{ct} with $\phi = 0^\circ$:

$$R_{ct} = \frac{RT}{nF i_0}. \quad (1.16)$$

Here i_0 is an exchange current rate of the process, which is related to the kinetic parameters of the reaction:

$$i_0 = F A k_0 C_{\text{Ox}}^{1-\alpha} C_{\text{Red}}^\alpha, \quad (1.17)$$

where C_{Ox} and C_{Red} are the concentrations of Ox and Red in the electrolyte, α is a symmetry factor of a given electrochemical reaction (1.15), $0 < \alpha < 1$, k_0 is a heterogeneous rate constant of the reaction (1.15).

- **Diffusion to/from the interface.** According to the equations (1.16),(1.17), the value of R_{ct} depends on the concentration of Ox and Red. If the reaction (1.15) is fast, then the concentrations of reagents at the interface are not the same as in the electrolyte. Thus, for the fast reactions, the rate of reaction (1.15) is influenced by the rate of diffusion of reagents to/from the interface. In the impedance measurements, this influence is reflected by an additional component of the impedance in a serial combination with R_{ct} , namely, the Warburg impedance \vec{Z}_W :

$$\vec{Z}_W = \frac{\sigma}{\sqrt{\omega}} + \frac{\sigma}{i\sqrt{\omega}}. \quad (1.18)$$

The parameter σ is the Warburg constant. It is related to the parameters of the reagents diffusion in an electrolyte:

$$\sigma = \frac{RT}{n^2 F^2 A \sqrt{2}} \left(\frac{1}{C_{\text{Ox}} \sqrt{D_{\text{Ox}}}} + \frac{1}{C_{\text{Red}} \sqrt{D_{\text{Red}}}} \right). \quad (1.19)$$

Here D_{Ox} and D_{Red} are the diffusion coefficients of Ox and Red in the electrolyte. From (1.18) it can be seen that the Warburg impedance \vec{Z}_W has the phase angle $\phi = 45^\circ$ ($\text{Re}(\vec{Z}_w) = \text{Im}(\vec{Z}_w)$).

1.3.1 Impedance of the flat electrode/electrolyte interface.

In the absence of redox processes on the flat electrode/electrolyte interface, its impedance can be represented by a serial combination of R_1 and C_{dl} , where R_1 depends on the conductivity of an electrolyte and the geometry of the electrochemical system. R_1 can be measured as a limit of $\vec{Z}(\omega)$ at high f .

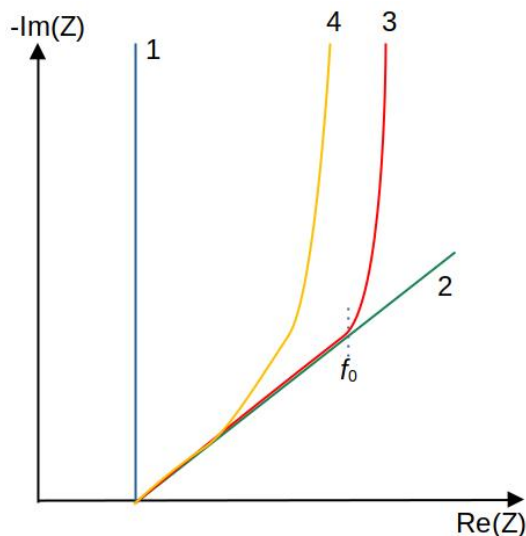


Figure 1.10: The schematic representation of the Nyquist diagram for the non-faradaic impedance \vec{Z}_{nf} : (1) flat electrode (1.14), (2) semi-infinite cylindrical pore, (3) finite cylindrical pore, (4) an electrode with pores of different diameters.

When a redox process occurs on the interface, the interfacial impedance includes a faradaic impedance component \vec{Z}_f . At a small potential modulation, C_{dl} and \vec{Z}_f can be considered as independent components. Therefore, the interfacial impedance can be modeled as their parallel combination (Fig.1.11(A)).

In a simplest case of a faradaic process, namely, the reversible electrochemical reaction, controlled by its kinetics and the diffusion of electrolyte components, \vec{Z}_f is modeled by the Randles circuit (Fig.1.11(B)). This circuit consists of a serial combination of 2 components: R_{ct} and \vec{Z}_w .

The Randles model predicts that $\lim_{\omega \rightarrow \infty}(\vec{Z}) = R_1$ and $\lim_{\omega \rightarrow 0}(\vec{Z}) = R_1 + R_{ct} + Z_w$, as it is observed, for example, for the reversible redox transformation of the $\text{Fe}^{\text{II}}/\text{Fe}^{\text{III}}$ -cyanide complex on the Au polycrystalline electrode [48]. Fitting experimental impedance spectra by the Randles model allows to determine k_0 , D_{Ox} and D_{Red} for a reversible faradaic process on the flat electrode.

For more complex reactions, the model of Faradaic impedance has to be modified. For example, if the reaction involves the formation of adsorbed intermediate, it results in an accumulation of a charge on the interface and adds a capacitive component into \vec{Z}_f . The impedance of this process is described by the Melik-Gaykazyan model impedance [49](Fig.1.11(C)).

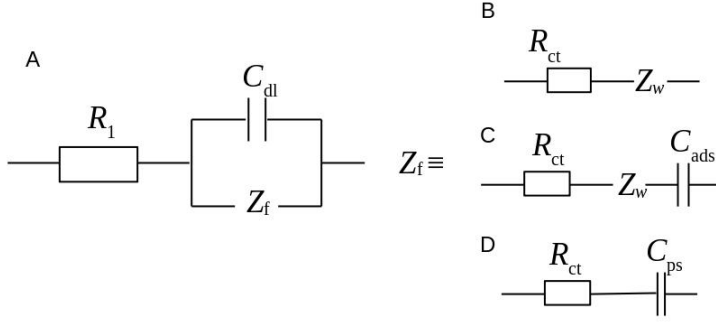


Figure 1.11: (A) The model equivalent circuit of the impedance of the flat electrode/electrolyte interface in the presence of a faradaic process. The models of the faradaic impedance \vec{Z}_f : (B) the Randles model, (C) the Melik-Gaykazyan model, (D) pseudocapacitance model.

1.3.2 Models of impedance of rough electrode/electrolyte interface

The models from Subsection 1.3.1 describe the impedance of flat uniform electrode/electrolyte interface, for which the current lines are parallel and evenly distributed, and also are perpendicular to the interface. However, the materials with rough surfaces and porous materials are commonly used in the EESD in order to increase surface and volume specific energy densities.

For the rough electrode surface, the current lines, directing toward the surface, are not parallel. This results in uneven conditions of the interface polarization. In this case the frequency dependence of impedance parameters, such as C_{dl} (1.14), R_{ct} (1.16) and σ (1.19), is observed [50]. For the non-faradaic impedance, this frequency dependence can be taken into account by using the model of constant phase element (CPE):

$$\vec{Z}_{CPE} = \frac{1}{(i\omega C_{dl})^a}. \quad (1.20)$$

Here a is the CPE constant; if $a=1$, then $\vec{Z}_{CPE} = \vec{Z}_{nf} - R_1$, and the CPE acts as an ideal capacitor with the frequency-independent C_{dl} . For the rough electrodes, the frequency dependence of the measured C_{dl} is described by \vec{Z}_{CPE} with $a < 1$. For example, $a \approx 0.9$ for the polycrystalline Au / HClO_4 interface, while $a \approx 0.99$ for the Au single crystal electrode [51].

The detailed finite element analysis demonstrated that the effect of the capacitance frequency dispersion on the non-faradaic impedance is observed at high frequencies $f > 10$ kHz for not very rough electrodes [52, 53]. However, for the adsorption with the interfacial partial charge transfer (i.e. the specific adsorption),

the frequency dispersion of R_{ct} and C_{ads} is predicted even for low frequencies [54].

In general, the application of the CPE model allows to fit the experimental impedance spectra and determine, for example, the C_{dl} capacitance even for rough or non-uniform electrodes. However, due to the multiple possible origins of $a < 1$, one has to be certain to understand the properties of a particular electrode/electrolyte interface and evaluate the applicability of the CPE model in each particular case. On the other hand, if the utilization of the CPE model is valid, the value of a provides the additional information about the structure of the electrode/electrolyte interface. For example, if $a < 1$ value is related only to the surface roughness, then the roughness can be characterized by a fractal dimension of the surface D_f , which is related to a [50]:

$$a = \frac{1}{D_f - 1}. \quad (1.21)$$

The porous electrode materials have a wide range of applications in various types of electrochemical devices, including supercapacitors [1].

The formation of the EDL and the pseudocapacitance are two main mechanisms of charge storage in the supercapacitors. The impedance of the EDL formation can be modeled as a non-faradaic impedance. In the presence of the pseudocapacitance, the interfacial impedance includes the faradaic impedance, which can be modeled as a serial combination of R_{ct} (related to the kinetics of interfacial reaction (1.16)) and C_{ps} (related to capacitance of ions intercalation) (Fig. 1.11(D)).

In order to model the impedance of electrodes of supercapacitors, the influence of porous structure has to be taken into account for any mechanism of the interfacial charge storage. The impedance of the interface inside a pore is often modeled by the staircase-type equivalent circuit (Fig.1.12).

It was demonstrated that for the infinitely long cylindrical pore the interfacial impedance is described by the following equation [47]:

$$\vec{Z}_p = \sqrt{R|\vec{Z}|} e^{i\frac{\phi}{2}}. \quad (1.22)$$

Here R is an electrolyte resistance within the pore per unit length, \vec{Z} is an impedance of a pore wall / electrolyte interface, and ϕ is a phase angle of \vec{Z} . (1.22) predicts that the interfacial impedance inside the pore has a phase angle equal to a half of an impedance of a flat electrode. For example, for the non-faradaic

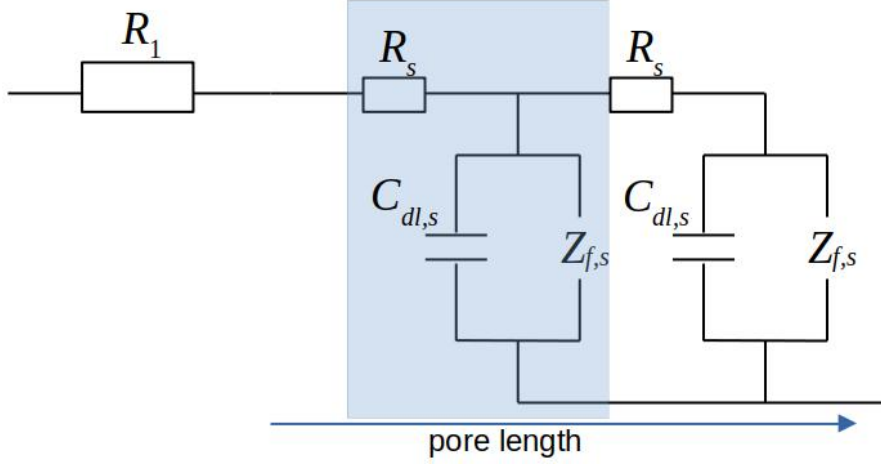


Figure 1.12: The staircase equivalent circuit of the impedance model inside a single pore. The highlighted elements form the repeating pattern along the pore.

impedance \vec{Z}_{nf} the DeLevi model predicts a constant phase angle $\phi = 45^\circ$.

For the analysis of a pore with a finite length l_p using the staircase model, it is convenient to define a length λ of the penetration of the potential modulation into the pore [55]:

$$\lambda = \frac{1}{2} \sqrt{\frac{\sigma d_p}{2\omega C_s}}. \quad (1.23)$$

Here σ is a conductivity of an electrolyte (in $\text{Ohm}^{-1} \cdot \text{m}^{-1}$), d_p is a pore diameter, and C_s is a surface specific interfacial capacitance.

From (1.23) it can be concluded that λ increases with a decrease in the modulation frequency $f = \omega/2\pi$. Thus, $\lambda > l_p$ for the frequencies below a certain threshold f_0 . Under this condition, the potential modulation is uniform along the whole length of the pore, and the pore impedance is the same as the impedance of a flat electrode with the same surface area. In this case, one observes a change from the shift angle $\phi = 45^\circ$ at $f > f_0$ to $\phi = 90^\circ$ for $f < f_0$ in the Nyquist diagram (Fig.1.10(3)). This transition is often observed for the porous carbon electrodes (for example, in [10]). In general, the transition is much less sharp and occurs over a certain range of frequencies (Fig.1.10(4)) due to the presence of the pores with various diameters and shapes [55, 56].

This staircase model allows to correctly fit the experimental impedance spectra of the porous electrodes in the absence of faradaic processes and determine the

capacitance C_{dl} . Moreover, the average pore length l_p can be estimated from the f_0 value, providing that the average diameter d_p of the pores is known from the other methods.

In the above mentioned models it is assumed that individual pores are not interconnected. Therefore, the staircase circuit is applied independently to each pore. The supercapacitors electrode materials, for example the activated carbon, often have hierarchial pores: the larger pores branch into several smaller pores of next generation, which can branch further. The hierarchial porous structure makes the application of the staircase model more complicated, because the staircase circuits of pores from different generations are no longer independent.

The model of branching pores was proposed in [57] by introducing 2 generations of pores: the large (μm size) voids between carbon particles and the narrower (sub- μm size) internal pores. The larger pores were branching into n smaller pores, and the length and diameter of smaller pores were scaled by a_l and a_d factors in comparison to the parent pores. Fitting the experimental spectra allowed to estimate the branching factor n and scaling factors a_l, a_d . However, these values had to be considered as estimates only, because the porous structure is more complex.

The model also demonstrates that the pores branching is counter-productive for efficient utilization of the capacitance of porous electrodes. Indeed, the capacitance of the interface of the porous electrode was equal to the capacitance of a flat electrode C_{dl} with the same surface area only if the lowest possible branching factor n was assumed. This conclusion is an important guiding rule for material science in the optimization of the structure of electrode materials. However, the unambiguous analysis of the influence of various structural parameters is difficult because of their interdependence. In particular, in [57] the porosity of electrode material and the length scaling factor a_l were fixed. An increase in the branching factor led to narrowing of branch pores which decreased the modulation penetration depth (1.23), and, thus, the efficiency of pore surface utilization.

It has also to be mentioned that the model in [57] assumed the serial connection of a parent pore and its branches: such as if the pores were branching only at their bottom points. This allowed to utilize the same polarization conditions for all pores of the same generation, thus simplifying the model. In reality, however, the branches may appear over the whole length of a pore (Fig.1.13).

In the following subsection the improved model of the impedance of a porous

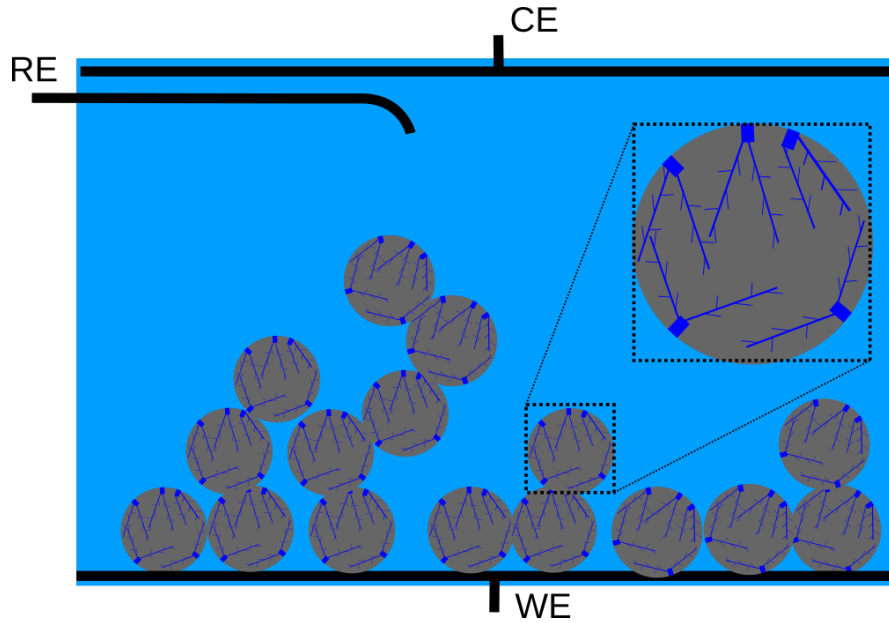


Figure 1.13: The sketch of an electrode with hierarchial porous structure with 3 generations of pores.

electrode is presented. This model utilizes staircase circuit and takes into account the presence of 3 generations of branching pores. The pores of 2^{nd} and 3^{rd} generations are formed by branching a parent pore. The branches are uniformly distributed over the length of the parent pore. The faradaic impedance of pseudocapacitance is also included into the staircase model, allowing to model the porous electrodes of pseudocapacitors. Thus, this model is further referred to as "generalized staircase model". The goal is to predict the influence of the structural parameters of electrode materials on their performance in supercapacitors. Namely, the influence of the pores length and diameter, the porosity of the material, and the branching factors is evaluated.

1.3.3 Generalized staircase model of impedance of porous electrode materials.

The sketch of the electrode material is depicted in Fig.1.13. The material is assumed to have 3 hierarchial generations of pores. The pores of the 2^{nd} and 3^{rd} generations are the branches of the pores of the parent generations and evenly distributed over the length of a parent pore. The pores of 3^{rd} generation are terminal: they have no branches.

Each generation of the pores has 2 characteristic parameters: a pore length $l_{p,i}$ and a pore diameter $d_{p,i}$, where i is a generation index. The surface area of the individual pore of the i^{th} generation is given as

$$A_i = \pi d_{p,i} l_{p,i} + \frac{\pi d_{p,i}^2}{4}. \quad (1.24)$$

Neglecting the surface of the material outside the pores, the total surface area of the material is calculated as the surface area A_p of all pores:

$$A_p = N_1(A_1 + \beta_{12}A_2 + \beta_{12}\beta_{23}A_3). \quad (1.25)$$

In equation (1.25), β_{12} and β_{23} are the branching factors: $\beta_{12} = N_2/N_1$, $\beta_{23} = N_3/N_2$, where N_1 , N_2 , N_3 are the numbers of pores of the 1st, 2nd, and 3rd generations correspondingly. The factors β_{12} and β_{23} are the model parameters, whereas N_1 is found as

$$N_1 = \frac{m \cdot SSA}{A_1 + \beta_{12}A_2 + \beta_{12}\beta_{23}A_3}, \quad (1.26)$$

where m is a mass of the deposit (in g), SSA is a specific surface area of a the electrode material (in cm²/g).

The impedance of the pores of each generation is modeled by the staircase circuit as described below.

Model of an individual pore of the 3rd (terminal) generation.

An equivalent circuit utilized in the improved generalized staircase model of the impedance \vec{Z}_{3g} of an individual pore of the 3rd generation (a pore with the smallest diameter and without branches) is depicted in Fig.1.14. The pore is divided into $K = 2^n$ identical segments. The value $n = 10$ is used for all calculations, as it was found that further increase in n does not change the results of modeling.

For the pore with the diameter d_p and the length l_p , the length of a segment is $\delta_l = l_p/K$, the surface area of the walls of the segment is $A_s = \pi d_p \delta_l = \pi d_p l_p / K$, and the surface of the bottom of the pore is $A_b = \pi d_p^2 / 4$.

A single segment has an interfacial impedance \vec{Z}_s . It consists of a component $C_{dl,s}$, which is the EDL capacitance of the walls of the segment. If the model includes also a faradaic impedance, then a faradaic impedance $\vec{Z}_{f,s}$ of the segment walls is added in parallel to $C_{dl,s}$. Therefore, in the presence of pseudocapacitance

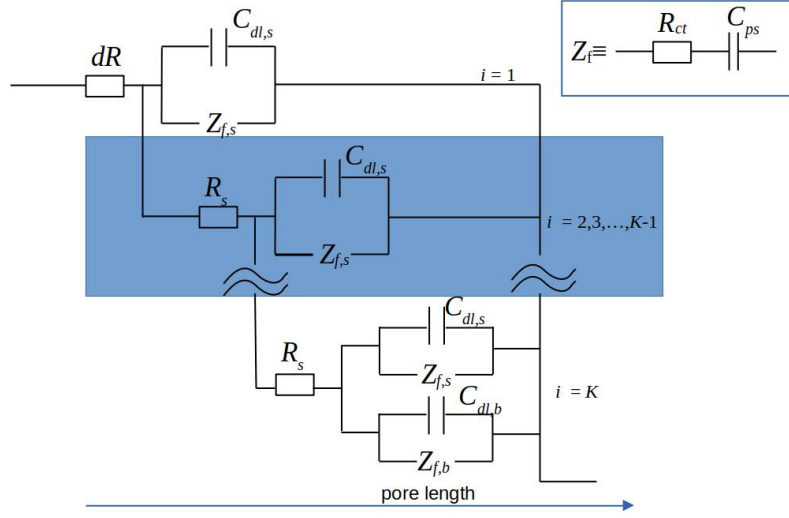


Figure 1.14: The equivalent circuit applied in the generalized staircase model. The highlighted area corresponds to the repetitive pattern of the circuit. The inset depicts the model of the faradaic impedance related to the pseudocapacitance.

the total impedance of the segment walls is given by the following equation:

$$\frac{1}{\vec{Z}_s} = \frac{1}{i\omega C_{dl,s}} + \frac{1}{\vec{Z}_{f,s}}, \quad (1.27)$$

$$C_{dl,s} = C_s \cdot A_s = C_s \cdot \pi d_p \frac{l_p}{K}. \quad (1.28)$$

The faradaic impedance $\vec{Z}_{f,s}$ is related to the pseudocapacitance and modeled as a serial combination of the charge transfer resistance $R_{ct,s}$ and the capacitance $C_{ps,s}$ (see the inset of Fig.1.14).

$$\vec{Z}_{f,s} = R_{ct,s} + \frac{1}{i\omega C_{ps,s}}. \quad (1.29)$$

Both $R_{ct,s}$ and $C_{ps,s}$ are calculated for the whole surface area A_s of the segment walls:

$$R_{ct,s} = \frac{RT}{nFi_0A_s} = \frac{RTK}{\pi nFi_0d_pl_p}, \quad (1.30)$$

$$C_{ps,s} = C_{ps} \cdot A_s = \pi C_{ps} \frac{d_pl_p}{K}. \quad (1.31)$$

The final segment of the pore, beside the contribution from its walls (\vec{Z}_s), contains

also a contribution from the bottom ($\vec{Z}_{s,b}$). The parameters of the impedance $\vec{Z}_{s,b}$ of the bottom, namely, $C_{dl,b}$ and $\vec{Z}_{f,b}$ are calculated using the equations, same as (1.28), (1.29), (1.30), (1.31), but with the bottom surface area A_b instead of the walls surface area A_s .

Thus, the impedance \vec{Z}_K of the last segment of the pore is calculated according to the circuit in Fig.1.14 as follows:

$$\vec{Z}_K = R_s + \frac{1}{\frac{1}{\vec{Z}_s} + \frac{1}{\vec{Z}_{s,b}}}. \quad (1.32)$$

Here R_s is the resistance of the electrolyte inside the segment of the pore:

$$R_s = \frac{1}{\sigma} \frac{\delta_l}{\pi d_p^2} = \frac{l_p}{\pi \sigma d_p^2 K}, \quad (1.33)$$

where σ is the conductivity of an electrolyte.

The part of the pore containing last two segments (K and $K - 1$) has the impedance \vec{Z}_{K-1} :

$$\vec{Z}_{K-1} = R_s + \frac{1}{\frac{1}{\vec{Z}_s} + \frac{1}{\vec{Z}_K}}. \quad (1.34)$$

In general, the impedance of the part of the pore containing i segments from the bottom of the pore (i.e. segments from i to K) is calculated by the recursive equation, similar to (1.34):

$$\vec{Z}_i = R_s + \frac{1}{\frac{1}{\vec{Z}_s} + \frac{1}{\vec{Z}_{i+1}}}. \quad (1.35)$$

Thus the total impedance of a pore of the 3rd generation with K segments is equal to an impedance of the pore with all segments from 1 to K : $\vec{Z}_{3g} = \vec{Z}_1$.

Impedance of pores of the 1st and 2nd generations.

The impedance of the pores of the 1st and 2nd generations is calculated by the same generalized staircase model as for the pores of 3rd generation, except that the contribution of the impedance of the next generations are taken into account.

The interfacial impedance of each of the segments of the pores of the 1st and 2nd generations is modeled by the circuit depicted in Fig.1.15. For example, an individual pore of the 2nd generation is branched into β_{23} pores of the 3rd gener-

ation. The total impedance of β_{23} parallel pores with impedance \vec{Z}_{3g} is equal to \vec{Z}_{3g}/β_{23} . It is assumed that the branch pores are uniformly distributed over the whole length of the parent pore. Thus, each segment of a parent pore contains an average additional impedance element Z^* due to the impedance of pores of next generation. For the pores of the 2^{nd} and the 1^{st} generations this additional element is given by the following corresponding equations:

$$d\vec{Z}_{2g}^* = \frac{\vec{Z}_{3g}K}{\beta_{23}}, \quad (1.36)$$

$$d\vec{Z}_{1g}^* = \frac{\vec{Z}_{2g}K}{\beta_{12}}, \quad (1.37)$$

where \vec{Z}_{3g} and \vec{Z}_{2g} are the total impedances of an individual pore of the 3^{rd} or 2^{nd} generation correspondingly.

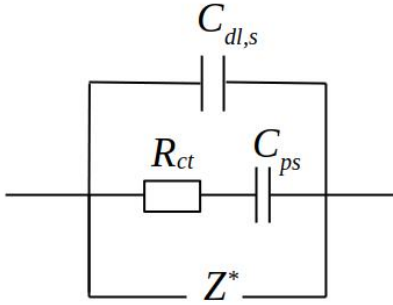


Figure 1.15: The equivalent circuit modeling the interfacial impedance of a segment of an individual pore of the 1^{st} and 2^{nd} generations.

of the calculation of the impedance of an individual pore is the same for the pores of all generations.

Finally, the total impedance of all pores of the material is calculated as the impedance of all N_1 pores of the 1^{st} generation:

$$\vec{Z}_p = \frac{\vec{Z}_{1g}}{N_1}. \quad (1.39)$$

Thus, according to the circuit in Fig.1.15, the interfacial impedance \vec{Z}_s of a segment of a pore of the 1^{st} or 2^{nd} generation, is calculated as

$$\frac{1}{\vec{Z}_s} = \frac{1}{i\omega C_{dl,s}} + \frac{1}{\vec{Z}_{f,s}} + \frac{1}{\vec{Z}^*}. \quad (1.38)$$

Physically, this approach to account for a contribution of the impedance of branch pores is equivalent to adding a branch pore with impedance equal to $d\vec{Z}_{2g}$ or $d\vec{Z}_{1g}$ to each of K segments.

(1.38) differs from (1.27) for \vec{Z}_s for the pores of 3^{rd} terminal generation by the $1/\vec{Z}^*$ term. Besides this difference, the rest

Results of modeling of impedance of porous electrode materials

The parameters of the materials of the electrode and electrolyte utilized in the calculations are listed in Table 1.4. The value of $SSA = 230 \text{ m}^2/\text{g}$ is close to the one of the carbon Vulcan XC-72, often utilized as an electrode material. This carbon black material consists of the small primary carbon particles (ca. 30 nm) filled with the micropores with an average diameter $d < 2 \text{ nm}$ [58]. The primary particles form the agglomerates with the size of 100-300 nm, which include the pores with diameters of 2-20 nm. The agglomerates form the large (μm size) chain-like structures containing the macropores with the diameter $d > 50 \text{ nm}$. Following this description, 3 types (generations) of pores of the model carbon material (see Fig.1.13) are defined in the generalized staircase model:

- micropores ($d_{p,3} = 0.7 \text{ nm}$), representing the apex and terminal branches of the inner pores inside the primary particles;
- small mesopores ($d_{p,2} = 3 \text{ nm}$), representing the major population of pores inside the primary particles;
- large mesopores ($d_{p,1} = 30 \text{ nm}$), representing the opening mouth of the smaller mesopores and the zones of contacts between primary particles.

According to the classification of Eikerling [59], the diameters of the pores of the 1st and 2nd generations correspond to the secondary and primary pores of the carbon electrode materials in fuel cells. These pores are important for efficient accessibility of the electrode/electrolyte interface. In the generalized staircase model, the micropores (3rd generation) are also added, because their presence is known to be beneficial for the performance of the supercapacitors [60]. On the other hand, the presence of a large population of macropores ($d \approx 150 \text{ nm}$)

Parameter	Value
SSA	$230 \text{ m}^2/\text{g}$
σ	2 S.m^{-1}
C_s	$5 \mu\text{F}/\text{cm}^2$
C_{ps}	$300 \mu\text{F}/\text{cm}^2$
ρ_c	$2 \text{ g}/\text{cm}^3$
m	1 g

Table 1.4: The parameters of materials used in calculations.

in Vulcan XC-72 is neglected for the simplicity of the model. These macropores make a relatively small contribution to the overall SSA of the carbon material and behave as a flat electrode under the conditions of the potential modulation utilized in the EIS measurements.

The length of the pores of the 2^{nd} and 3^{rd} generations are the variables of the model. The length of large mesopores (1^{st} generation) is fixed to $0.1 \mu\text{m}$, i.e. these pores are relatively short and represent the openings of pores within the agglomerates. The macropores branch into narrower and longer ($3 \mu\text{m}$) mesopores of the 2^{nd} generation.

In order to evaluate the performance of a porous material as an electrode in supercapacitors, the measurable capacitance of the material is calculated as $-1/\omega \cdot \text{Im}(\vec{Z}_p)$ and the surface specific calculated capacitance $C_{s,c}$ as

$$C_{s,c} = -\frac{1}{A_s \omega \cdot \text{Im}(\vec{Z})}. \quad (1.40)$$

One of the main characteristics of the supercapacitor electrode material is the mass specific capacitance C_g :

$$C_g = C_{s,c} \cdot SSA. \quad (1.41)$$

In the literature on supercapacitors, a high C_g value is often considered as a criteria of an efficient electrode material. Indeed, an efficient electrode material must have a high C_g value. However, it is not the only criterion. For example, a nm-thin film of an active storage material deposited on the current collector can demonstrate a high C_g value. However, it is the impractical material due to the high relative contribution of masses of inactive components, such as the current collector and the separator. In reality, high loadings of active material (above 1 mg/cm^2) are required. The modeling of such thick electrodes is difficult. Alternatively, for thick layers, volume specific characteristics should be analyzed [8], because they depend on both surface specific capacitance C_s and porosity of the material. Thus, the model focuses on the analysis of volume specific capacitance C_V :

$$C_V = C_{s,c} \cdot SSA \cdot \rho, \quad (1.42)$$

where ρ is a calculated density of the material:

$$\rho = \frac{m}{V_t} = \frac{m}{V_p + V_c} = \frac{m}{V_p + \frac{m}{\rho_c}}. \quad (1.43)$$

Here m is a mass of the material, V_t is a total volume of the material, V_p a total volume of the pores in the material, V_c is a volume of the compact part of the material, ρ_c is a compact density of the material (e.g. the density of a non-porous material; in the model $\rho_c = 2 \text{ g/cm}^3$, which is a typical value for the compact graphite materials). Parameters m and ρ_c are fixed model parameters (see Table 1.4), while V_p is calculated by a similar approach to A_p (eq.1.25):

$$V_p = \pi \cdot N_1(d_1^2 l_1 + \beta_{12} d_2^2 l_2 + \beta_{12} \beta_{23} d_3^2 l_3). \quad (1.44)$$

The impedance \vec{Z}_p is calculated for the wide range of frequencies f : from 0.1 mHz to 100 kHz. It is important to define the range of f , which is the most relevant for the electrode materials of supercapacitors. As it was discussed in Subsection 1.2.4, the characteristics of electrochemical performance of the supercapacitor electrode materials should be measured under the operational conditions of supercapacitors, e.g. with the charging rates above 60C [8]. For a supercapacitor with 1V operational voltage, this charging rate corresponds to the potential sweep rate of ca. 16.7 mV/s or, for galvanostatic cycling, the charging current of 2 A/g (for a capacitor with $C_g=120 \text{ F/g}$). In the case of the EIS, the rate v_E of modulation of the potential $\vec{E} = E_0 \sin(\omega t)$ is given by the equation

$$v_E = \frac{dE}{dt} = E_0 \omega \cos(\omega t). \quad (1.45)$$

According to (1.45), v_E changes periodically with time. For the sake of comparison with other methods, one can use the root mean square rate v_{rms}

$$v_{rms} = \frac{2\pi E_0 f}{\sqrt{2}}. \quad (1.46)$$

Table 1.5 shows the correspondence between the modulation rate v_{rms} and the modulation frequency f , calculated by (1.46). It can be concluded that the most relevant range of f for supercapacitors is from ca. 0.1 Hz to ca. 100 Hz (or the range of $\log_{10} f$ is from -1 to 2).

v_{rms} , mV/s	i_m , A/g	f , Hz	$\log_{10}(f, \text{Hz})$
0.1	0.01	0.0032	-2.49
0.2	0.02	0.0064	-2.19
0.5	0.05	0.016	-1.79
1.0	0.1	0.032	-1.49
2.0	0.2	0.064	-1.19
5.0	0.5	0.16	-0.79
10	1	0.32	-0.49
20	2	0.64	-0.19
50	5	1.61	0.21
100	10	3.21	0.51
200	20	6.43	0.81
500	50	16.1	1.21

Table 1.5: The values of v_{rms} and the charging current densities i_m as the estimations of the potential modulation rate for different modulation frequencies f , calculated by (1.46).

Below the influence of various structural parameters of a porous system on its electrochemical properties, in particular, C_V , is analyzed. In order to decrease the number of varied parameters, the diameters of different generations of the pores d_1, d_2, d_3 , and the length of the 1st generation of pores l_1 are fixed. Thus, the model is focused on the influence of l_2 and l_3 , as well as the total pore length and the branching factors β_{12}, β_{23} .

Simple model systems: influence of pore diameter, geometry, and branching

At first, the generalized staircase model was applied to the simple configurations of pores depicted in Fig.1.16. The results of the calculations with the model systems A, B, and C, containing 1 type of pores ($\beta_{12} = \beta_{23} = 0$), are shown in Fig.1.17. The pore length was $l = 3.2 \mu\text{m}$. The results are presented as the Nyquist plots of impedance ($-\text{Im}(\vec{Z})$ vs. $\text{Re}(\vec{Z})$), and the Bode plots of C_V .

The Nyquist plots demonstrate the expected transition from $\phi = 45^\circ$ at the frequencies higher than the threshold value f_0 to $\phi = 90^\circ$ at the frequencies $f < f_0$. The threshold f_0 decreases with the pore diameter (1.23). In the Bode plots one observes the transition from the constant C_V at $f < f_0$ to the varying C_V , which decreases with the frequency $f > f_0$. As expected, the narrower pores have higher C_V values due to the higher density of the material: $\rho = 1.513 \text{ g/cm}^3$ for $d = 0.7 \text{ nm}$, $\rho = 0.136 \text{ g/cm}^3$ for $d = 30 \text{ nm}$. The narrower pores also have a lower threshold frequency f_0 and a stronger C_V loss with increase of f . Thus, at certain

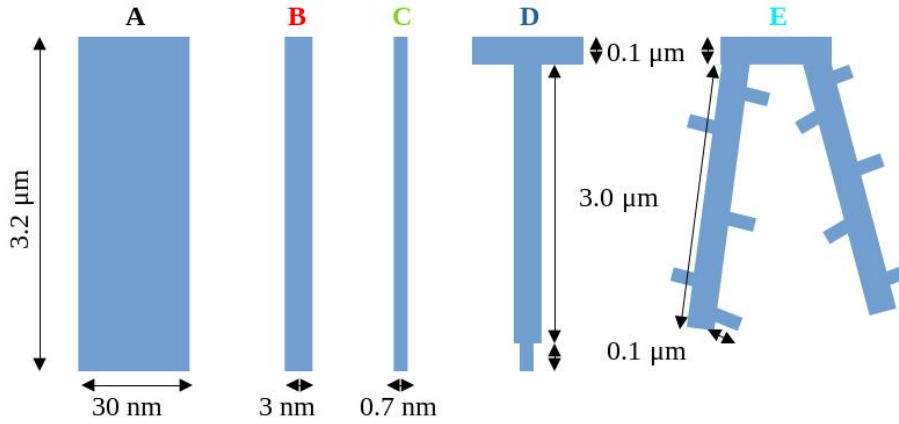


Figure 1.16: The sketches of the simple pore model systems.

$f > f_0$, for the pores with $d = 3$ nm the C_V values are predicted to be higher than the C_V values for the pores with $d = 30$ nm, Fig.1.17(B).

In order to validate the model, these results were compared with calculations for the model system with 3 generations of non-branching ("consecutive") pores ($\beta_{12} = \beta_{23} = 1$) with the same diameter $d_1 = d_2 = d_3$ (Fig.1.17). For the data in Fig.1.17, the lengths of the pores of the 1st, 2nd, and 3rd generations were $l_1 = 0.1$ μm , $l_2 = 3$ μm , $l_3 = 0.1$ μm . The total length of a single pore for the given model system was $l_p = l_1 + l_2 + l_3 = 3.2$ μm , which is the same as in the model with 1 generation of pores.

As expected, the results of the calculations for these 2 models coincide well with a slight negligible deviation observed in the Nyquist plots only for low frequencies. This slight deviation characterizes a small and acceptable inaccuracy of the model with 3 generations related to the uniform spreading of the impedance of branch pores over the length of a parent pore.

It was also verified that if all 3 generations of non-branching pores have the same diameter, then the results were the same for all models with the same total pore length, independently of the relative lengths of pores of each generations. Indeed, the results of calculations for the model system with $l_1 = 3$ μm , $l_2 = l_3 = 0.1$ μm coincide with the results for the model systems with $l_1 = l_3 = 0.1$ μm , $l_2 = 3$ μm , and $l_1 = l_2 = 0.1$ μm , $l_3 = 3$ μm .

The results for the model system D with non-branching pores, the diameters $d_1 = 30$ nm, $d_2 = 3$ nm, $d_3 = 0.7$ nm, the lengths $l_1 = l_3 = 0.1$ μm , $l_2 = 3$ μm , are

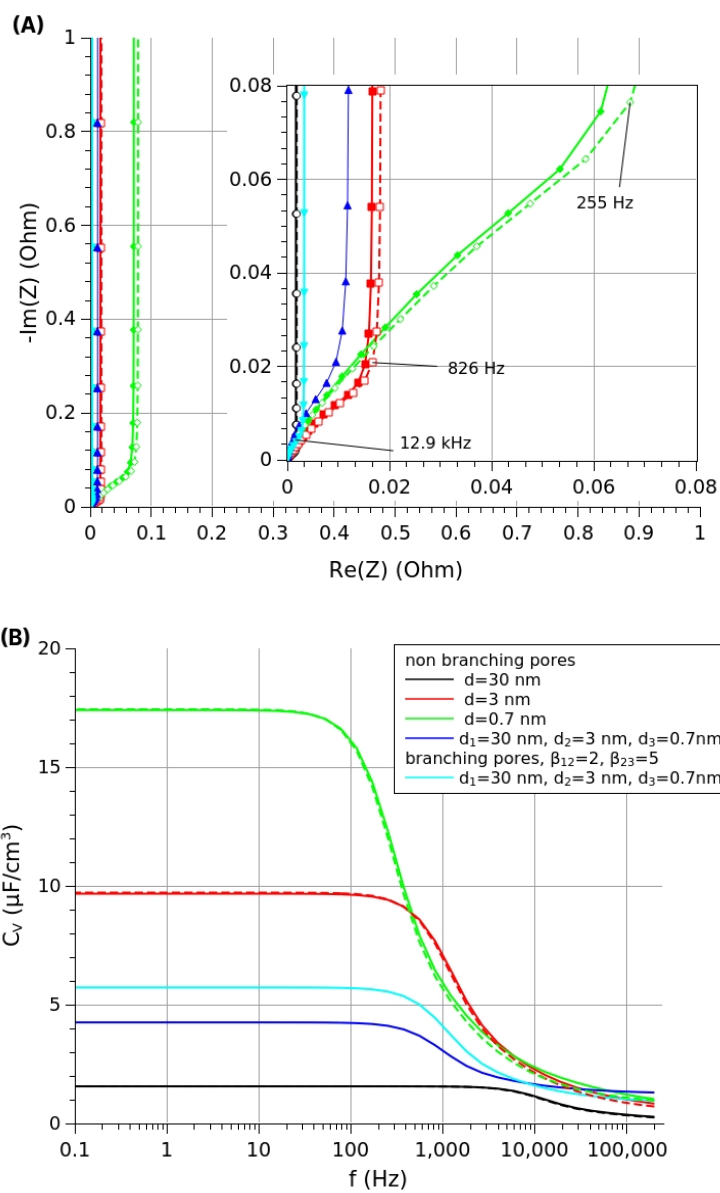


Figure 1.17: The Nyquist plots (A) and the Bode plots (B) of the model systems. Dashed lines: the model systems with 1 generation of pores ($\beta_{12} = \beta_{23} = 0$) and various pore diameter d . Solid lines (except blue and cyan): the model systems with 3 generations of non-branching pores ($\beta_{12} = \beta_{23} = 1$) and the same pore diameter d . Blue lines: the model system with non-branching pores and decreasing pore diameters. Cyan line: the model system with branching factors $\beta_{12} = 2, \beta_{23} = 5$ and decreasing pore diameters.

shown in Fig.1.17 as blue lines. The Nyquist plots for this model system show a more complex behavior, indicating the influence of all 3 generations of the pores. The phase shift angle ϕ is larger than 45° even at relatively high frequencies, while the transition to the behavior with $\phi = 90^\circ$ is less sharp comparing to the system with $d = 3$ nm (red lines). Such behavior of the Nyquist plots is similar to the one predicted for the conical pores with decreasing diameter [55].

In comparison to the system B with straight pores, the system D with a wide opening has a significantly lower density (0.841 and 0.372 g/cm³ correspondingly). Thus, the system D shows the lower C_V values if the frequencies f are not too high. The threshold frequency f_0 for this system is close to the model system B with $d = 3$ nm (red line), despite of the narrower apex of the pores of the system D ($d_3 = 0.7$ nm). A narrower apex is expected to result in a lower f_0 , however, this effect is weak and undetectable. On the other hand, due to a wider mouth of the pore $d_1 = 30$ nm, the C_V decrease in high frequency range is significantly lower in comparison to the system B ($d = 3$ nm). Above a certain frequency, the C_V values of the system D with a wide opening are bigger than those of the system B with the straight pores.

Finally, the results for the model system E with the same dimensions of 3 generations of pores as in system D, but with the branching factors $\beta_{12} = 2$ and $\beta_{23} = 5$ are shown in Fig.1.17 (cyan lines). As a branching pore has a higher surface area than a non-branching pore, the number of pores in the system E is lower than in the system D. This results in a higher density (0.498 and 0.372 g/cm³ correspondingly), and, thus, higher C_V values. Also, the value of the threshold frequency f_0 of the system E falls in the interval between the values for the systems with 1 generation of pores and the diameters $d = 3$ and $d = 30$ nm. This proves that the modeled branching porous structure is more favorable for efficient surface utilization than a non-branching structure at least in the considered frequency range. The increased efficiency can be qualitatively explained by the fact that for the same frequency f , and thus, the same penetration depth λ , the system with $\beta_{12} = 2$ has ca. 2 times higher surface area than a system with non-branching pores. However, for high frequencies, the efficiency of non-branching pores becomes comparable with branching pores. This can be explained by a stronger contribution of the wider mouths of pores to the total pore surface area in the non-branched pores.

Summing up, the following preliminary conclusions can be made from the com-

parison of the models A-E.

- Straight and narrow (micro-)pores provide the highest interfacial capacitance at least at moderate potential modulation rates. For the applications requiring high power output (fast discharging rates), narrow mesopores might be more efficient.
- The presence of wide opening of the pores ("hierarchical" pores: wider pores transforming to the narrower ones) results in the smaller losses of capacitance with the potential modulation rate increase. However, the material density and the related C_V values decrease. Thus, the wide opening of the pores might be not favorable for the applications requiring a high energy density.
- Comparing to a system with non-branching pores, the system with branching pores and the same pores dimensions has a similar dependence of capacitance on the modulation rate. However, pores branching results in a higher material density (lower porosity) for the same SSA and higher C_V values. Therefore, the branching of pores appears to be favorable for the better material performance as supercapacitor electrodes.

In the next Subsection the influence of the structure of porous systems, namely, the pores diameter, length, and branching factors on the material performance is analyzed in details.

Effect of pore "mouth"

First, the systems with the same total length of the non-branching pores $l_p = l_1 + l_2 + l_3 = 1.2 \mu\text{m}$ were modeled (see Fig.1.18). The system (F1) with the straight micropores with the diameter $d = 0.7 \text{ nm}$ was compared to the systems (F2-F4) with wide pore openings, modeled as short ($0.1 \mu\text{m}$) segments with various diameters at the mouths of pores. The comparison of the results for the systems F1-F4 is given in Fig.1.19.

The Nyquist plots of the system with straight pores with $d = 0.7 \text{ nm}$ (black lines in Fig.1.19) show the typical behavior described in the Subsection 1.3.3: a transition from $\phi = 45^\circ$ at $f > f_0$ to $\phi = 90^\circ$ at $f < f_0$. For the same threshold f_0 , the Bode plots show the transition in C_V behavior: from the independence of f for $f < f_0$ to the decrease with increasing f for $f > f_0$.

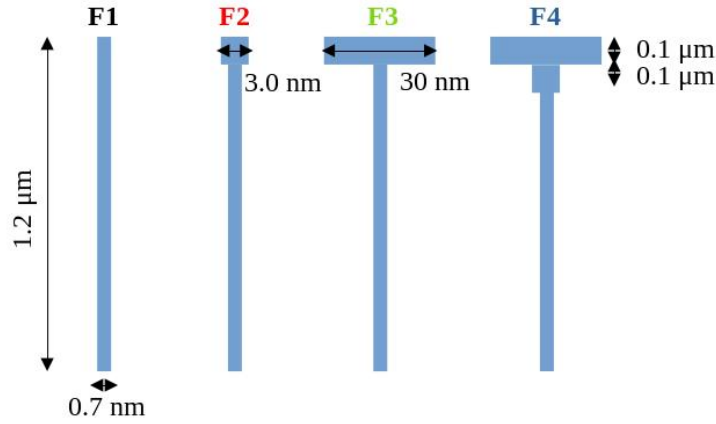


Figure 1.18: The sketches of the pore model systems F1-F4.

Adding the short wide opening segments to the mouths of the pores shifts f_0 to slightly higher frequencies and decreases the loss of C_V at higher f . These effects are stronger for wider openings. On the other hand, the presence of a wide opening increases a material porosity and decreases a material density: $\rho = 1.51$, 1.23 and 0.175 g/cm^3 for the systems F1 (no wider opening), F2 (opening segment with $d = 3 \text{ nm}$) and F3 (opening segment with $d = 30 \text{ nm}$) correspondingly. This results in a lower C_V values at low and moderate frequencies. Thus, under the low and moderate potential modulation rates the pores without wide openings are more favorable for supercapacitors.

Influence of pore branching

In order to evaluate the effect of pore branching on the capacitance of porous materials, the set of systems with pores of the same dimension ($l_1 = 0.1 \mu\text{m}$, $d_1 = 30 \text{ nm}$, $l_2 = 3.0 \mu\text{m}$, $d_2 = 3 \text{ nm}$, $l_3 = 0.1 \mu\text{m}$, $d_3 = 0.7 \text{ nm}$) and varied branching factors was modeled. The first set (G) had fixed $\beta_{23} = 5$ and varied β_{12} from 1 to 100, and the second set (H) had fixed $\beta_{12} = 5$ and varied β_{23} from 1 to 100 (Fig.1.20). The Bode plots are shown in Fig. 1.21. For all model systems very close values of f_0 were obtained, close to one of the system B (pores with $l = 3.2 \mu\text{m}$, $d = 3 \text{ nm}$, Fig.1.17, red lines). The increase in branching factors increases the loss of C_V at high potential modulation rates. However, it also increases the density of the material. For example, for $\beta_{23} = 5$ the increase in β_{12} from 1 to 10 and further up to 100 results in the increase in the material density from 0.375 to

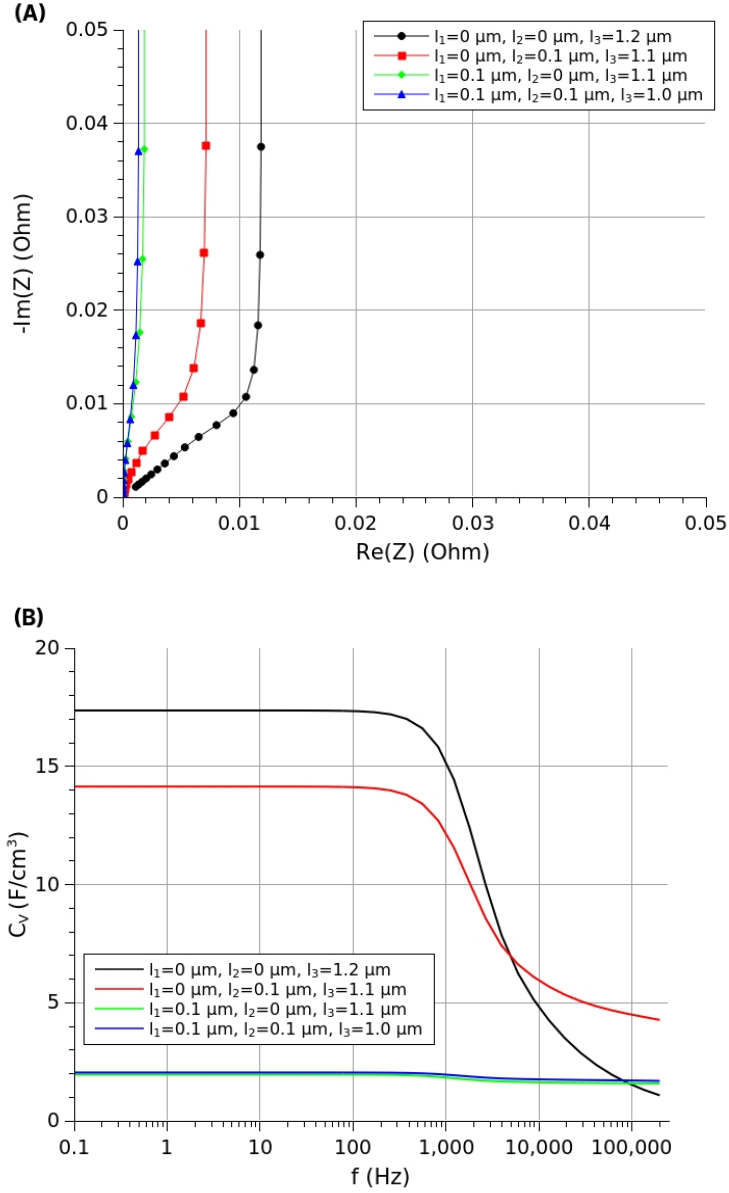


Figure 1.19: The Nyquist plots (A) and the Bode plots (B) of the model systems with 3 generations of non-branching pores with the diameters $d_1 = 30 \text{ nm}$, $d_2 = 3 \text{ nm}$, $d_3 = 0.7 \text{ nm}$. The relative lengths of the segments were varied, while the total pore length was kept constant $l_p = l_1 + l_2 + l_3 = 1.2 \mu\text{m}$.

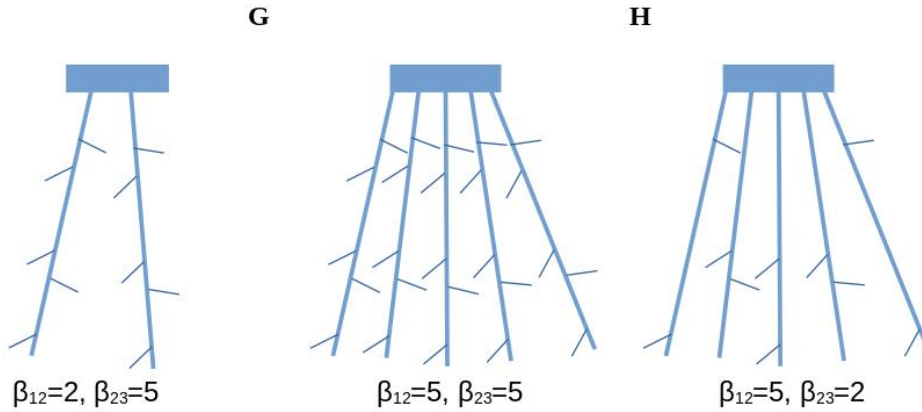


Figure 1.20: The sketches of the model system sets G and H.

0.734 and further up to 0.840 g/cm³.

It may seem to be counter-intuitive that a system with stronger pore branching has a higher density. However, it can be rationalized as follows. Pore branching results in higher surface area of each individual pore, and thus, for the same SSA, a smaller amount of pores is required. This means the lower porosity and the higher density of the material. The effect of an increased material density is predominant in the wide range of f . Only at very high f (above 10 kHz) the materials with a lower β_{12} demonstrate a higher C_V . For the increase of β_{23} , the effect of stronger C_V loss at higher frequencies is even less pronounced. This is explained by the fact that the contribution of terminal pores is smaller at the higher frequencies due to the short modulation penetration depth.

Thus, it can be generally concluded that pore branching is a favorable strategy to increase the capacitance of porous materials for supercapacitors with non-faradaic impedance, for example for the EDLC.

Below the model predictions for the systems with faradaic impedance are evaluated. These systems are relevant for the electrode materials for pseudocapacitors.

Influence of faradaic impedance

The generalized staircase model was applied to calculate the impedance of porous electrodes with faradaic impedance involved in energy storage. The interfacial impedance in this case was modeled as the impedance of a parallel connection of the capacitive impedance $Z_{dl} = Z_{C=C_{dl}}$ and the faradaic impedance $Z_f = R_{ct} +$

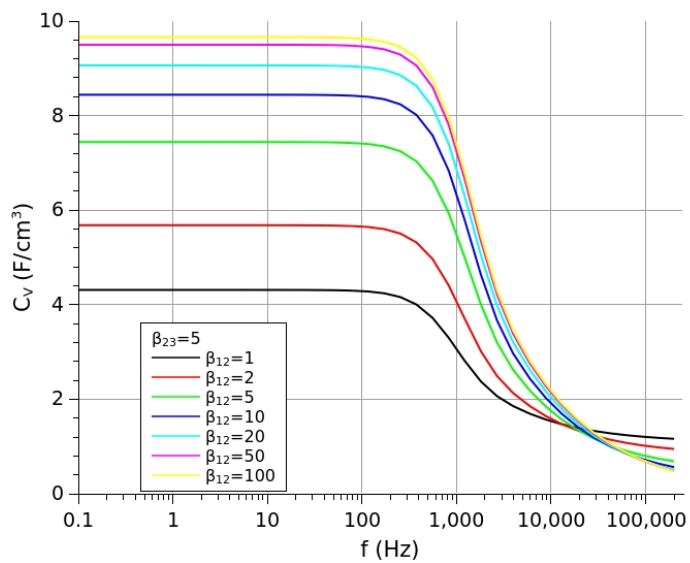
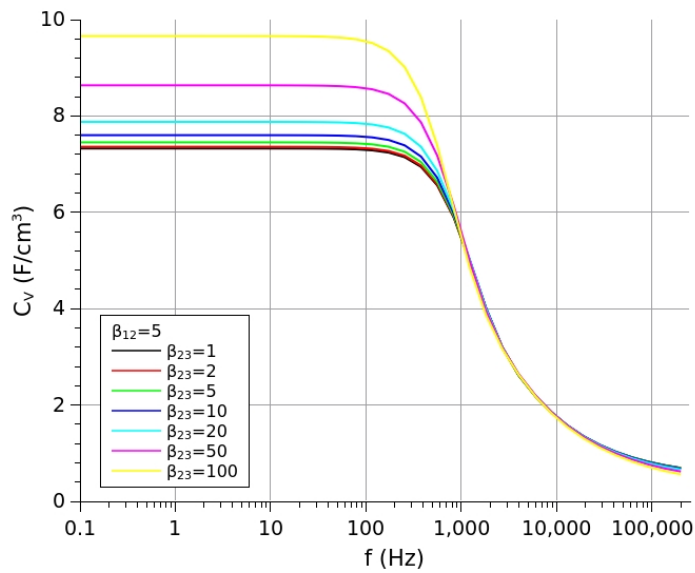


Figure 1.21: The Bode plots for the systems G with varied β_{12} (A) and the systems H with varied β_{23} (B). The lengths of the pores are: $l_1 = 0.1 \mu m$, $l_2 = 3.0 \mu m$, $l_3 = 0.1 \mu m$.

$Z_{C=C_{ps}}$ (Fig.1.14). The Nyquist plots clearly shows the influence of the faradaic impedance, especially at low frequencies, even for the relatively low values of i_0 (the exchange rate of electrochemical reaction), i.e. for the relatively high R_{ct} (1.16). As the rate i_0 increases, the predominance of \vec{Z}_f over \vec{Z}_{dl} becomes pronounced also at the higher frequencies. However, the Bode plots show that the contribution of C_{ps} becomes significant only for high i_0 and for low or moderate frequencies. For example, for the system with a very fast charge transfer rate ($i_0 = 50 \text{ mA/cm}^2$) and high $C_{ps} = 300 \text{ }\mu\text{F/cm}^2$, the contribution of C_{ps} becomes noticeable only at $f < 100 \text{ Hz}$, even though the $|\vec{Z}_{dl}| > |\vec{Z}_f|$ already at $f < 1000 \text{ Hz}$. Fig.1.23 compares the Nyquist and the Bode plots for the porous systems with the varied branching factor β_{23} , while $\beta_{12} = 2$ was fixed. The Nyquist plots are practically identical, except slight deviations observable in the high frequency range (see inset of Fig.1.23(A)). It has to be reminded that data in the Nyquist plots, namely, $-\text{Im}(\vec{Z}_p)$ vs $\text{Re}(\vec{Z}_p)$, do not reflect the changes in material porosity. This shows that the influence of branching factor on the total impedance in the presence of the faradaic impedance is negligible. It can be explained by the fact that faradaic impedance becomes predominant in the low frequency range, where the penetration depth λ is close or larger than the pore length l_p and the effects of pore geometry are weak. In this case, one may expect that the main effect of branching factor increase on the capacitance of the materials with faradaic impedance is related to the changes in the material porosity and density. Indeed, the Bode plots in Fig.1.23 demonstrate a significant increase in the values of C_V related to the increase of the material density from $\rho = 0.486 \text{ g/cm}^3$ for $\beta_{23} = 1$ to $\rho = 0.663 \text{ g/cm}^3$ for $\beta_{23}=100$.

1.4 Conclusions

It was demonstrated that the generalized staircase model allows to model the impedance of the porous materials with relatively complex pore geometry. The pore geometry can include a system of hierarchial pores, e.g. pores with a wider diameter transforming into single narrower pores or branching into multiple narrower pores evenly distributed over a parent pore. Modeling of the interfacial impedance of an individual pore can be done by splitting a pore into small segments and using the recursive equations to calculate the impedance of a part of a pore by sequentially including all segments of the part. The generalized staircase

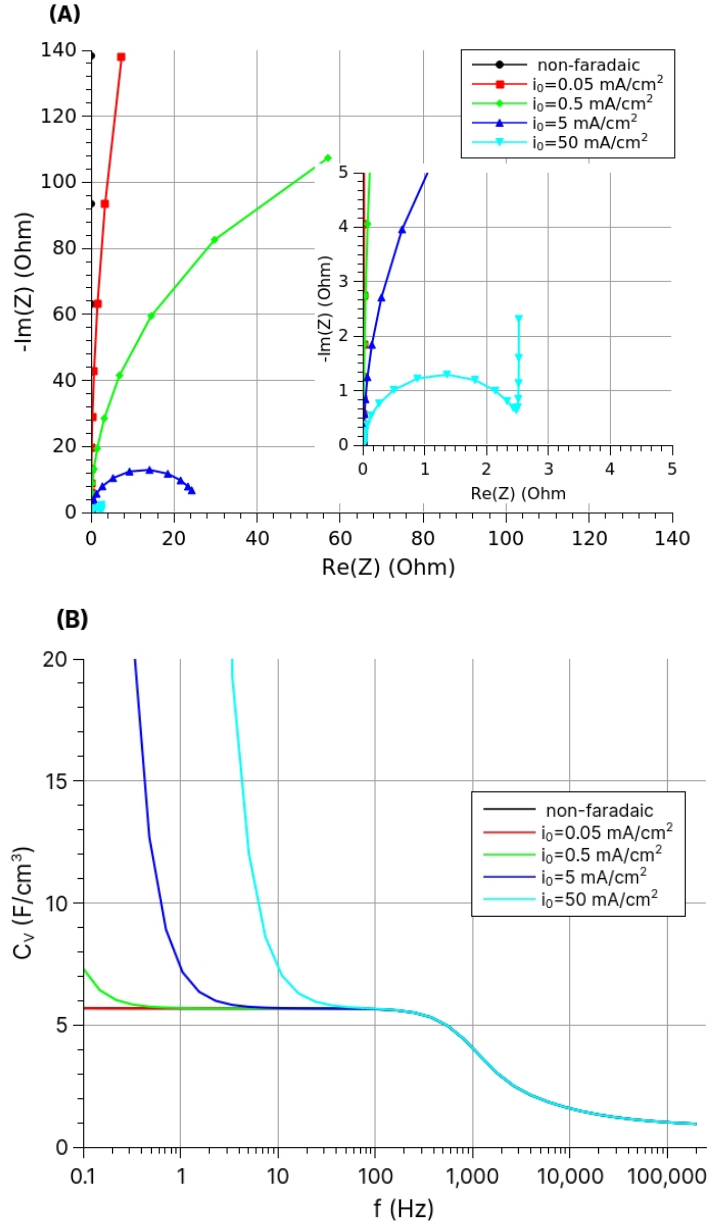


Figure 1.22: The Nyquist plots (A) and the Bode plots (B) for the model system with typical structural parameters: $d_1 = 30 \text{ nm}$, $l_1 = 0.1 \text{ }\mu\text{m}$, $d_2 = 3 \text{ nm}$, $l_2 = 3 \text{ }\mu\text{m}$, $d_3 = 0.7 \text{ nm}$, $l_3 = 0.1 \text{ }\mu\text{m}$, $\beta_{12} = 2$, $\beta_{23} = 5$, in the presence of the faradaic impedance.

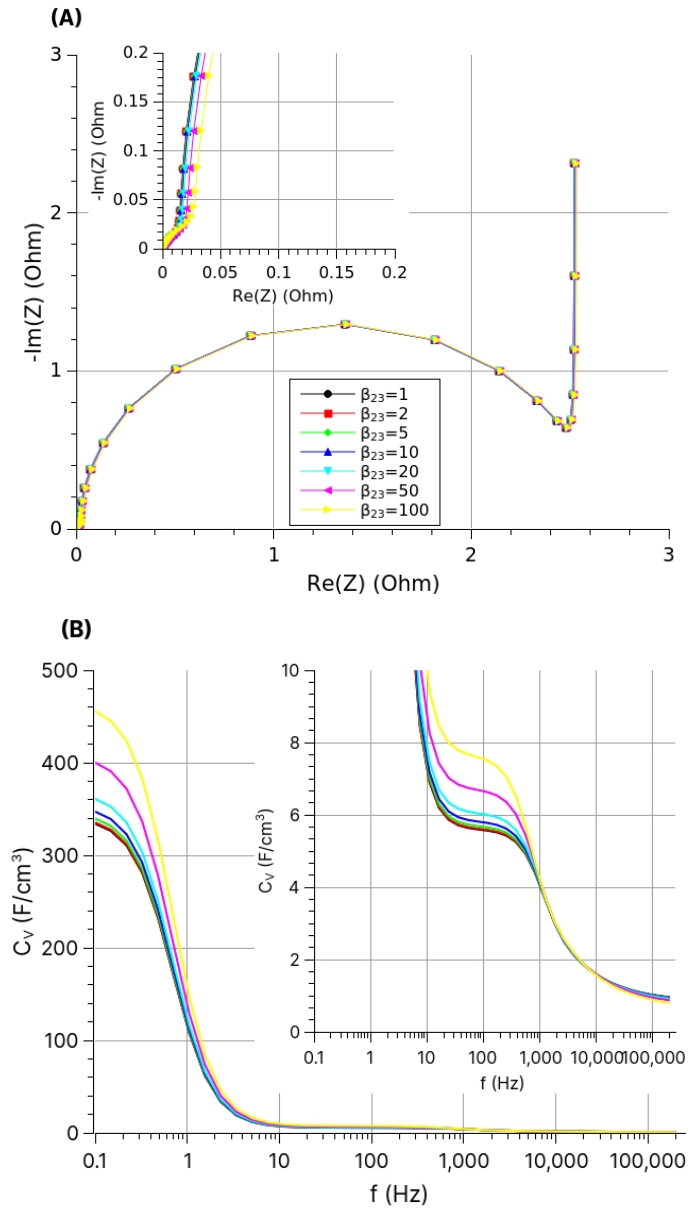


Figure 1.23: The Nyquist plots (A) and the Bode plots (B) for the model system with faradaic impedance ($C_{ps} = 300 \mu\text{F}/\text{cm}^2$, $i_0 = 50 \text{ mA}/\text{cm}^2$) for the varied branching factor β_{23} ($\beta_{12} = 2$ was fixed).

model allows to calculate the impedance of a single pore and the total impedance of all pores for the material with both non-faradaic and faradaic processes.

The generalized staircase model was developed to evaluate the influence of structural parameters of the porous electrode materials on their electrochemical performance in supercapacitors. It was demonstrated that the volume specific capacitance C_V serves as an informative parameter of the electrochemical performance.

The variation of the structural parameters of the model porous systems causes two groups of effects on the capacitance of materials.

The first group of effects is related to the limited depth of the penetration of potential modulation. These effects are manifested as a decrease in capacitance at modulation frequencies above the threshold value f_0 . Both the magnitude of this decrease and the value of f_0 depend on the structure of a porous system. In particular, a decrease in the pore diameter and an increase in the pore length result in the stronger loss of C_V and an increase of the value of f_0 . Thus, the electrochemical performance of the material decreases. On the other hand, a wider opening of pores (e.g. hierarchical pores) decreases the loss of C_V at high frequencies.

The second group of effects is related to the change in material density caused by the changes in the parameters of a porous system. A higher porosity results in a lower density of the material, a lower volume specific capacitance and a lower energy density. These effects are often counter-acting the effects of the first group.

The generalized staircase model allows to evaluate the influence of these two groups of effects and detect the predominant effect for a chosen set of the structural parameters. It was observed that too wide opening of the pores results in a strong density decrease and lower values of C_V . On the other hand, an increase in pore branching results in the predominant effect of an increase in material density and, thus, in higher values of C_V . The latter effect is the most important effect for the capacitor electrode materials with faradaic interfacial reactions, i.e. pseudocapacitors. The faradaic impedance is predominant at lower rates of potential modulation (low f), where the effects of the first group are weak.

The results of the modeling provide the guidelines for the focused design of electrode materials with high performance in EDLC and pseudocapacitors.

In Chapters 2 and 3 the two main classes of materials for the electrodes of supercapacitors, namely, carbon-based materials and transition metal oxides are discussed in details.

Chapter 2

Carbon electrode materials

As mentioned above, the carbon-based materials are most often used for the electrodes of supercapacitors. There are several advantages of using carbon materials for the electrochemical energy storage.

- Carbon is an abundant element (12th most abundant element on Earth) and can be synthesized from various fossil or bio-sources.
- Carbon has the lowest electrical resistivity among all non-metal elements. For example, graphite resistivity in the plane-parallel direction is equal to $0.4 \mu\Omega \cdot \text{m}$ (in the plane-perpendicular direction is larger than $40 \mu\Omega \cdot \text{m}$) [61]. This in plane resistivity is just a few times higher than the typical resistivity of transition metals (e.g. $0.096 \mu\Omega \cdot \text{m}$ for Fe) and ca. 10 times higher than that of coinage metals (e.g. $0.017 \mu\Omega \cdot \text{m}$ for Cu).

The conductivity of carbon is provided by the $\pi - \pi$ electron conjugation in the ordered sp^2 carbon sheets. Thus, the carbon conductivity is related to the ratio of sp^2 and sp^3 carbon and the size of the ordered sp^2 domains which form the graphene sheets. The conductivity of carbon materials spans from ca. $10^5 \Omega^{-1} \cdot \text{cm}^{-1}$ for the defect-free graphene sheet to ca. 10^{-15} for the diamond.

- Carbon is a light element: the density of graphite is 2.267 g/cm^3 , which is comparable to the density of Al (2.70 g/cm^3) and is lower than the densities of all transition metals. For carbon materials one has to distinguish between the density of carbon element (the above given value) and the apparent density of carbon materials. The apparent density is often much lower than the

density of carbon element due to the porosity or granular structure of carbon materials. For example, the typical densities of activated carbons are 0.6-0.8 g/cm³ [61].

- The structure of carbon materials can be strongly varied on the levels of its macro-, micro-, and nano-structures. In particular, carbon materials can be prepared in the form of powders, paper-like tissues, sheets, amorphous solids etc., i.e. with different macrostructures. Furthermore, carbon materials exist in the form of nanoparticles, nanofibers, nanotubes, atomically thin layers, nanosheets etc., i.e. in different nanostructures. Such variability of carbon materials provides possibilities for optimization of their structure according to the demands of a particular application. For example, in the EDLC, the charge is stored at the electrode/electrolyte interface. Thus, a high SSA, which is accessible for an electrolyte, is required for the best performance of carbon as EDLC electrode. The SSA of carbon materials can be as high as 3000 m²/g. However, one has to take into account that the surface specific charge capacitance has a complex dependence on the SSA, which will be discussed in more details below.

Carbon can be found in various allotropies: sp³ (diamond structure), sp² (graphene sheet or graphite basal plane), distorted sp² (fullerene structure), sp¹ (carbyne structure) [62]. Carbon easily forms the oligo- and polymeric chains giving rise to the vast variability of existing carbon structures: both natural (diamond, graphite, coal, tars, etc.), and engineered. The author suggests to classify these various structures according to their architectures as 0D, 1D, 2D and 3D materials. Below the examples of the characteristic structures of are described with particular attention to the materials relevant for the EESD applications.

2.1 0D-carbon

Carbon nano-onions (CNO) or onion-like carbon (OLC) [63] are the examples of the 0D-carbon. CNO can be obtained by the high temperature annealing (1500-2000°C) of nanodiamonds (produced by the detonation synthesis) under inert atmosphere or in vacuum. CNO consists of concentric carbon spheres with the diameters less than 10 nm. The typical SSA of CNO is less than 500 m²/g. The high temperature annealing results in the graphitization of carbon. As a result,

CNO materials have a high conductivity, a low defect density, and a relatively low surface specific capacitance ($\approx 4 \mu\text{F}/\text{cm}^2$) and mass specific capacitance ($\approx 2 \text{ F/g}$). Considering the low specific capacitances and the high production costs, CNO represent a little practical interest for the energy storage applications. However, it is an interesting model electrode material with a well controlled and regular porosity.

2.2 1D-carbon

Carbon nanotubes (CNT) and nanofibers (CNF) are the examples of the 1D-carbon. This is one of the most widely studied type of carbon materials for supercapacitor electrodes. There are numerous methods of synthesis of CNT/CNF, including the chemical vapor deposition via the decomposition of hydrocarbon precursors [7]. This method offers a preparation of ordered (vertically aligned) nanotubes electrode with a relatively easy scale-up to mass production.

The main advantage of using 1D-carbon materials as electrodes is their controlled porosity (with predominant presence of mesopores), especially in the case of vertically aligned nanotubes or nanofibers. There are numerous studies demonstrating the possibility of the fine control on the geometry and the composition of carbon nanotubes. This makes CNT a very suitable model material to study the influence of various structural parameters on the performance in supercapacitor electrodes.

On the other hand, the disadvantage of CNT is a relatively low SSA (less than $250 \text{ m}^2/\text{g}$) of the as-synthesized materials, resulting in a low mass specific capacitance. However, the mass specific capacitance can be significantly increased by the chemical post-treatment, due to the increase in SSA and carbon surface functionalization. In particular, the introduction of the O- and N-containing surface groups allows to improve the accessibility of pores for aqueous electrolytes and increases the contribution of pseudocapacitance due to the redox transformations related to these groups [64]. The optimization of geometry and composition of CNT allows to increase the SSA up to $500 \text{ m}^2/\text{g}$ resulting in the mass specific capacitance equal to 203 F/g .

Carbon nanotubes and nanofibers are often utilized in combination with metal oxides and/or conductive polymers as the components of the composite electrodes for supercapacitors [65]. The reason is the regular controllable structure of carbon

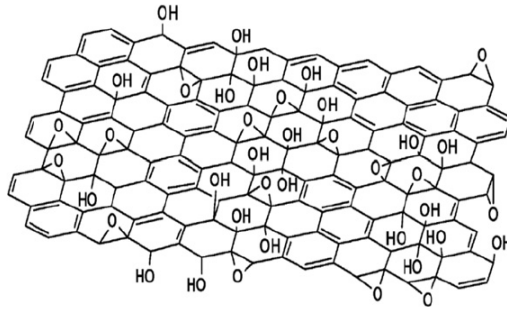


Figure 2.1: The Lerf-Klinowski chemical model of GO produced by the chemical oxidation of graphite [68].

nanotubes, namely, their geometry, porosity, surface and bulk composition. As mentioned above, the modification in chemical composition allows to increase the intrinsic charge capacitance of carbon nanotubes due to the pseudocapacitance reactions. The introduction of heteroatoms (N, S) also allows to create the adsorption sites for metal precursors, thus, facilitating the synthesis of metal oxide / carbon composites.

2.3 2D-carbon

Graphene is the 2D carbon material which consists of the separated (exfoliated) sheets of sp^2 -carbon. This material has a high mechanical stability: the Young modulus of a defect-free single graphene sheet is equal to 1.0 TPa and break stress is equal to 130 GPa [66]. Graphene has a high theoretical SSA equal to 2630 m^2/g [67]. The single sheet graphene is characterized by a relatively low surface resistance 400 Ohm/sq, which is decreased to 30 Ohm/sq for the film of 4 graphene sheets with thickness of ca. 2 nm [68]. The bulk conductivity of such graphene-type film is estimated to be ca. $1.6 \cdot 10^5 \text{ Ohm}^{-1} \cdot \text{cm}^{-1}$.

The high electronic conductivity and mechanical stability make graphene a very attractive electrode materials for EDLC. However, there are two main challenges related to the application of graphene as an electrode material: (i) the tendency of re-stacking of graphene sheets during the deposition on the electrode and (ii) the cost of scaling-up of the synthesis of graphene above laboratory quantities.

The methods for the graphene synthesis are typically divided into two groups: the top-down methods (e.g. mechanical exfoliation, chemical and sonochemical

exfoliation) and the bottom-up methods (chemical vapor deposition (CVD)). The CVD and the mechanical exfoliation are known to produce high quality graphene films [67], however, its application is limited to non-porous substrates. Among the top-down methods, the mechanical exfoliation is the hardest method to scale up. Alternatively, the chemical exfoliation route can be easily scaled up to mass production. Below two main strategies of the chemical exfoliation methods are considered: chemical (Hummer method) and sonochemical exfoliation.

2.3.1 Chemical exfoliation of graphite

The *chemical exfoliation* consists of the chemical oxidation of graphite by the Hummer's original [69] or improved synthesis [70], producing the graphene oxide (GO). This step is followed up by the reduction of GO, either chemical or thermal, to the reduced graphene oxide (rGO) [5, 71]. The chemical oxidation of sp^2 carbon introduces the oxygen-containing functional groups (Fig.2.1) and results in the formation of the graphite oxide. The polar functional groups decrease the interaction between the graphene sheets. A hydrophilic nature of the oxygen containing groups facilitates the exfoliation in aqueous solutions. Eventually, this results in the exfoliation of graphite, often assisted by the controlled sonication of the solution. Thus, the stand-alone GO sheets suspension is formed in the solvent. The difficulty of this step of the synthesis is to tune the oxidation rate: a stronger oxidation results in a more efficient exfoliation of graphite, as well as in shorter flakes of GO with more structural defects [72].

The exfoliation efficiency is manifested by the change in the XRD of the material. The graphite shows a narrow and strong peak at $2\theta = 26.5^\circ$, corresponding to the (002) plane and the sheets separation distance equal to 3.35-3.37 Å [73]. The graphite oxidation results in the shift of this peak to $2\theta = 10^\circ$, indicating a wider separation of the graphene sheets. The chemical oxidation also induces the distortions and structural defects in the 2D-ordered graphene sheets.

These transformations are often detected by the Raman spectroscopy. The spectra of undistorted graphene contain the characteristic peaks: the G peak at ca. 1580 cm^{-1} related to the scattering of E_{2g} phonons [73] and the 2D peak at ca. 2700 cm^{-1} due to second-order boundary phonons. The relative intensity of the 2D peak is sensitive to the number of layers in the graphene stack (Fig. 2.2). Indeed, a systematic study of the Raman spectra of the graphene sheets with different

thicknesses on the atomically flat SiO₂/Si substrate demonstrated the empirical linear dependence (2.1) of I_G/I_{2D} ratio on the number of graphene layers n [74]:

$$\frac{I_G}{I_{2D}} = 0.14 + \frac{n}{10}. \quad (2.1)$$

The position and intensity of the 2D Raman band of graphene depends also on the density of strains and defects in a graphene sheet [75]. Thus, the equation (2.1) should be understood only as a rough estimate, which is useful for the comparison of the thicknesses of the graphene materials with comparable structures.

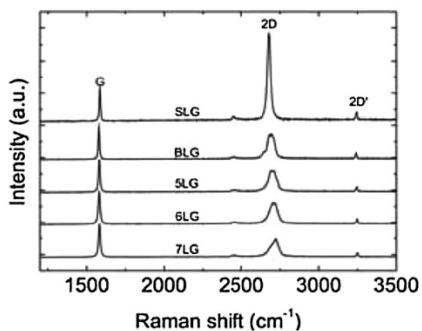


Figure 2.2: The dependence of Raman spectra of the few layer graphene stacks on the number of layers [76].

The appearance of structural defects is manifested by the intensive D peak in the Raman spectra at ca. 1320 cm⁻¹ related to the first-order boundary phonons [66, 77]. The ratio of the intensities of the D- and G-peaks, I_D/I_G , is often used to characterize the density of structural defects in graphene materials. For example, in the well-crystallized graphite, I_D/I_G lies in the range of 0.05-0.35, depending on the origin of the graphite [73]. I_D/I_G ratio increases up to 3.0-3.5 as an average distance between the structural defects L_D decreases down to ≈ 4

nm [68]. The distance L_D can be approximated as an average size of the ordered sp^2 domain. For disordered activated carbons with a high density of structural defects, the typical I_D/I_G ratio is much higher: 4.8-5.6 [77]. The formation of GO from the graphite results in a significant decrease in the conductivity due to the distortion of the $\pi - \pi$ conjugation. The surface resistance of GO is reported to be as high as 10¹² Ohm/sq. Thus, the reduction of GO is required. The reduction can be done either thermally at temperature above 750°C, or chemically by NaBH₄, N₂H₄, or electrochemically [68]. The reduction of the functional groups is necessary to re-establish a predominant population of the conductive sp^2 domains. On the other hand, the recovery of these domains increases the hydrophobicity of rGO and can trigger the re-stacking of graphene sheets. Thus, the optimal reduction ratio has to be found experimentally.

The stacking degree and the concentration of defects can be controlled by the

conditions of graphite oxidation and GO reduction [6]. According to the XPS data, the reduction of GO to rGO results in an increase in the atomic C/O ratio from 4:1-2:1 (typical for GO) to ca. 12:1 [68], which indicates that the reduction is not complete. Also, the typical I_D/I_G ratio for rGO lies in the range 0.9-1.5, which indicates the presence of structural defects in the resulting material.

From the viewpoint of the energy storage applications, the advantage of GO/rGO route is that the partially reduced oxygen-containing functional carbon groups are electrochemically reversible and add the charge storage capacitance due to the pseudocapacitance phenomena [67]. The pseudocapacitance phenomena is discussed in details in the Section (1.2.3). The challenge of the GO/rGO route is to find the optimal conditions of each of its steps. The typical SSA and the mass specific capacitance of rGO electrode materials are reported in the ranges of 400-700 m^2/g and 150-260 F/g correspondingly.

2.3.2 Sonochemical exfoliation of graphite

The *sonochemical exfoliation* of graphite allows to avoid the formation of high density of structural defects, because it relies on the presence of an exfoliating chemical agent in the sonicated liquid dispersion of graphite instead of the formation of oxygen functional groups. At the sufficiently powerful sonication, the exfoliation of graphite occurs in organic solvents, such as DMF and NMP [66] even in the absence of exfoliation agents. However, the exfoliation yield is relatively low [72]. In the last decade, the non-toxic perfluorinated organic solvents were shown to be efficient in the graphite exfoliation [76].

The exfoliating agents added to a solvent assist the exfoliation and can also act as a surfactant, stabilizing the graphene sheets and avoiding their re-stacking [67]. The variety of exfoliation agents allows to form stable aqueous and organic dispersions of partially stacked graphene sheets, most commonly with few (less than 10) layers stacked. Therefore, the resulted materials are commonly called as the few layer graphene (FLG) [76]. Mostly the expensive and toxic organic solvents are used, making scaling up of the process more difficult [72]. However, the utilisation of the bio-compatible oligopeptide exfoliating agents is reported [78], which offers the possibility for preparation of a stable aqueous dispersion of the FLG materials.

A comparison between the chemical or electrochemical oxidation/reduction

(GO/rGO) routine and the sonochemical exfoliation (FLG) demonstrated [79] that the latter has a generally lower yield and requires a longer time for the formation of comparable amount of the material. The exfoliation during the chemical or electrochemical oxidation of graphite is due to the chemical processes occurring in the bulk of carbon, such as oxidation, formation of oxygen-containing groups and, more importantly for the exfoliation, formation of gas (CO_2 and O_2) bubbles. The exfoliation during the sonochemical treatment is due to the formation of cavity bubbles located at the very vicinity of the solid/liquid interface. This results in a lower yield but a smaller damage in the graphene sheets structure.

2.3.3 Graphene-like carbon in supercapacitors

The stand alone graphene-like materials (rGO or FLG) are rarely applied in the supercapacitors due to the re-stacking phenomenon or the limited surface accessibility in the presence of surfactants [5]. In order to avoid the re-stacking, the spacers are often introduced between the graphene sheets: for example, the carbon nanotubes [80, 81] or the metal oxide nanoparticles [82, 83]. The latter belongs to the class of the composite metal oxide / carbon materials, which will be considered in details in Chapter 3.2.

The synthesis of graphene-based electrode materials by using structuring compounds (*template synthesis*) is another common and promising approach. Polymers are most commonly applied as the structuring elements [67]. The materials prepared by the template synthesis have the high SSA and conductivity of the graphene based materials and the controlled optimized porous structure of templates. Such structural design of the composite graphene/polymer electrode materials results in the outstanding capacitance at high electrode loading. For example, the stand-alone graphene/PANI foam with the loading equal to 0.90-0.96 mg/cm² demonstrated the capacitance equal to 790 F/g at the charging current $I_g = 1$ A/g [84]. The reported capacitance is higher than theoretical capacitance for the stand alone graphene (ca. 550 F/g), indicating the contribution of the polymer. It explains a ca. 20% loss of capacitance of the composite during 1 A/g cycling in 1M H_2SO_4 , while the capacitance retention of the stand alone carbon electrodes is close to 100% under the same conditions.

Alternatively, the inorganic templates can be applied to control the structure of a synthesized electrode material. For example, MgO or $\text{Mg}(\text{OH})_2$ are reported

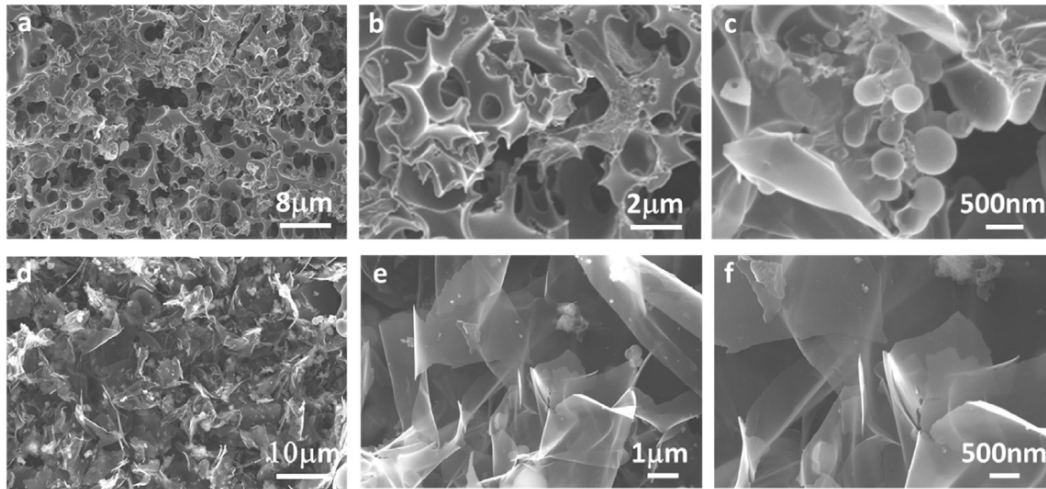


Figure 2.3: The typical SEM images of carbon material prepared by the KOH impregnation / etching technique in the absence (a-c) and in the presence of the templating NaCl agent (d-f) [10].

as template agents [85, 86]. The materials synthesized with these templates show the high specific capacitance up to 450 F/g at 0.5 A/g in 6M KOH. Contrary to the polymer/graphene composites, the retention of capacitance up to 134% was detected after 10^4 cycles at 200 mV/s, i.e. a noticeable increase in capacitance upon cycling was observed, which often occurs for carbon electrodes.

2.3.4 Case study: Graphene-like carbon from sugar/salt mixture

In this subsection the graphene-type carbon materials synthesized and tested for the supercapacitors in ICPEES with the participation of the author are discussed [10].

The graphene-like carbon materials with the ordered 2D-carbon structure were synthesized by the high temperature KOH etching of the refined sugar in the presence of NaCl as an inorganic template, which is soluble in water [10]. These material are further referred to as salt-to-sugar or the *StS* materials. Thermal KOH etching is a conventional technique to prepare the carbon materials with high SSA. An impregnation of the carbon source by KOH is followed by its thermal activation, resulting in the development of a complex porous 3D carbon structure with a high SSA up to the theoretical limit 2630 m²/g (Fig. 2.3(a-c)). The technique of thermal chemical etching is considered in details in Section 2.4.

In contrast to the conventional etching technique, the impregnation of carbon source (sugar), was done in the presence of NaCl as a templating agent. The thermal etching results in the carbon material with predominantly disordered graphene 2D-sheets, providing a high accessibility of carbon surface for an electrolyte (Fig. 2.3(d-f)). The properties of the $StS_{x/y}$ carbons depended on the mass ratio x/y of salt to sugar. The optimal ratio was found to be $x/y = 1/1$. The graphene-type structure of the carbon sheets is evident from the presence of 2D Raman peak at 2400 cm^{-1} [74]. The intensity ratio $I_G/I_{2D} \approx 5.3$ shows that the observed planes contain few tens of single graphene sheets. This fact is in agreement with a relatively small SSA of the StS , $630 - 890\text{ m}^2/\text{g}$, comparing to the SSA of activated carbons prepared by the conventional KOH etching technique.

Despite a lower SSA, the $StS_{1/1}$ carbon demonstrated an outstanding specific capacitance $C_g = 293\text{ F/g}$ in $0.5\text{M H}_2\text{SO}_4$ at 1 A/g with a very moderate decrease to 234 F/g at a higher charging rate of 50 A/g , (Fig.2.4(A)). Moreover, the capacitance retention close to 100% was observed in more than $12 \cdot 10^3$ cycles after the 11.5% capacitance increase in first 1000 cycles at 5 A/g (Fig.2.4(B)). An estimate of the surface specific capacitance of the $StS_{1/1}$ carbon (SSA= $780\text{ m}^2/\text{g}$) demonstrated a high value of $C_s \approx 38\text{ }\mu\text{F}/\text{cm}^2$, i.e. few times higher than the one expected for the double-layer capacitance of the sp^2 carbon surface. This indicates the contribution of the surface- and sub-surface pseudocapacitance phenomenon to the charge storage in the StS carbon. For example, the H intercalation into the graphitic layers can be responsible for the pseudocapacitance phenomenon. Indeed, the contribution of pseudocapacitance is manifested by the presence of a distinct pair of the CV peaks, which are centered around 0.5 V RHE (Fig.2.4(A)). These peaks are similar to the CV peaks for carbon electrodes submitted to the strong chemical oxidation, (Fig.1.7) [29]. It is important to emphasize that as the charging rate increases from 1 A/g to 50 A/g , C_s decreases only slightly from 38 to $30\text{ }\mu\text{F}/\text{cm}^2$, indicating a fast rate of pseudocapacitance processes within StS .

More details on the mechanism of the interfacial phenomena can be obtained from the impedance spectra (Fig. 2.5). The Nyquist plots demonstrate the typical behavior for a porous material in the capacitor. Namely, the transition from low $\phi < 45^\circ$ at high f to $\phi \approx 90^\circ$ at $f < 100\text{ Hz}$ is observed. The low frequency part of the Nyquist plots can be modeled by the CPE impedance with $a \approx 0.89$, which is a typical value for the carbon electrodes. In the high frequency range ($10^5 - 10^2\text{ Hz}$), one clearly observes the phase angle ϕ decreasing to the values close to or

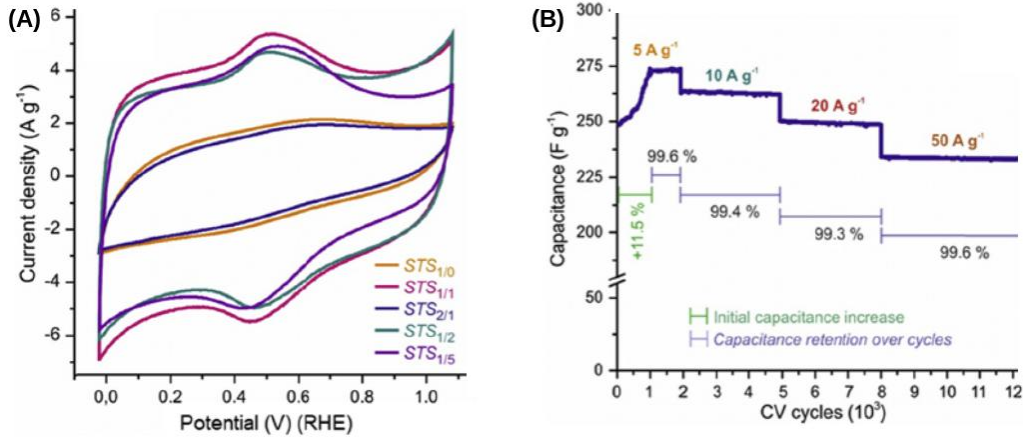


Figure 2.4: (A) The CV curves of the $StS_{x/y}$ carbon electrodes in 0.5M H_2SO_4 at 20 mV/s. (B) The dependence of the specific capacitance of the $StS_{1/1}$ electrode on the number of galvanostatic cycles applied at different charging rates [11].

even less than 45° . The low phase angle is related to the influence of porosity of StS material, as discussed in details in the Section 1.3.

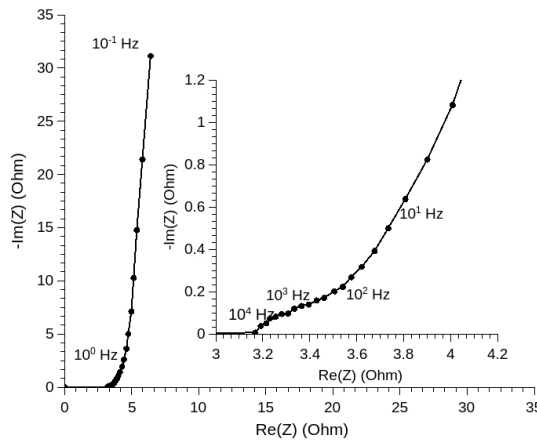


Figure 2.5: The Nyquist impedance plots of the $StS_{1/1}$ carbon electrode at the open circuit potential in 0.5M H_2SO_4 [11].

In order to support these conclusions, a more detailed study of the mechanism of pseudocapacitance in the StS carbon materials in various electrolytes is needed (see Chapter 4).

The above discussed results allows to relate the strong performance of the $StS_{1/1}$ electrodes to their structural properties. The presence of the graphitic layers appears to be important for the electrolyte ions intercalation. The presence of the oxidized carbon surface groups seems to be preferable for the strong interaction of the electrolyte species with the carbon surface. The optimal combination of these two factors is responsible for an outstanding electrochemical performance of the StS carbon

2.4 3D-carbon

The formation of the EDL is the main mechanism of charge storage in carbon electrodes of the EDLC. The charge capacitance of an electrode materials of the EDLC is determined by its accessible interfacial surface area. This parameter depends on (i) the SSA of carbon materials and (ii) the accessibility of carbon surface area for an electrolyte. According to (1.41), the mass specific capacitance C_g is linearly proportional to the SSA of carbon: the higher is SSA, the higher is C_g . This trend has been confirmed by the analysis of experimental data [28]. However, the experimental dependence of C_g on SSA is not strictly linear due to a decrease of C_s with the SSA increase. There are 2 origins of the dependence of C_s on SSA.

- In carbon materials, a higher SSA is provided by a higher volume contribution of micropores: the surface-to-volume ratio of pores increases with the decrease of their diameter d . However, as d decreases to the values below the doubled size of the solvated ions (e.g. below ca. 1 nm), the surface specific capacitance of carbon decreases down to $5 \mu\text{F}/\text{cm}^2$, because the diffusion of ions in these pores becomes more difficult [60]. However, a further decrease in pores size (below 1 nm) is expected to result in a significant increase in the surface specific capacitance (up to $15 \mu\text{F}/\text{cm}^2$) due to the distortion of ions solvation shell [60]. Another origin of the increase of surface specific capacitance is the increase in surface quantum capacitance, related to the formation and screening of the image charge in the conductor induced by the adsorbed ion [28]. Nevertheless, the experiments reported in the literature demonstrate the decrease of $C_s \approx 15 \mu\text{F}/\text{cm}^2$ for $\text{SSA} < 1000 \text{ m}^2/\text{g}$ to $C_s \approx 5 \mu\text{F}/\text{cm}^2$ for $\text{SSA} > 2500 \text{ m}^2/\text{g}$.
- It has been discussed in details in Section 1.3 that the depth of the penetration of potential modulation inside the pores decreases for a higher modulation rate and a narrower pore diameter d (see 1.23). Thus, a material with the narrower pores have a stronger loss of interfacial capacitancies C_g and C_V at higher charging rates. However, narrower pores also provide a lower porosity of the material with the same SSA, resulting in a higher material density, and, thus, a higher C_V . As it was discussed in Section 1.3, the effect of porosity is predominant in the range of potential modulation rates which is

typical for supercapacitors, both EDLCs and pseudocapacitors. Thus, the micropores are favorable for the materials with high C_g and C_V .

The activated carbons (AC) form the class of 3D carbon materials with the highest practically achievable SSA, larger than 3000 m²/g [62]. The other advantage of the activated carbons is relatively straightforward synthesis routines, which can be classified in general as (i) the physical and (ii) the chemical carbon activation methods [87].

The physical activation occurs due to the pyrolysis of a carbon source in the inert atmosphere at high temperature (800 °C or more). The resulting structure depends on the duration and temperature of the pyrolysis. The optimal temperature which provides the maximal carbon surface area, depends on the source of carbon. For example, a detailed study of the activation of the pine-derived biomass [88] demonstrated that the highest BET surface area was obtained after the pyrolysis at 600°-800°C, while further increase in the temperature resulted in a sharp decrease of the surface area. In general, 4 typical temperature domains of carbonisation were proposed [88].

- The initial structure of source was predominantly kept below 350°C, providing the predominant crystalline cellulose structure and a relatively high content of hydrogen, oxygen and other volatile elements.
- The initial degradation started above 350°C, resulting in the increase of the content of the sp^2 carbon, and a slight growth of the BET surface area and porosity.
- The formation of carbon nanocrystalline structure occurred at $\approx 500^\circ\text{C}$; resulting in the further increase in the sp^2 carbon content. In this temperature range, the maximums of the BET surface area and the volume of pores were obtained.
- At the temperature above $\approx 800^\circ\text{C}$ the graphitic structure developed, the maximum of sp^2 carbon content was reached, while the BET surface area decreased.

The first step of the chemical activation is the impregnation of carbon source with an etching agent, most typical of which are NaOH/KOH, H₃PO₄, H₂SO₄,

K_2CO_3 , $ZnCl_2$. The next step is the etching, which is performed at a high temperature but below the temperatures typical for the physical activation. Then the traces of etching agents are washed out from resulting material after its cooling. The chemical activation is preferred due to a lower activation temperature and shorter time. The porous structure of the final material is controlled by the duration of activation and the amount of etching agent.

Various sources of carbon can be used to prepare the activated carbon by the chemical activation method. From the sustainable development point of view, the utilization of natural, abundant and cheap carbon sources, such as peat, wood, or coconut shells is specially interesting for the mass production of carbon materials. In particular, the utilization of natural carbon-rich sources is a viable strategy for the biomass valorization [89]. The chemical activation of a bio-source precursor eliminates most of the elements other than carbon and creates the porous carbon structure with a well developed surface area. The structure of the final product, i.e. the activated carbon, depends on the activation parameters: namely, nature and concentration of an activating agent, temperature and duration of the activation step.

2.4.1 Case study: activated carbon from ripe fig fruit

In this subsection the 3D activated carbon materials, which were synthesized from a bio-sourced precursor in the ICPEES with the participation of the author, are discussed [11].

The utilization of bio-wastes as precursors for the porous carbon electrodes for the EESD is an attractive topic of research from the sustainable development point of view. The electrodes for the EDLCs and the Li-S batteries have been prepared from the banana peels by chemical activation [90, 87]. A fig fruit is another natural precursor for the carbon materials. It can be used as a model of various bio-wastes due to the high content of carbohydrate lignocellulose fibers.

A highly porous carbon was prepared by the KOH activation of the natural ripe fig fruit at the temperatures above $700^\circ C$ [10]. Similarly to the thermal activation, the chemical activation at a higher temperature results in a more graphitized structure. It is manifested by the appearance of the (002) XRD peak and a significantly lower I_D/I_G ratio of Raman peaks observed for the AC prepared at $900^\circ C$ in comparison to the AC prepared at $700^\circ C$ (Fig.2.6).

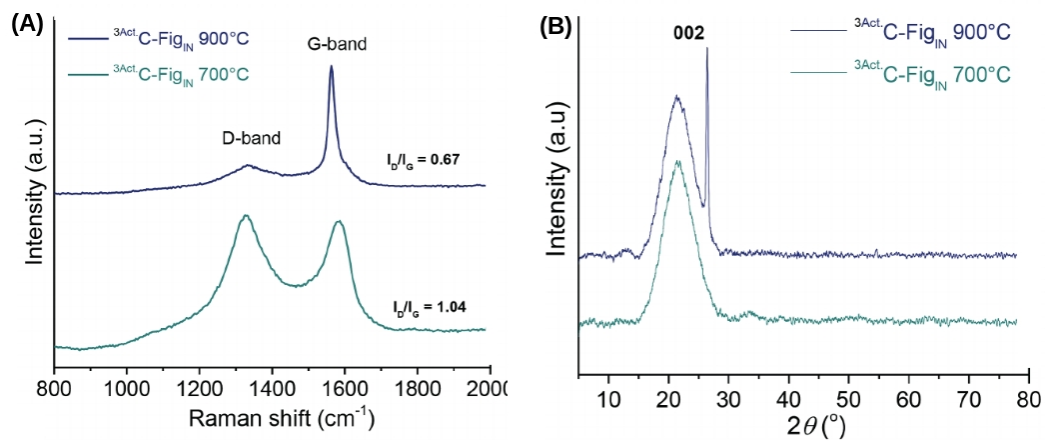


Figure 2.6: (A) The Raman spectra and (B) the XRD of the bio-sourced carbon synthesized by the KOH thermal activation at 700°C and 900°C [10].

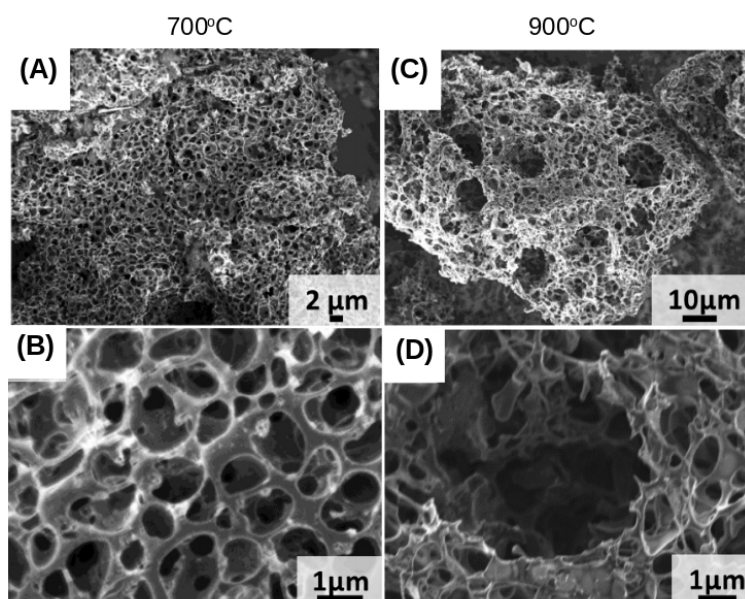


Figure 2.7: (A-D) The SEM images of the bio-sourced carbon synthesized by the KOH thermal activation at 700°C and 900°C [10].

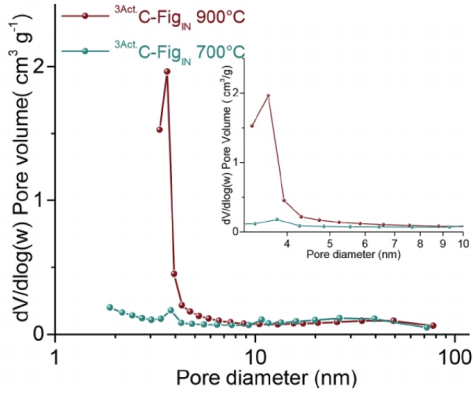


Figure 2.8: The pores distribution as measured by the BET [10].

Contrary to the physical activation, an increase of the annealing temperature of the chemical activation above 700°C results in a higher BET: 1003 m²/g at 700°C and 2337 m²/g at 900°C [10]. These high SSA values reflect a well developed porous structure (Fig.2.7). The higher SSA of carbon obtained at 900°C is related to strong contribution of micropores and small mesopores with $d < 4$ nm (Fig.2.8). The SEM images demonstrate that the pores of the AC sample prepared at

900° have the hierarchial branching structure: the wider pores are branching in several narrower pores. As concluded in Section 1.3, such structure provides a compact material with a well developed surface and is favorable for the materials with a high specific capacitance.

The electrochemical properties of the activated carbon obtained by the KOH thermochemical activation of a fig fruit are summarized in Fig.2.9. This AC material demonstrates an outstanding charge capacitance above 300 F/g in 0.5M H₂SO₄ at the charging rates below 2 A/g. Using the BET value of SSA, the surface specific capacitance was estimated as $C_s = 13 \mu\text{F/g}$, which is a value expected for carbon/electrolyte interface. It allows to conclude that:

- the EDL charging is the main mechanism of charge storage for the studied AC material,
- the utilization of an entire surface of the studied AC material is close to 100% because of the well developed open porous structure.

The increase in charging rate up to 50 A/g resulted in the decrease of the mass specific capacitance to 170 F/g. This might be related to the pronounced dependence of the penetration depth on the rate of potential modulation in the case of micropores. The effect of porosity was clearly detected by the impedance measurements. The EIS spectra of the activated carbon electrode, freshly prepared as well as after 10⁴ cycles are shown in Fig. 2.9(D). The freshly prepared activated carbon

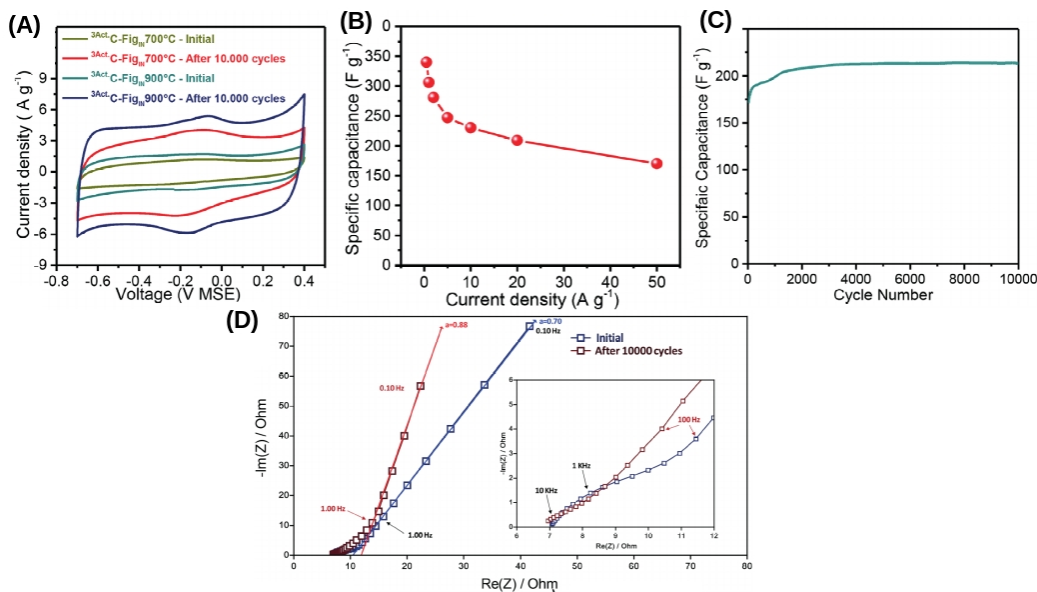


Figure 2.9: The electrochemical properties of the bio-sourced activated carbon in 0.5 M H₂SO₄. (A) CV curves measured at 20 mV/s. (B) The dependence of the mass specific capacitance on the charging rate. (C) The evolution of the mass specific capacitance with the galvanostatic cycling at 2 A/g charging rate. (D) The impedance spectra measured at open circuit voltage at 5 mV amplitude [11].

demonstrated a change in phase angle at the frequency decrease. A constant phase angle behavior, corresponding to $a=0.70$, was reached at $f < 100$ Hz.

After 10000 charging cycles, the impedance behavior was changed. The effect of the dependence of the modulation penetration depth on the frequency was detected at high frequency ($f > 1$ kHz) only. The CPE behavior with $a=0.88$ was observed at the intermediate and low frequencies. The value of a close to 0.9 corresponds to a non-homogeneous flat carbon surface. This indicates that the AC electrodes behave as flat carbon electrodes at these frequencies. 10000 charging cycles also resulted in a significant increase in the capacitance (Fig. 2.9(C)), which can be explained by an increase in the accessible surface area.

These phenomena can be interpreted as changes in the pore structure and the surface chemistry during the charge/discharge cycles, which result in the improvement of pore accessibility for an electrolyte. One may suggest that charging cycles result in the formation of more polar carbon surface groups, making the interface more hydrophilic, and, thus, making the pores more accessible. The presence of the polar surface groups also increases the interaction of electrolyte species with

the carbon surface and results in the faster surface redox transitions.

It can be seen that the impedance spectroscopy can provide valuable insights into the influence of porous structure of a material on its electrochemical properties. In order to better understand these effects, a model of the interfacial impedance for porous electrode materials in supercapacitors is needed. Such generalized staircase model and the results of its application for porous electrode systems are described in the Section 1.3.

2.5 Conclusions

The carbon materials are among the materials most commonly used for the electrodes of supercapacitors. The reasons are their high conductivity, electrochemical stability, abundance and non-toxicity. The main mechanism of charge storage in carbon electrodes is the formation of the EDL. However, the specific capacitance of the carbon electrodes in the EDLC is limited by relatively low surface specific capacitance of the carbon/electrolyte interface, which spans from $13.5 \mu\text{F}/\text{cm}^2$ for a single graphene sheet to $5 \mu\text{F}/\text{cm}^2$ for the stacked sheets of the graphitized carbon [28]. A highest theoretical SSA of the exfoliated separate graphene sheets is equal to $2680 \text{ m}^2/\text{g}$, even though the SSA above $3000 \text{ m}^2/\text{g}$ was reported for the activated carbons [62]. Thus, the highest specific capacitance of the purely EDL electrodes cannot be higher than ca. $360 \text{ F}/\text{g}$.

The porosity of the carbon is an important factor determining its total charge capacitance. The micropores with $d < 1 \text{ nm}$ provide a high SSA even for relatively compact materials. Thus, these materials have high mass and volume specific capacitances C_g and C_V . Branching of wider pores into the narrower ones also leads to the high utilization of pores surface area and the high capacitance of electrode materials. Indeed, the AC electrodes, prepared from a fig fruit, demonstrated the open and well developed porous structure, the high SSA ($2337 \text{ m}^2/\text{g}$), the high mass specific capacitance (above $300 \text{ F}/\text{g}$) and the high retention above 100% after 10000 charging cycles at $2 \text{ A}/\text{g}$.

The contribution of pseudocapacitance to the charge capacitance of a carbon electrode is relatively small. The oxidation of carbon surface results in the generation of oxygen-containing functional groups responsible for the surface-bounded pseudocapacitance reaction [29], providing ca. $10 \mu\text{F}/\text{cm}^2$. This contribution is comparable to the EDL surface specific capacitance.

The electrolyte ions intercalation into the carbon allows to significantly increase its charge capacitance. For example, the highest reported specific capacitance of the CH900-200 carbon (1194 F/g) is related to the intercalation of H^+ into the strongly swelled carbon structure [38]. However, the process of the H^+ intercalation is claimed to be very slow: the apparent diffusion coefficient of H^+ , which is intercalated from an aqueous electrolyte, is several orders of magnitude smaller than diffusion coefficient of Li^+ cations intercalated from a non-aqueous electrolyte [91]. The slowness of the H^+ intercalation limits a practical interest in this swelled carbon structures.

Contrary to the CH900-200 carbon, the high specific capacitance of *StS* carbon materials, which is also related to the pseudocapacitance phenomenon, decreases only slightly at higher charging rates (up to 50 A/g). A combination of several factors is claimed to be responsible for this outstanding electrochemical behavior:

- open porous structure with the surface of carbon easily accessible for an electrolyte,
- presence of the oxidized carbon surface groups enhancing an interaction of electrolyte species with the carbon surface,
- formation of the densely packed graphitic layers with the estimated thickness of few tens of graphene sheets, providing the medium for electrolyte ion intercalation.

Doping of the carbon materials by the heteroatoms (N,B) allows to increase their charge capacitance. In particular, N-doping enhances the interaction of solvent molecules with the carbon surface and, thus, enhances the pseudocapacitance phenomenon. Simultaneous tuning of the carbon structure and the amount of doping element allows to reach a relatively high specific capacitance even at relatively fast charging rates: above 350 F/g at 10 A/g charging rate [92].

Chapter 3

Transition Metal Oxide (TMO) electrode materials

3.1 General aspects

The metal oxides are the second largest class of materials utilized in EESD, in particular, in pseudocapacitors [1]. The oxides of transition and some post-transition metals are of particular interest due to the existence of at least 2 stable oxidation states for these metals (Fig. 3.1).

As several stable oxidation states for transition metal cations exist, the reversible redox transformation of these cations occurs upon the modification of the electrode potential. This results in an additional interfacial charge storage due to the phenomenon of pseudocapacitance, as discussed in Section 1.2.3. If this reaction is accompanied by an insertion of an ion into the sub-surface interfacial area, it provides a mechanism of propagation of the redox transition reaction into the bulk of oxide material according to (3.1). This equation is the same as the equation (1.10) in Section 1.2.3). As discussed in Chapter 1.2.4, the intercalation of an electrolyte cation Ct^+ (H^+ or Na^+ , K^+ , ...) results in the pseudocapacitance, providing that the process is sufficiently fast to be quasi-reversible in the electrochemical sense [8]:



The efficiency of the charge storage by the intercalation mechanism depends on the maximal amount of cations that can be intercalated into the crystal cell of the

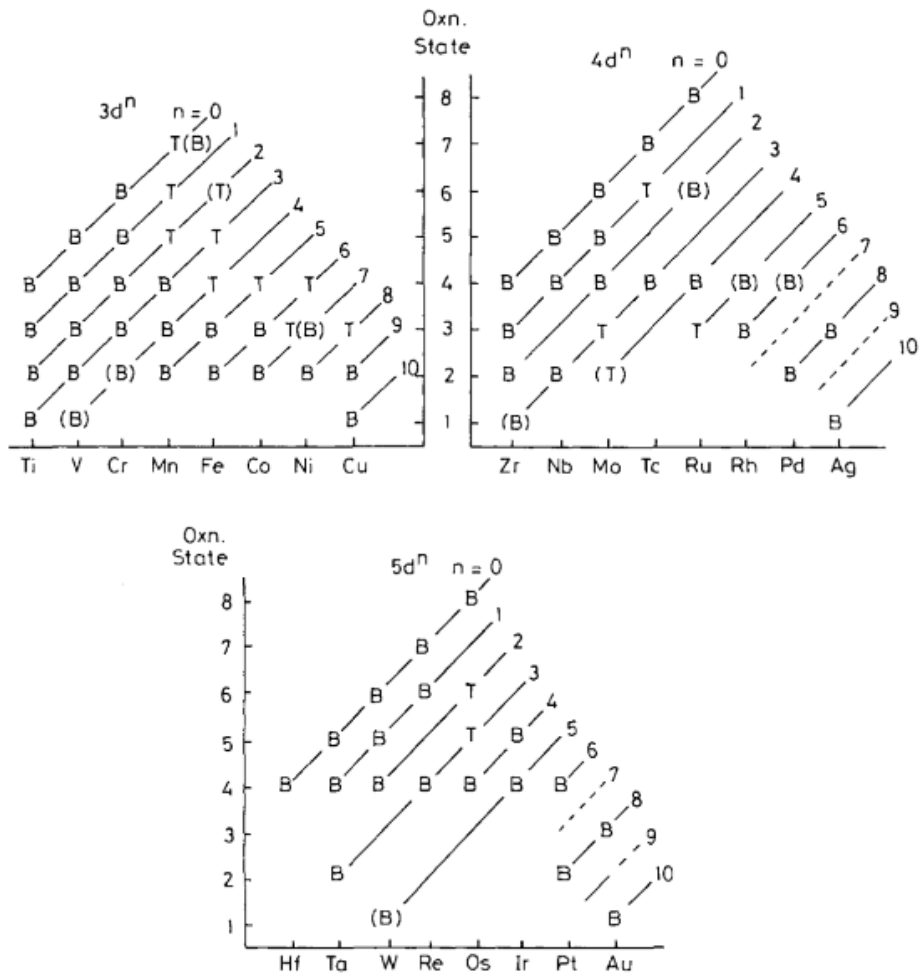


Figure 3.1: The oxidation states and the electron configurations in the TMO of the 4th ($3d$), 5th ($4d$), and 6th ($5d$) periods. **B** indicates a well-characterized binary oxide, **T** – a ternary or a more complex oxide. (B) and (T) indicate doubtful or poorly characterized or mixed valence systems [93].

TMO. Ideally, all transition metal cations of the oxide (including the bulk of the oxide phase) can undergo the redox transition, meaning that $\delta = 1$ in (3.1). In this case, the maximal theoretical specific charge storage Q_C (in C/g) for a given oxide can be estimated by using Faraday's law:

$$Q_C = \frac{x \cdot F}{M}, \quad (3.2)$$

where x is the stoichiometric factor of the metal in the oxide formula M_xO_y , M is the molecular weight of metal oxide (in g/mol).

In the literature on the batteries, the value of charge storage capacitance Q_C is traditionally given in A.h/kg (or mA.h/g) units. On the other hand, in the literature on the supercapacitors, the specific capacitance C_g is the most common characteristic of charge storage capacitance (along with the energy density, see Section 1) and traditionally given in F/g units. C_g can be related to Q_C by the simple relation:

$$C_g = \frac{Q_C}{\Delta V}, \quad (3.3)$$

where ΔV is the operational voltage of the supercapacitor, providing that Q_C is expressed in C/g. Thus, Q_C is expressed in C/g units further in the text. The transformation between the units is straightforward: C/g = 3.6 A.h/kg.

For RuO_2 ($M = 133$ g/mol, $x = 1$), $Q_C = 725.4$ C/g according to (3.2). This value is in a good agreement with the values of $Q_C = 614$ C/g, measured experimentally for the amorphous RuO_2 [44]. This agreement indicates that the value of the redox transformation degree $\delta \approx 0.85$. Thus, the most of Ru cations in the bulk of the oxide is involved into the charge storage due to a relatively high conductivity (both electronic and ionic) of RuO_2 .

The (3.2) demonstrates that the highest mass-specific charge storage is expected for the oxides of the light metals with low M . This is why the oxides of the transition metals of the 4th period (Ti, V, Cr, Mn, Fe, Co, Ni) attract more interest, while the oxides of the transition metals of the 5th (Zr, Nb, Mo) and 6th (Hf, Ta, W) periods are much less studied in relation to the supercapacitors. According to Fig.3.1, the oxides of 4th period also have a stronger variability of stable phases with different oxidation states, which is beneficial for pseudocapacitance. However, these factors cannot be generalized: a good example is RuO_2 , which is a metal oxide belonging to the 5th period. Despite having a relatively

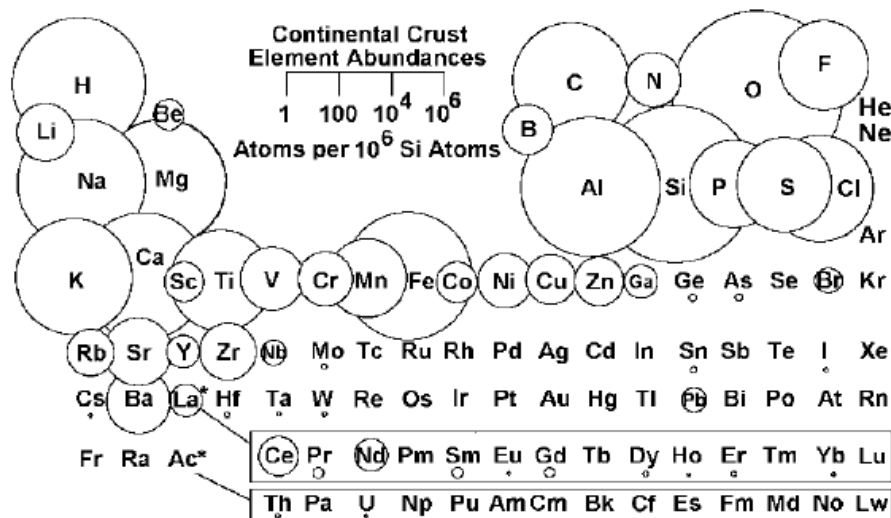


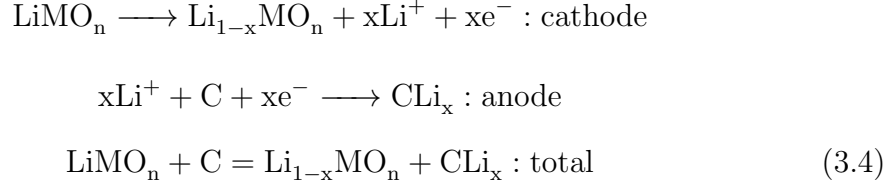
Figure 3.2: The diagram of the abundance of elements in the continental crust [94].

high molecular weight, typical for the 5th period metals, RuO_2 possesses a high electronic and ionic conductivity. This is why RuO_2 is the most studied oxide for supercapacitors.

High capacity of the ion intercalation (a large δ) and a high conductivity are important criteria of the efficiency of metal oxides in supercapacitors. From the sustainable development point of view, the other important criteria of the efficiency of electrode materials for supercapacitors, are their abundance, affordable price, non-toxicity and environmental compatibility. Fig.3.2 illustrates the relative abundance of the elements in the continental crust of the Earth [94]. The transition metals of 4th period are apparently more abundant than the heavier metals. The Fe and Ti are the most abundant among the metals of the 4th period. A non-uniform distribution of the metals all over the world has to be taken into account as well. Co, for example, is a relatively abundant element, but more than 50% of Co is located in the mines of the Democratic Republic of Congo. Such non-uniform distribution is critical for the sustainable development of the technologies relying on Co.

The crystalline structure of many binary TMO consists of MO_6 octahedra arranged in a regular way by sharing corners, sides, or faces. It creates the crystal sites and channels for the cations transport and the intercalation without losing a

structural integrity of the oxide crystal structure. This phenomenon is utilized, for example, in the Li-ion batteries, where the cathode (for example, a lithium-metal mixed oxide) is emitting Li^+ cations and the anode (for example, the carbon) is hosting them by the intercalation mechanism during the charging [95, 45, 96]:



As it has been discussed in Section 1.2.4, the reaction (3.1) has to occur under a quasi-reversible conditions in supercapacitors. It means that the equilibrium concentration of the intercalated cation Ct^+ in the oxide at the interface, as defined by the Frumkin isotherm, must be attained. This concentration depends on the interfacial potential and the concentration of Ct^+ in an electrolyte, and is not influenced by the distribution of cations in the bulk of oxide (see 1.12). In the other words, the conditions of the cation transport in the oxide phase must not influence the intercalation ratio δ , requiring a high ionic conductivity of the TMO and a relatively short diffusion path of cations. Thus, the pseudocapacitive electrode materials are often prepared as thin oxide films on a conductive substrate or as the composite materials of the nanostructured oxides (nanoparticles, nanofibers) mixed with a conductive component.

In [95], the criteria of an ideal electrode material for the Li-ion batteries were formulated. These criteria can be adapted for the electrode materials for supercapacitors, taking into account similarities and differences in the performances of batteries and supercapacitors.

- *Capacitance.* The oxide electrode materials (MO_n) should be light and able to intercalate a significant amount of the electrolyte cation Ct^+ in order to have a high specific charge capacitance.
- *Electrochemical stability.* The MO_n should be stable in a wide potential range, insoluble and inert toward an electrolyte in order to provide a high voltage available for the supercapacitor. The high voltage V and the capacitance C_g provide a high energy density (1.3).
- *Conductivity.* The electrode materials should have a high electronic conduc-

tivity. The oxide MO_n should also have a high ionic conductivity for the fast and efficient cation intercalation. A fast charge transfer within the electrode material is crucial for a high power density of supercapacitors.

- *Structural integrity.* The MO_n oxide should demonstrate none or minimal modification of its crystalline structure for a possible widest range of the intercalation efficiency δ ($0 < \delta < 1$) for a high cyclability retention.
- *Availability.* From the scaling up point of view, the electrode materials should be abundant, inexpensive and non-toxic.

The capacitance and the availability criteria were discussed above. The conductivity, the electrochemical stability and the structural integrity of the TMO are discussed below.

3.2 Conductivity of TMO

The sufficient electronic conductivity is necessary to ensure the uniform distribution of the potential over the electrode material deposited on the current collector. In contrast to the carbon materials, used in the EDLC electrodes, most of the metal oxides are either semiconductors or insulators with a low conductivity at the ambient conditions ($10^{-3} - 10^{-17} \text{ S} \cdot \text{cm}^{-1}$). The conductivity increases exponentially with the increase of the temperature [97].

However, there exist the oxides which have metallic conductivity, which decreases with the temperature increase ($10^2 - 10^6 \text{ S} \cdot \text{cm}^{-1}$): TiO , CrO_2 , NbO , RuO_2 , ReO_3 . There is also a numerous class of the metal oxides, which have a low conductivity at low temperatures, but demonstrate the transition to the metal conductivity at the certain temperature: Ti_2O_3 , Ti_3O_5 , Fe_2O_4 , NbO_2 , several vanadium oxides.

The electronic conductivity of the oxide material depends on its properties, and it is difficult to find general correlations between various parameters. The influence of various parameters of the oxide chemical and crystalline structures on its conductivity is discussed below.

The intrinsic electronic conductivity of the metal oxides depends on the position of the d -electron band relative to the Fermi level and the shape of the d -band. The conductivity depends on the d -band width: the narrowing of the band due to a

larger lattice distance results in a lower conductivity [97]). The conductivity is also influenced by the hybridization of the d -band with s - and p -orbitals: a stronger hybridization results in a lower conductivity [98]. These dependencies can be explained by the band theory combined with the Mott concepts of the dependence of band narrowing on the lattice parameters, the band overlap model and the antiferromagnetism effects.

The combined theory correctly predicts that the oxides M_2O_3 with 1,3,5,7 and 9 d -electrons (the corundum crystalline structure) are the insulators ($Ti_2O_3-3d^1$, $Cr_2O_3-3d^3$, $Fe_2O_3-3d^5$, and $Ni_2O_3-3d^7$), and $V_2O_3-3d^2$ has the metallic conductivity [97]. The monoxides TiO , VO , MnO , FeO , CoO , NiO have the same crystalline structure (monoclinic $NaCl$), but the systematically varying lattice constant: from 4.09 Å for VO to 4.43 Å for MnO . In this set of oxides, TiO has the metallic conductivity, VO has the transition from the semiconducting behavior at low temperature to the metallic conductivity above 126 K, and the other oxides are the insulators [98].

The electronic conductivity of a material depends on its crystallinity. In general, a polycrystalline material has a lower conductivity than single-crystals due to the grain boundaries resistance [97]. It can also be expected that amorphous materials have a lower conductivity than the crystalline oxides due to a higher concentration of the grain boundaries. However, this is not always the case: the crystalline V_2O_5 is an insulator, while the amorphous V_2O_5 is a semi-conductor with conductivity $\sigma = 6.5 \cdot 10^{-6} \text{ S.cm}^{-1}$ (as explained by the small polaron nearest-neighbor hopping model [99]).

The electronic band structure and, thus, the conductivity of the oxide materials, can be tuned by altering its stoichiometry, for example, by the creation of oxygen deficiencies or the controlled doping [100]. One of the most impressive examples is the formation of Magnéli phases. Magnéli phases are the stable oxygen-deficient phases, which are formed by inducing regular stacking faults into the rutile-type oxides MO_2 . These phases have a general formula M_nO_{2n-1} [101]. Fig.3.3 demonstrates how the intrinsic conductivity of the titania oxides changes with its stoichiometry: TiO_2 anathase is a typical semiconductor, while Ti_4O_7 has the conductivity $1.5 \cdot 10^3 \text{ S.cm}^{-1}$, which is comparable to the graphite.

The doping of the oxide materials by the cation insertion is another commonly used approach to increase the conductivity [100]. For example, the doping of the electrochemically deposited MnO_2 by Au up to 9.9 at.% results in inducing the

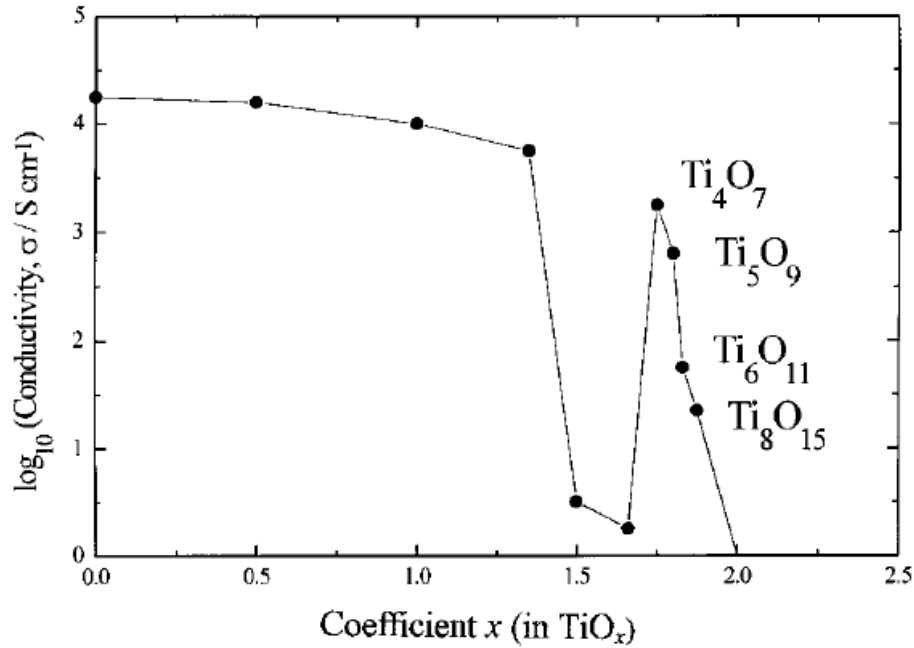


Figure 3.3: The dependence of the intrinsic electronic conductivity of Magnéli oxide $\text{Ti}_n\text{O}_{2n-1}$ on its stoichiometry [101].

intermediate electronic states close to the conductance band and the conductivity increase [102]. This results in the increase of C_g of the 9.9 at.% Au doped MnO_2 to 626 F/g comparing to 380 F/g for the non-doped MnO_2 . The further increase in the Au doping level results in the segregation of Au into the nanoparticles under the potential cycling and in the decrease in specific capacitance. The cycling of the potential of the optimally doped Au– MnO_2 oxide results in the capacitance increase due to more homogeneous redistribution of Au in the oxide. This observation highlights an importance of controlled and uniform distribution of a dopant in the oxide for the efficient improvement of the electrochemical performance.

The conductivity of the oxides with the same stoichiometry may significantly vary depending on its crystalline phase. For example, MnO_2 can be synthesized with various crystallographic structures: α - MnO_2 , β - MnO_2 , γ - MnO_2 , δ - MnO_2 , ramsdellite, delithiated spinel λ - MnO_2 , todorokite MnO_2 [95] (see Table 3.1). The difference in the structure is related to the way of arranging of MnO_6 octahedra into a regular structure and the formation of molecular tunnels. The conductivity of these oxides (mixed with 20%_{wt.} of carbon) was found to vary from 10^{-6} for

Phase	Crystallographic structure	Relative tunnel size	Comments
α -MnO ₂	cryptomelane	(2x2) + (1x1)	regular combination of 2x2 (4.6x4.6 Å) and 1x1 (1.9x1.9 Å) tunnels; stabilized by cations or water
β -MnO ₂	pyrolusite	(1x1)	compactly arranged MnO ₆ octahedra with (1.9x1.9) Å tunnels
γ -MnO ₂		(2x1) + (1x1)	combination of ramsdellite 2x1 (1.9x2.3 Å) and β -MnO ₂ structure; ratio depends on synthesis conditions
δ -MnO ₂	birnessite		layers of β -MnO ₂ with 7.0 Å interlayer distance
λ -MnO ₂	spinel		formed by delithiation of LiMn ₂ O ₄ spinel; narrow tunnels
	ramsdellite	2x1	regular arrangement with (2x1) tunnels; γ -MnO ₂ with nearly no β -MnO ₂

Table 3.1: The description of some of the crystalline phases of MnO₂ [95, 103]

the pyrolusite (β -MnO₂) to $2.8 \cdot 10^{-3}$ S.cm⁻¹ for the spinel (λ -MnO₂) or $3 \cdot 10^{-3}$ S.cm⁻¹ for the cryptomelane (α -MnO₂) [103]. It is important to note that various phases may contain various amounts of water. For example, β -MnO₂ contains no water after the synthesis, while α -MnO₂ contains significant amount of water. The water in α -MnO₂ stabilizes the wide tunnels structure and can enhance the charge transfer rate [95]. The difference in the electrochemical performance of various phases of MnO₂ will be discussed below.

The sufficient intrinsic electronic conductivity (i.e. the low resistivity) is necessary for the electrode materials for supercapacitors due to the requirement of a high specific power (see 1.4). However, even for MnO₂ with a relatively high conductivity, this requirement is fulfilled only for the thin film electrodes, where the values of pseudocapacitance are close to the theoretical value [104, 105]. The

increase of electrode loading above ca. $10 \mu\text{g}/\text{cm}^2$ results in the significant decrease of the specific capacitance. This is related to the hindered charge transfer at interparticles contacts, which have much lower effective cross-sections comparing to the bulk volume of the particles. A typical loading of carbon electrodes in the commercial supercapacitors is, however, $1\text{-}10 \text{ mg}/\text{cm}^2$, i.e. 2-3 orders of magnitude larger than the above mentioned limit.

This problem is typically addressed by adding a conductive carbon powder (15-20%*wt.* of C) to the oxide in order to form a thicker electrode. However, the mechanical mixing of the components often results in the non-uniform distribution of the oxide particles and the existence of interparticles contacts even at the carbon content as high as 66%*wt.* [13]. A more promising approach is the synthesis allowing the formation of the metal oxide and the carbon composites with the uniform mixing of the components directly during its formation. The example is the solid state combustion (SSC) synthesis, which is discussed in details in Section 3.3.3. The 34%*wt.* $\text{Mn}_3\text{O}_4/\text{C}$ composite, prepared by the SSC method, was studied by the author [13]. The material demonstrated the capacitance which was several times higher comparing to the mechanical mixture of the same components. The difference in capacitance values became stronger at the faster potential sweep rate, i.e. at the higher power of charging/discharging (Fig.3.4).

As discussed above, the sufficient electronic conductivity is necessary for the uniform polarisation of the electrode material and its efficient utilisation in supercapacitors. The ionic conductivity is another factor, which is often claimed to limit material utilization in supercapacitors. For example, a study of different crystalline phases of MnO_2 [103] demonstrated that their specific capacitance was correlated with SSA and, more strongly, with the ionic conductivity. In particular, very close specific capacitances of the spinel and the birnessite $\delta - \text{MnO}_2$ were detected despite the fact that the electronic conductivity of the spinel was 3 orders higher. The corresponding ionic conductivities were much closer (0.015 and $0.017 \text{ S}\cdot\text{cm}^{-1}$), allowing the authors of [103] to conclude that the ionic conductivity was a main factor influencing the specific capacitance of the oxide materials.

One has to emphasize that measuring the ionic conductivity of the TMO under the ambient conditions is more difficult than measuring the electronic conductivity. In particular, separating ionic and electronic conductivities of the TMO is not simple. The ionic conductivity is often measured as the difference of total conductivity of the material filled with an electrolyte and the conductivity of the

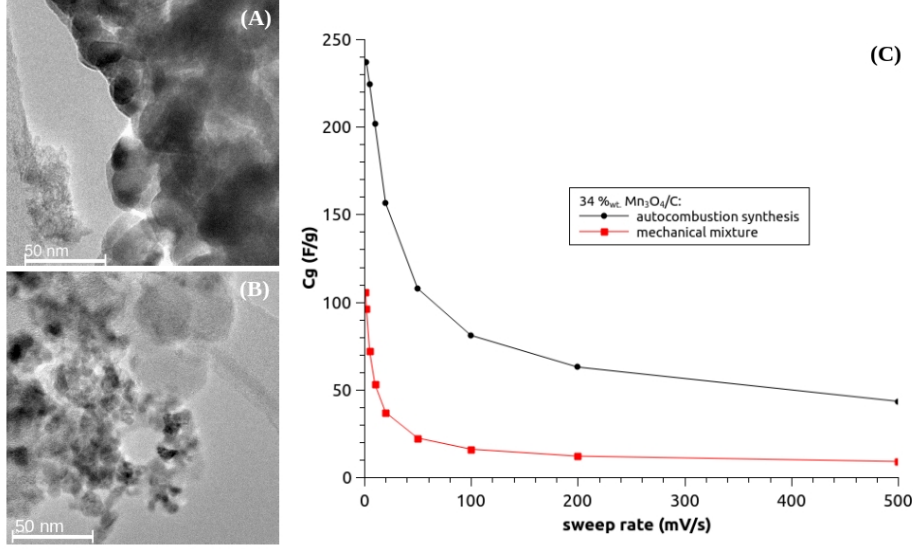


Figure 3.4: The TEM images of Mn_3O_4 synthesized by the SSC method (A) without carbon, (B) with 66% $_{wt.}$ of carbon. (C) The dependence of specific capacitance C_g on the potential sweep rate for the 34% $\text{Mn}_3\text{O}_4/\text{C}$ electrode [13].

dry material (which is assumed to have the electronic conductivity only) [103]. However, in this method the conductivity of an electrolyte in the interparticles volume is either neglected or approximated by a simple geometric volume. Thus, one may anticipate a relatively strong uncertainty in the reported values of the ionic conductivities.

Thus, it is important to evaluate the theoretical requirements to the ionic conductivity for the TMO materials for supercapacitors. As mentioned in Section 1.2.4, the ionic transport in the bulk of the oxide phase should not influence the interfacial equilibrium concentration of intercalating ions. The intercalation follows the interfacial redox reaction 3.1, resulting in the gradient of Ct^+ concentration from the interface to the bulk of the oxide particle. Assuming the uniform distribution of the electrical potential within the oxide phase (due to sufficient electronic conductivity), the charging current I is related to the flow J_{Ct^+} of Ct^+ ions from the interface to the bulk of oxide according to the first Fick's law ¹:

$$I = -FAJ_{\text{Ct}^+} = -FAD_{\text{Ct}^+} \frac{\partial C_x}{\partial x}, \quad (3.5)$$

¹For the simplicity of evaluation, the flat diffusion model is used, neglecting the curvature of the electrode/electrolyte interface

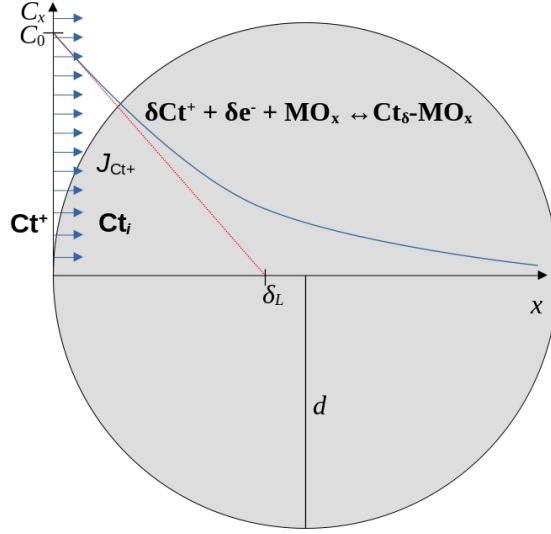


Figure 3.5: The illustration of the Ct^+ cation intercalation into the oxide particle.

where A is the surface area of the electrode/electrolyte interface, C_x is the concentration of Ct^+ inside the oxide phase at distance x from the interface (Fig.3.5).

Using the second Fick's law and the boundary conditions $C_{x=0} = C_0$, $C_{x=\infty} = 0$, the equation (3.5) can be integrated into the following equation for the charging current:

$$I = AFC_0 \frac{D_{\text{Ct}^+}}{\delta_L}, \quad (3.6)$$

where δ_L is the apparent thickness of concentration gradient layer.

For the supercapacitors materials, the requirement for the concentration of Ct^+ is $C_x \approx C_0$ for any x inside the particle. This means that $\delta_L \gg d$, where d is the thickness of the oxide phase. For example, d can be the diameter of the oxide particle.

For the efficient intercalation material, $\delta \approx 1$, and the value of C_0 can be approximated as the concentration of metal cations of the oxide. For example, for MnO_2 , $C_0 \approx \rho/M$, where ρ is the density of the oxide material, and M is its molecular weight. Thus, for MnO_2 $C_0 \approx 0.058 \text{ mol/cm}^3$.

The value of δ_L depends on the charging rate I (the faster the charging, the shorter is δ_L) and on the solid state diffusion coefficient D_{Ct^+} (the bigger D_{Ct^+} , the longer is δ_L). The diffusion coefficient can be related to ionic conductivity σ_i

by using the Smolukhowski-Einstein equation:

$$\sigma_i = \frac{F^2 C_{\text{Ct}^+} D_{\text{Ct}^+}}{RT}. \quad (3.7)$$

For $\sigma_i \approx 0.02 \text{ Ohm}^{-1}\text{cm}^{-1}$ reported in [103], $D_{\text{Ct}^+} \approx 10^{-7} \text{ cm}^2/\text{s}$. From the practical point of view, it is useful to relate the charging rate I (in A) with the specific charging current density i_m (in A/g) by considering the geometry of a spherical particle with the diameter d :

$$i_m = \frac{6IA}{\rho d}. \quad (3.8)$$

Combining the equations (3.7) and (3.8), the equation for δ_L dependence on i_m is obtained:

$$\delta_L = \frac{6FC_{\text{Ct}^+}D_{\text{Ct}^+}}{i_m\rho d}. \quad (3.9)$$

For $i_m = 100 \text{ A/g}$ (the fast charging rate for the supercapacitor electrodes) and $d = 100 \text{ nm}$ (large particles), (3.9) gives the estimate $\delta_L \approx 0.6 \text{ cm}$, which apparently satisfies the condition $\delta_L \gg d$. The values of D_{Ct^+} estimated from the values of σ_i reported in [103] are few orders of magnitude higher than those reported for the Li^+ solid state diffusion [39]. This fact points to the above mentioned uncertainty of the measurements of σ_i for the TMO materials. However, even for the values of D_{Ct^+} , which are 3 orders of magnitude lower, the estimated value of δ_L is $6 \mu\text{m}$ and, thus, the condition $\delta_L \gg d$ still holds.

The above discussion leads to the assumption that for the nanostructured oxides (for example, in the form of large nanoparticles) the ion mass transport is not a limiting factor even for relatively high charging rates. However, this requires that the electronic conductivity of the oxide phase is sufficiently high to assume the uniform distribution of the potential inside the oxide phase.

The electrochemical stability of the TMO as another important criterion of efficiency of the oxide materials as supercapacitor electrodes is considered in the next section.

3.3 Electrochemical stability and structural integrity of TMO

The other important parameter determining the performance of electrode materials in supercapacitors is the capacitance retention during charge/discharge cycling. The pseudocapacitance phenomena involves the redox reaction which can be not completely reversible due to the change of the metal oxide structure or the formation of an insulating or soluble oxide phase. In the electrochemistry, the thermodynamic stability of a material in aqueous solutions is conveniently analyzed by the $E - pH$ diagrams, which are thoroughly presented in Pourbaix atlas [106] for the most of the metals. The Pourbaix diagrams for some of the metal / metal oxide systems are presented in Fig.3.6. Generally, there are 3 domains of stability of metal / metal oxide system in contact with an electrolyte.

- *Immunity (blue domains in Fig.3.6).* Under these conditions, a metal in contact with an electrolyte is thermodynamically stable and not corroding. The charge can be accumulated on the metal/electrode interface, similar to the EDLC. The charge storage in the bulk of the metal is possible by the absorption of electrolyte components, for example, by the absorption of hydrogen in Pd and the formation of Pd hydrides [107]. However, this type of processes provides either lower energy density or weaker cyclability comparing to the pseudocapacitance in the metal oxides.
- *Corrosion (yellow domains in Fig.3.6).* The thermodynamically stable form of the metal under these conditions is water soluble: it can be either the metal cation M^{z+} (in general, at acidic pH) or the metal anion MO_y^{z-} or $H_xMO_y^{z-}$ (in alkaline solutions). The diagram does not show the kinetics of the corrosion, thus, the corrosion might be kinetically hindered. For example, the chromium (III) oxide Cr_2O_3 is thermodynamically unstable at acidic pH (Fig.3.6(C)). However, the kinetics of its dissolution in the most of acids is so slow that the layers of Cr_2O_3 are used as the corrosion protection [108]. Similarly, Al oxide Al_2O_3 is stable in the acids due to the kinetically hindered dissolution despite being thermodynamically unstable. Nevertheless, in general, the lack of thermodynamic stability in the corrosion domains does not allow the sufficient cyclability of a metal oxide for the application in supercapacitors.
- *Passivation (green domain in Fig.3.6).* Under these conditions, the given

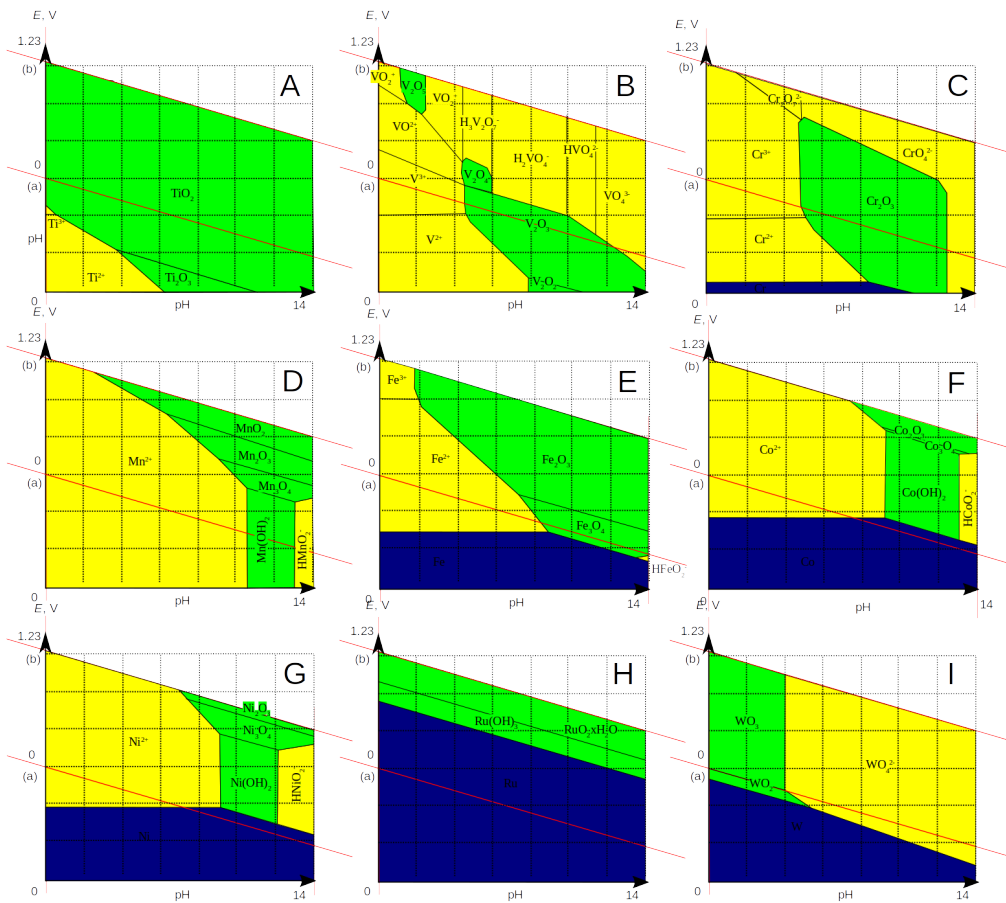


Figure 3.6: The Pourbaix diagrams for different metals (the sketch is adapted from [106]).

metal oxide or hydroxide phase is thermodynamically stable in contact with an aqueous electrolyte. If the pure metal is in contact with an electrolyte, then it corrodes with the formation of the deposit of oxide/hydroxide film, which slows down or stops the corrosion. This means that the metal is *passivated*. The composition of the passive film depends on the conditions of its formation. For the same metal, various Pourbaix diagrams can be plotted for various passive films. For the purpose of the current work, Fig.3.6 shows the most thermodynamically stable oxide phases at the ambient conditions. On the other hand, the metal oxide films formed under the electrochemical control are often amorphous, hydrated, or even non-stoichiometric [108]. The borders of the passivation domains depend on the solubility of the given phase. In Fig 3.6 these borders are plotted for 10^{-6} M concentration of the soluble form.

The supercapacitors with an aqueous electrolyte operate in the potential range between lines (a) and (b) on the Pourbaix diagrams. The lines (a) and (b) show the pH-dependent potential of the water electroreduction to H_2 and the electrooxidation to O_2 correspondingly: this is the potential range of water stability. As one can see from Fig.3.6, the diagrams for different metals differ significantly. Below some types of the electrochemical behavior of the selected TMO are considered in details.

3.3.1 TMO stable in wide pH range: RuO_2 , TiO_2

Relatively few transition metals are stable in a wide range of pH: for example TiO_2 (Fig.3.6 A), RuO_2 (Fig3.6 H). In particular, **RuO_2** is the most extensively studied TMO as supercapacitor electrode material. Several comprehensive reviews on the applications of the RuO_2 -based electrodes in supercapacitors are available [109], including a recent work [110]. Besides its chemical and electrochemical stability (Fig.3.6(H)), RuO_2 has a high electrical conductivity $\sigma = 2.8 \cdot 10^4$ S.cm⁻¹ [111], resulting from the position of the Fermi level within the DOS of the $2d$ band [112]. Due to the high electronic conductivity, the RuO_2 electrodes can be easily obtained by the cathodic deposition with the fine control on the conditions and amount of deposited material [113, 114, 115].

Assuming 1e- charge storage per Ru atom, the maximal charge storage Q_C for RuO_2 , according to (3.2), is $Q_C = 721.8$ C/g which translates into the specific capacitance $C_g \approx 800$ F/g for the potential interval of 0.9V. Indeed, the values

of C_g above 700 F/g are routinely obtained for RuO_2 , indicating the high values of the intercalation parameter $\delta \approx 1$ in (1.8). This provides the ultimately high efficiency of charge storage in RuO_2 in acids due to the H^+ insertion. High values of the specific capacitance and the insertion parameters are detected even for relatively thick deposits of the RuO_2 oxide, up to 1.4 mg/cm² without the addition of a conductive component [110]. The RuO_2 /carbon composites can be prepared by the cathodic electrodeposition of the oxide on the carbon substrates with desired morphology. The optimization of structure and composition of these electrode materials provides high specific capacitance values $C_g = 1176$ F/g for ca. 1 mg/cm² loading of the 12%_{wt.} RuO_2 /CNT composite [114]. The high electrochemical stability of RuO_2 allows applying a wide potential window up to 1V both in acid [113] and alkaline [116] electrolytes.

One may conclude that RuO_2 demonstrates optimal electrochemical properties for the supercapacitor applications. However, RuO_2 wide commercialization in the industrial supercapacitors is hurdled due to its high price and toxicity.

TiO₂ is a wide-gap semiconductor (the band gap $E_g=3.2$ eV for anathase) with a relatively low electronic ($5.5 \cdot 10^{-6}$ S · cm⁻¹ [117]) and ionic conductivities, which limits its application in supercapacitors. The annealing in a reductive atmosphere (in vacuum or H₂) creates the oxygen vacancies which results in higher electronic conductivity. When a sufficient amount of regular oxygen vacancies is accumulated, the Magnéli phases of $\text{Ti}_n\text{O}_{2n-1}$ are formed having the conductivity of Ti_4O_7 , $\sigma = 1.5 \cdot 10^3$ S · cm⁻¹, comparable to the graphite [101] (Fig.3.3). However, according to the Pourbaix diagram (Fig.3.6A) the reduced states of Ti^{3+} and Ti^{2+} are unstable in aqueous solutions and are oxidized to Ti^{4+} , which leads to the conductivity loss. Due to the semiconducting nature of the bulk TiO_2 , the interfacial capacitance is predominant by the charge depletion layer within the oxide. Therefore, the capacitance of TiO_2 is smaller than the interfacial capacitance of well-conducting materials [118]. Thus, the bulk or powdered TiO_2 are not considered as suitable electrode material for supercapacitors.

On the other hand, the development of 2D-nanostructured TiO_2 phases is an interesting and well explored approach towards the tuning of the properties of titania. The nanotubes of titania can be routinely prepared by the hydrothermal synthesis [117] or by the anodization of the Ti electrode [119, 120]. Both approaches provide the control of the geometry of nanotubes, namely, their length (up to few μm), wall thickness (from few to few tens of nm) and inner diameter

(ten or tens of nm) can be controlled. The composition of the nanotubes can also be varied by changing the composition of synthesis media or by post-treatment [121]. The advantages of the TiO₂-nanotubes in comparison to the conventional nanopowders are (i) a lower contact electrical resistance and (ii) a shorter electron and/or ion diffusion path. Due to these advantages, the TiO₂-nanotubes are widely studied as electrode materials in electrocatalysis, especially in the oxygen electroreduction and the oxygen evolution reactions due to the high corrosion resistance of TiO₂) [122]. The TiO₂-nanotubes are often used in the photoelectrocatalysis, in particular, in the water splitting reaction [121, 123]. Moreover, the impedance spectroscopy analysis of the arrays of vertically aligned TiO₂-nanotubes demonstrated a significant increase in the charge carriers density in comparison to the bulk TiO₂, resulting in much higher interfacial capacitance [124]. It was concluded that the interfacial capacitance of the arrays of nanotubes, in contrast to the bulk TiO₂, is predominant by the EDL capacitance and the pseudocapacitance related to the proton insertion [125, 126]:



More impressive results were obtained for the layered titanates, prepared by the hydrothermal synthesis. Here the sheets of anatase TiO₂ were separated by the interlayer space, which was stabilized by the insertion of proton or alkaline cations. The specific capacitances above 300 F/g were reported for the hydrated H₂TiO₃ [127] and the sodium layered titanates Na₂Ti₂O₄(OH)₂ [128]. This was attributed to the reversible insertion of the electrolyte cations. One may conclude that despite a low electronic and ionic conductivities of the bulk TiO₂, the development of the 2D-nanostructured layered titanate materials is a promising approach to the development of new efficient electrode materials for supercapacitors.

3.3.2 TMO stable in acidic pH: oxides of W and Mo

The most of transition metal oxides (for example, the oxides of Co, Ni, Mn) is more stable in neutral and weakly alkaline solutions, while being thermodynamically unstable in acids. The exceptions are the oxides of W (Fig.3.6 I) and Mo, which are stable in acids and dissolving in alkaline solutions.

In particular, WO₃ is a wide-gap (2.6 eV) semiconductor with the n-type conductivity at the ambient temperature [129]. The maximal theoretical charge stor-

age for WO_3 , according to (3.2), is $Q_c = 451.3 \text{ C/g}$. The monoclinic WO_3 has a relatively low intrinsic conductivity: below $10^{-5} \text{ S.cm}^{-1}$, making this phase unpractical for the supercapacitor applications. However, WO_3 can be easily reduced thermally (in a reducing atmosphere) or electrochemically, thus, forming the substoichiometric oxide WO_{3-x} due to the oxygen vacancies. The intrinsic conductivity of the reduced oxide is as high as $4.8 \cdot 10^{-2} \text{ S.cm}^{-1}$ [129]. If the synthesis of the tungsten oxide is adapted to avoid the interparticles resistance, then the WO_3 -based electrodes shows a significant charge capacitance due to the H^+ insertion phenomena occurring in acids, similar to the reaction 1.8 with RuO_2 :



In order to avoid the interparticles resistance, various synthetic strategies are applied, namely, the template synthesis [130], the hydrothermal synthesis of nanorods [131], or the direct synthesis of graphene / oxide composites [132], [133].

In particular, the mesoporous substoichiometric WO_{3-x} oxide shows the capacitance equal to 199 F/g [131]. This value corresponds to the insertion factor $\delta \approx 0.4$, showing a high efficiency of the charge storage. The reaction 3.10 occurs at low potentials in the wide range below ca. 0.6V RHE . It gives the advantage of using WO_3 -based materials as negative electrodes in the assymetric supercapacitors. The operational voltage range of 1.65V was applied for the supercapacitor consisting of the WO_3 nanorods in the negative electrodes and the carbon nanofibers in the positive electrodes [132]. This device demonstrated an outstanding energy density equal to 35.3 Wh/kg at the power density $P = 314 \text{ W/kg}$.

Besides stability in acidic electrolytes, the advantage of the molybdenum oxide MoO_3 is the accessibility of a wide range of the oxidation states from $+6$ to $+2$ [134]. However, the electrical conductivity of MoO_3 at ambient conditions is low: below $10^{-8} \text{ S.cm}^{-1}$ at 300K . Thus, a high charge capacitance was observed only in the composites with low oxide loadings [134] or the thin oxide films. In the latter case, one may use the advantage of a relatively facile exfoliation of the layered orthorhombic crystalline structure of MoO_3 [135] to obtain the specific capacitance above 500 F/g . However, these high charge capacitances are observed only at slow charging rates due to the complications with a low electronic conductivity of the oxide phase.

3.3.3 TMO stable in neutral and weak alkaline pH: oxides of Mn, Fe, Co, Ni

As mentioned above, the most of transition metals have stable oxides at not very strong alkaline pH, for example, Mn, Fe, Co, Ni, (Fig. 3.6 (D)-(G)).

Oxides of Fe

Comparing to the other transition metals mentioned above, the iron oxides have the widest pH of stability (Fig. 3.6(E)). Another remarkable advantages of the iron oxide electrode materials are their relative abundance (since iron is the most abundant element among the transition metals (Fig.3.2)) and non-toxicity. The oxides of Fe are the most interesting electrode materials from the viewpoint of sustainable development. Thus, considerable efforts have been taken for the development of the iron oxide electrode materials for supercapacitors [136]. The most common iron oxides are α -Fe₂O₃ (hematite), Fe₃O₄ (magnetite), and α - and γ -FeOOH (goetite and lepidocrocite correspondingly).

α -Fe₂O₃ (hematite) is the iron oxide with the widest range of thermodynamic stability according to the Pourbaix diagram (Fig.3.6(E)). It has the rhombohedral (corundum) crystalline structure. According to (3.2), the maximal charge capacitance for this oxide ($M = 159.69$ g/mol) is $Q_c=1209$ C/g (assuming $1e^-$ per 1 Fe atom storage). However, the bulk pure α -Fe₂O₃ is an insulator. The presence of a structural defect can transform it into a semiconductor [137] with a low conductivity reported in the range $10^{-4} - 10^{-14}$ S.cm⁻¹. Thus, the hematite is used as electrode material in the form of thin films [138], yet demonstrating the specific capacitance equal to 178 F/g (in 1M NaOH in the potential window 0.7V), which is much lower than the theoretically expected value. Nevertheless, more than a 6-fold increase in the surface specific capacitance was detected for the graphite foam after it was decorated by the atomic layer deposition with the uniform layer of the Fe₂O₃ nanoparticles of the size 10 nm [139]. This electrode material demonstrated a remarkable capacitance retention more than 95% after $5 \cdot 10^4$ cycles in 1M NaOH. The assymetric supercapacitor with the Fe₂O₃/graphite // CoMoO₄/graphite electrodes demonstrated the specific capacitance equal to ca. 210 F/g (total electrode mass) or the energy density equal to 74.7 W.h/kg at $P = 1.4$ kW/kg.

As it has been mentioned, the presence of structural defects, in particular, oxygen vacancies, in α -Fe₂O₃ results in an increase of its electronic conductivity due

to the modification of its electronic states. The doping of α -Fe₂O₃ by the electron acceptor cations, in particular, Ti⁴⁺, leads to the formation of the stabilized oxygen vacancies and reduced cation Fe²⁺ sites [140]. These modifications provide a significant improvement of the charge storage performance of α -Fe₂O₃ with the capacitance retention above 90% after $3 \cdot 10^4$ cycles.

Fe₃O₄, or FeO · Fe₂O₃, is a spinel oxide of iron, formed by the high temperature reduction of Fe₂O₃. Its maximal charge storage capacitance, according to (3.2) with $x = 3$ and $M = 231.5$ g/mol, $Q_C = 1250,4$ C/g. This value is even higher than the value of Q_C for Fe₂O₃. Contrary to the hematite oxide, Fe₃O₄ has a high conductivity at the ambient conditions: $10 - 10^2$ S.cm⁻¹ [141]. Thus, Fe₃O₄ was proposed as a promising component for supercapacitors electrode material [136]. Despite a relatively high conductivity, the stand-alone films of Fe₃O₄ nanoparticles (diameter is ca. 20 nm) demonstrated a moderate specific capacitance $C_g = 118.2$ F/g and a weak capacitance retention of 89% after just 500 cycles in 1M Na₂SO₃ [142]. The moderate performance of Fe₃O₄ can be attributed to the high interparticles resistance in the absence of the conductive component of the electrode layer [143]. The other problem of utilisation of Fe₃O₄ as an electrode material is a narrow (ca. 200 mV) potential window of its thermodynamic stability, see the Pourbaix diagram (Fig.3.6(E)). At more positive potentials one can expect the oxidation of Fe^{II} sites into Fe^{III} resulting in the performance loss. The electrodes of Fe₃O₄ are often tested in the Na₂SO₃ electrolytes, because the sulfite is a reductant and helps to stabilize the Fe^{II} sites. Also, the fine dispersion of the Fe₃O₄ nanoparticles on the carbon substrates allows to avoid the interparticles resistance complications and stabilizes the performance. The high specific capacitance of the Fe₃O₄ nanoparticles with $d = 5$ nm, which are dispersed on the reduced graphene oxide sheets, is $C_g=361$ F/g at 1 A/g in 1M KOH. This high specific capacitance is stable up to 10^3 cycles at 5 A/g [144].

Case study: hierachial deposits of Fe₃O₄@graphene / PEDOT:PSS

In this subsection the hierarchial electrode material with the Fe₃O₄ nanoparticles deposited on the graphene and arranged into the layered structure is described. This material was developed in the common project between IPCMS, ICS and ICPEES with the participation of the author [12].

The uniform deposits of the Fe₃O₄ nanoparticles on the few-layer graphene

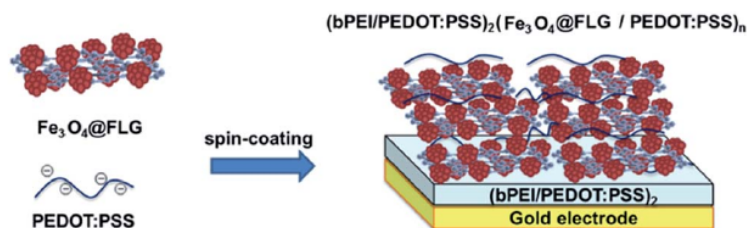


Figure 3.7: The $\text{Fe}_3\text{O}_4/\text{FLG} // \text{PEDOT:PSS}$ electrodes, prepared by the layer-by-layer deposition [12].

(FLG) support were utilized to construct thick electrode layers up to $72 \mu\text{m}$ [12]. The regular structure of the deposit was preserved by the layer-by-layer deposition of the $\text{Fe}_3\text{O}_4/\text{FLG}$ layers alternating with the PEDOT/PSS layers, which played the role of structuring element (Fig.3.7). Preserving the structure of the layer resulted in the linear increase in the surface specific capacitance with the number of deposited layers. However, after more than 20 bilayers were deposited, the slope of the increase decreased due to the partial disturbance of the structure (Fig.3.8). The mass specific capacitance had the maximal value $C_g=116 \text{ F/g}$ in $0.5 \text{ M Na}_2\text{SO}_3$ for the deposit with 15 bilayers (Fig. 3.9). The stability of the performance was demonstrated by the retention of 114% for the initial capacitance after $1.5 \cdot 10^3$ cycles at 1 A/g in $0.5\text{M Na}_2\text{SO}_3$. The increase of the capacitance was attributed to the electrochemically induced recovery of the Fe_3O_4 chemical state. The chemical state of Fe_3O_4 was assumed to be altered due to the partial oxidation during the materials and final electrode preparations [12].

The oxyhydroxide of Fe^{III} , **FeOOH**, occurs mainly in 2 allotropies: the goethite $\alpha\text{-FeOOH}$ and the lepidocrocite $\gamma\text{-FeOOH}$. These 2 oxides are formed spontaneously on the surface of iron as main components of the rust layer (together with hematite and magnetite) [145]. They can also be grown on the surface of the Fe electrode under the controlled electrochemical conditions [146]. The ratio of the components depends on the conditions of formation. The goethite is claimed to be a protective component, while the lepidocrocite – a dissolving component.

The conductivity of these oxides is low, ca. $10^{-9} \text{ S.cm}^{-1}$ [147], which strongly limits their application in supercapacitors. The oxohydroxides of Fe are used as the supercapacitors electrodes in the form of nanoparticles supported on a conductive substrate. For example, the composites of the goethite nanoparticles on rGO

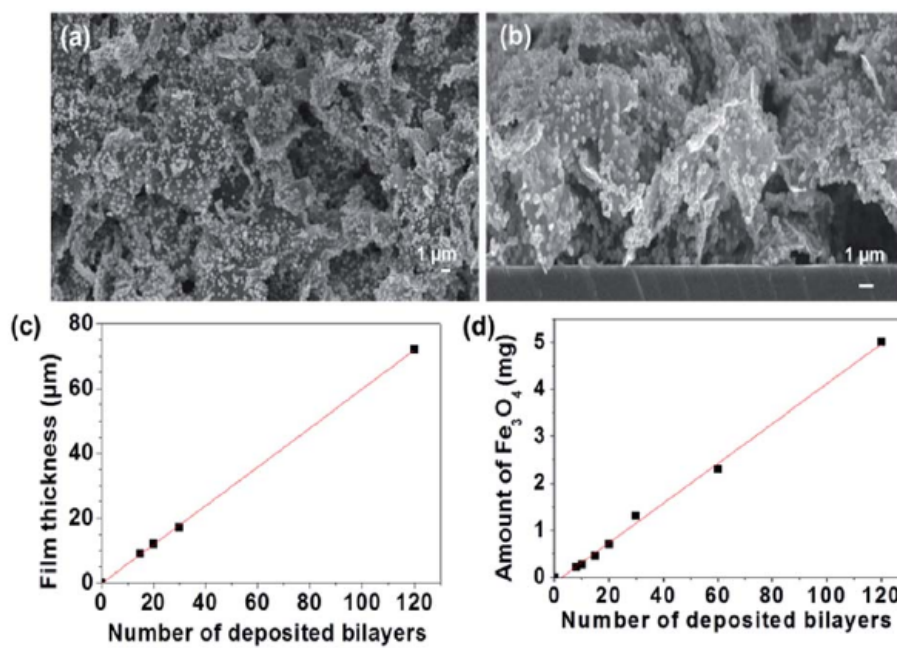


Figure 3.8: The typical SEM images of 15 layers of the Fe₃O₄/FLG // PEDOT:PSS deposit: (a) atop and (b) cross-section views; dependencies of the deposit thickness (c) and mass of Fe₃O₄ (d) on the number of deposited layers [12].

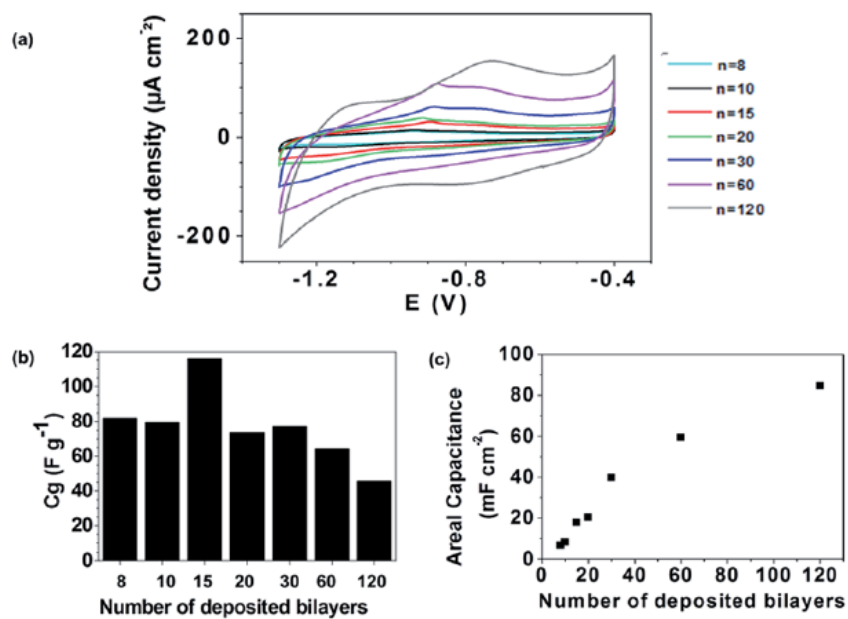


Figure 3.9: (a) The typical CV curves of the 15-layered ($\text{Fe}_3\text{O}_4/\text{FLG} // \text{PEDOT:PSS}$) electrode in $0.5\text{M Na}_2\text{SO}_3$ at 1 mV/s . The dependence of the specific capacitance of the electrode layer on the number of deposited layers: the mass specific capacitance (b) and the capacitance referred to the geometric surface area (c) [12].

demonstrated the capacitance equal to 132 F/g at 0.5 A/g and the retention equal to 87% after 200 cycles in 0.1M Na₂SO₃ [148]. The nanorods of the goethite uniformly dispersed on rGO sheets demonstrated the capacitance above 450 F/g (at 1 A/g) in 1M KCl [149], and the retention of 87% of the initial capacitance after 10³ cycles at 2 A/g. It is claimed that the uniform distribution and fine contact of oxide material with the flexible rGO substrates is responsible for this impressive performance.

The doping of the goethite crystals with Co results in a significant improvement of the capacitance and its retention [150]: the deposit of 3.6% Co-doped α -FeOOH demonstrated the capacitance equal to 463.18 F/g at 0.1 A/g in 1M KOH and the excellent retention equal to 96.3% after 10³ cycles. The improvement of the performance was explained by the influence of the dopant Co³⁺ cations on the energy level of the oxygen *p*-electrons and the decrease in the band gap by 0.24 eV.

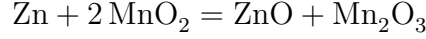
The lepidocrocite γ -FeOOH is less stable than the goethite. However, the advantage of the lepidocrocite is its 2D-layered structure with the interlayer channels facilitating the ion transport [136]. For example, the thick (30-50 nm) nanosheets of γ -FeOOH with the length ca. 1.4 μ m were electrochemically deposited on the carbon cloth. The high value of the mass specific capacitance $C_g = 310.3$ F/g was detected at 0.2 A/g and more importantly, only a mediocre drop of the capacitance to 219.5 F/g was observed at very high charging rates of 12.6 A/g (both in 3M KCl) [146]. This indicated the efficient ion transport within the electrode layer.

Oxides of Mn

The manganese oxides form the second most studied group of oxides (after RuO₂) as electrode materials for supercapacitors. Numerous reviews were published exclusively devoted to the manganese oxides electrode materials [151, 82, 152]. The manganese oxides are relatively abundant and cheap, and environmentally neutral. In contrast to the most of transition metals, Mn has a wide range of stable oxidation states, from Mn⁰ as the metal to Mn⁷⁺ as the permanganate anion MnO₄⁻. Mn forms several oxides stable in aqueous solutions: MnO (easily oxidizes to Mn₂O₃), Mn₃O₄, Mn₂O₃, MnO₂. Another oxide Mn₂O₇ is a strong oxidant, reacting with water to form MnO₂ and O₂.

The oxide of Mn^{IV}, namely, **MnO₂**, is by far the most intensively utilized

oxide of manganese in the field of electrochemical energy storage. The cathode redox transition $\text{MnO}_2/\text{Mn}_2\text{O}_3$ is commonly used in the non-rechargeable alkaline batteries with the Zn anodes:



The reversibility of both Zn anodes and MnO_2 cathodes can be improved by the application of nanostructured materials, in particular, the MnO_2 nanofibers [153]. The retention of 92% of the initial capacitance of such batteries after 5000 cycles at 5C rate was reported [153]. The MnO_2 -based cathodes are also commonly utilized as cathodes of the Li-ion rechargeable batteries [95, 154].

Since the work [91], where the capacitive behavior of the MnO_2 oxide in neutral electrolyte (2M KCl) was first demonstrated and $C_g = 199$ F/g and its 100% retention after 100 cycles were claimed, there were intensive studies of application of MnO_2 as electrode materials for supercapacitors. The maximal charge storage, assuming $1e^-$ per Mn atom was $Q_C=1102$ C/g or 918 F/g for the potential range of 1.2V, which was utilized in [91]. In [155] an even higher value of the capacitance equal to 1250 C/g was obtained for the thin deposit of amorphous particles of MnO_2 . The amorphous hydrated $\alpha\text{-MnO}_2$ is typically formed by the low-temperature chemical synthesis or the electrodeposition from Mn^{2+} salts. High observed values of Q_C indicate the high efficiency of the charge storage in $\alpha\text{-MnO}_2$, related to the following suggested redox transition [155]:



However, such high value $Q_C=1250$ C/g or the capacitance $C_g=1380$ F/g were reported for the thin films of MnO_2 only. For example, the low loading ($13.3 \mu\text{g}/\text{cm}^2$) MnO_2 deposit on the Pt substrate [155] showed the high capacitance, while the increase of the loading to $66.7 \mu\text{g}/\text{cm}^2$ resulted in the film of the thickness equal to ca. $5 \mu\text{m}$ with the capacitance decreased to 930 F/g. In the most of experimental studies, the films with the thicknesses around $100 \mu\text{m}$ were used, and the capacitances $C_g \approx 130 - 150$ F/g were generally reported [104, 156]. Such significant decrease in the electrochemical capacitance with the deposit thickness was attributed to a limited conductivity of MnO_2 , both electronic and ionic.

The conductivity of MnO_2 varies with its crystal structure. The rutile-type $\beta\text{-MnO}_2$ (pyrolusite) is an n -type semiconductor [157] with a low electronic con-

ductivity $\sigma \approx 10^{-6} \text{ Ohm}^{-1} \cdot \text{cm}^{-1}$ [103]. β - MnO_2 consists of the MnO_6 tetrahedra forming the compact structure with (1x1) tunnels, i.e. a tunnel with dimensions close to the size of the MnO_6 tetrahedra, $2.3 \times 2.3 \text{ \AA}$. These relatively narrow tunnels provide not very high ionic conductivities. If MnO_2 is formed relatively fast in aqueous solutions, then water molecules can stabilize larger tunnels. The examples are the (2x2) tunnels in α - MnO_2 (cryptomelane), the (2x1) tunnels in ramsdellite structure, or the alternating ramsdellite (2x1) and rutile (1x1) domains in γ - MnO_2 [95]. These polymorphs of MnO_2 are reported to have higher electronic and ionic conductivities [103] comparing to β - MnO_2 . Upon the reversible cation insertion, the α - MnO_2 structure with large (2x2) tunnels can become destabilized [95], resulting in the loss of performance. The ramsdellite and γ - MnO_2 show a better stability [158, 159].

The controlled annealing of the amorphous MnO_2 , which is obtained by the reduction of the aqueous solution of KMnO_4 and contains a significant amount of K^+ inclusions, results in the formation of the δ - MnO_2 oxide (birnessite) [160]. The birnessite has the layered structure of β - MnO_2 sheets separated by water and the ions insertion. In particular, the decrease of K^+ content in the birnessite, caused by its washing in acidic or neutral aqueous solutions, results in the increase of the inter-layer separation and the SSA of the material. δ - MnO_2 shows the electrical conductivity comparable to that of β - MnO_2 . However, δ - MnO_2 has a significantly higher ionic conductivity [103].

The spinel oxide λ - MnO_2 can be obtained by the de-lithiation of the spinel LiMn_2O_4 by the hydrolysis in HCl . Despite the absence of large regular tunnels in the spinel structure, the high ionic conductivity of λ - MnO_2 was reported [103].

The electrochemical properties of MnO_2 depend significantly on its crystal structure. This dependence was studied in details in [160] and [103]. It is important to emphasize that it is difficult to isolate the effect of crystal structure, because the material capacitance depends also on SSA and porosity. Since the conditions of the synthesis of different polymorphs of MnO_2 are substantially different, the SSA and porosity of final materials varied too, which can explain certain disagreement between the studies [160] and [103]. Nevertheless, these studies present several common observations. In particular, the lowest specific capacitance was observed for the pyrolusite β - MnO_2 and explained by its low conductivity. β - MnO_2 is the most compact phase among the above mentioned oxides. Significantly higher capacitances were detected for more open phases, such as the cryptomelane α -

MnO₂. Even a higher capacitance was reported for the birnessite δ -MnO₂. It is important to notice that the DFT modeling demonstrates that despite a low bulk conductivity, the surface conductivity of β -MnO₂ is much higher, because of the presence of the surface states [161]. Thus, the nanostructured MnO₂ mixed with a conductive component (carbon) makes a promising class of electrode materials for supercapacitors.

Most of the studies of the MnO₂ electrodes for supercapacitors were performed in neutral solutions, namely, chlorides or sulfates of K or Na. There are only few studies of the capacitance of the manganese oxides performed in alkaline electrolytes. It was observed [162] that the capacitance of the same material (MnO₂ deposited on the carbon nanotubes) was ca. 25% higher in 1M KOH than in 0.5M Na₂SO₄, while the same mechanism of charge storage was assumed. The electrodeposited manganese oxide also demonstrated a substantially higher specific capacitance in 1 M NaOH [163] comparing to 0.5M Na₂SO₄ [164]. The intriguing aspect of the studies in alkaline electrolytes is the existence of a relatively wide potential range of the stability for the reduced manganese oxides: Mn₂O₃ (at pH > 7) and Mn₃O₄ (at pH > 10.5) (Fig.3.6(D)). It was suggested that the redox transitions of these oxides could allow a more significant change of the oxidation state of Mn in the potential range of 1V [165], thus, increasing the pseudocapacitance of the oxide.

The detailed XPS analysis of the changes in intensities of the O 1s and Mn 2p XPS signals between the fully charged (oxidized) and discharged (reduced) α -MnO₂ in 0.1M Na₂SO₄ confirmed that the reaction (3.11) was the main mechanism of charge storage. This reaction results in the change of average oxidation state of Mn from 3.1 for the reduced state to 4 for the oxidized state. The high values of the detected Q_C indicate that the reaction (3.11) can propagate into the bulk of MnO₂ particles. On the other hand, despite numerous claims in literature of electrolyte cation insertion into the bulk of MnO₂, the amount of Na and S detected by the XPS is attributed to the adsorption of the electrolyte cations Na⁺ and anions SO₄²⁻ exclusively on the surface of oxide [9].

The oxides of manganese with lower oxidation states, namely, the birnessite Mn₂O₃, MnOOH, and the spinel Mn₃O₄ are studied significantly less than MnO₂. The main reason is that the intrinsic electronic conductivity of these oxides is much lower [157]. In particular, the conductivity of Mn₃O₄ is $\sigma = 10^{-7} \text{ Ohm}^{-1} \cdot \text{cm}^{-1}$. The other problem is the instability of lower oxidation states of Mn²⁺/Mn³⁺. This

instability is caused by the irreversible oxidation to Mn^{4+} upon potential cycling, which was proved by the XANES measurements [166]. This effect was observed for both Mn_2O_3 and Mn_3O_4 oxides and resulted in the unexpected decrease of the mass specific capacitance (measured in 0.1 M Na_2SO_4) by 21% in 300 cycles: from 230 F/g to 180 F/g. It is interesting that a significantly higher capacitance of Mn lower oxidation state oxides was observed in alkaline electrolytes, comparing to neutral electrolytes. For example, Mn_2O_3 on the mesoporous carbon in 6M NaOH provided 651 F/g with 85% retention after 800 cycles [152]. A composite of the spinel Mn_3O_4 and the porous carbon demonstrated the specific capacitance equal to 600 F/g in 1M KOH, but at a very low charging rate (0.1 mV/s) [167]. The capacitance dropped to 340 F/g at 1 mV/s rate, indicating the limitations related to the low conductivity of Mn_3O_4 . It is important to emphasize that in the studies of electrochemical properties of Mn_2O_3 and Mn_3O_4 in alkaline electrolytes, few pairs of CV redox peaks were clearly observed, contrary to MnO_2 , which demonstrated relatively flat CV curves. The presence of the CV redox peaks clearly indicates the contribution of pseudocapacitance into the charge storage.

Case study: $\text{Mn}_3\text{O}_4/\text{C}$ composites as supercapacitors electrode material

In this subsection the synthesis and the properties of the spinel (hausmannite) Mn_3O_4 oxide in the composite with the Vulcan carbon are discussed. This composite was developed in the ICPEES and studied by the author in details [13].

The electrochemical properties of the Mn_3O_4 spinel oxide were studied thoroughly for the composite of the oxide nanoparticles and the XC-72 Vulcan carbon [13]. The composites were prepared by the solid state combustion synthesis (SSC), which is commonly used for the preparation of the oxide nanosized powders [168, 169, 170]. The SSC method has been adapted in the ICPEES by Dr. Kéranguéven for the preparation of the composites of metal oxide nanoparticles with carbon, which are used as electrocatalysts in the oxygen reduction reaction [171]. The modified SSC method was named as the in situ autocombustion or the ISAC method.

In the original SSC method, a precursor salt of a transition metal (mostly nitrate or carbonate) is mixed with a fuel component. A fuel component is a substance capable to decompose at moderate temperature with a strong exothermic effect. Most commonly used fuel components are glycine ($\text{C}_2\text{H}_5\text{NO}_2$), citric acid

Substance	$\Delta_r H$, kJ/mol	C_p , J · mol ⁻¹ · K ⁻¹
Reagents		
Mn(NO ₃) ₂ · 4 H ₂ O	500	-
Glycine	-973	-
Products		
Mn ₃ O ₄	-	44
C, graphite	-	8.5
N ₂	-	31
CO ₂	-	54
H ₂ O	-	45

Table 3.2: The parameters for the calculation of reaction temperature (3.12) for the synthesis of Mn₃O₄ from the Mn nitrate with glycine as a fuel.

(C₆H₈O₇), urea ((NH₂)₂CO). The heat generated by the decomposition dissipates fast, providing enough heat to decompose the metal salt into well crystallized oxide particles and, at the same time, avoiding the sintering of the particles. The size of the particles depends on the weight ratio of salt to fuel [170]. The temperature T_r , generated within the reaction media, can be estimated by the equation

$$T_r = T_0 + \frac{\sum_i (-\Delta_r H_i \cdot n_i)}{\sum_j C_{p,j} \cdot m_j}, \quad (3.12)$$

where T_0 is the externally applied temperature, i is the index of decomposing reagents, j is the index of the products of the decomposition reactions. The i^{th} reagent generates the heat $-\Delta_r H_i$ (in J/mol) and is present in the n_i molar quantity. The j^{th} product has the specific heat capacitance $C_{p,j}$ (in J · mol⁻¹ · K⁻¹) and the mass m_j . The parameters of the equation (3.12) for the synthesis of Mn₃O₄ by the decomposition of Mn(NO₃)₂ · 4 H₂O with glycine as a fuel are given in Table 3.2. It is important to note that the equation (3.12) gives an estimate of the temperature and not the exact value, because of the assumption about a weak dependence of the specific heat capacitance on the temperature.

In comparison to the original SSC synthesis, the presence of carbon in the ISAC synthesis decreases the temperature of the media due to a high heat conductivity of the carbon. Using (3.12), the effect of the presence of the carbon in the reaction media is evaluated. The dependence of the reaction temperature on the weight percentage of the oxide in the Mn(NO₃)₂ - glycine - carbon mixture is shown in Fig.3.10. It appears that the loading of carbon up to ca. 70% decreases the

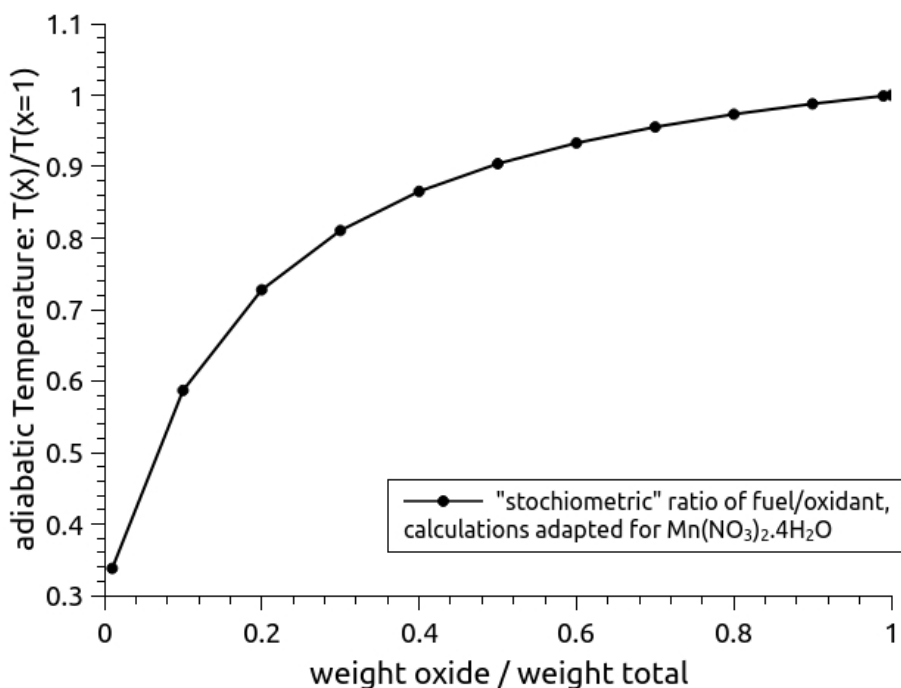


Figure 3.10: The dependence of the reaction temperature in the ISAC synthesis for the $\text{Mn}(\text{NO}_3)_2 \cdot 4\text{H}_2\text{O}$ - glycine - carbon mixture on the weight ratio of the oxide. The molar ratio of nitrate and glycine is fixed to provide the optimal conditions.

temperature of the reaction media only by ca. 20%. It can be explained by a relatively low heat capacitance of the carbon, comparing to the other products of the ISAC reaction (see Table 3.2).

Indeed, the composites of $\text{Mn}_3\text{O}_4/\text{C}$ can be prepared by the ISAC method in a relatively wide composition range: at least from 7%_{wt} to 87%_{wt} of the oxide [13]. The composite consists of the Mn_3O_4 nanoparticles with the size range 20-30 nm, which are distributed uniformly over the carbon substrate. As it was discussed in Chapter 3.2, the mixing of the components in the ISAC synthesis is much more efficient comparing to the mechanical mixing. Such effective mixing results in a high specific capacitance and its weaker dependence on the charging rate (Fig. 3.4).

The specific capacitance of these composites shows strong dependence on their compositions (Fig.3.11). In particular, the presence of a relatively small (18%_{wt}) amount of the oxide in the composite results in the 2-fold increase of the specific capacitance. The maximum capacitance $C_g = 270 \text{ F/g}$ was obtained for the com-

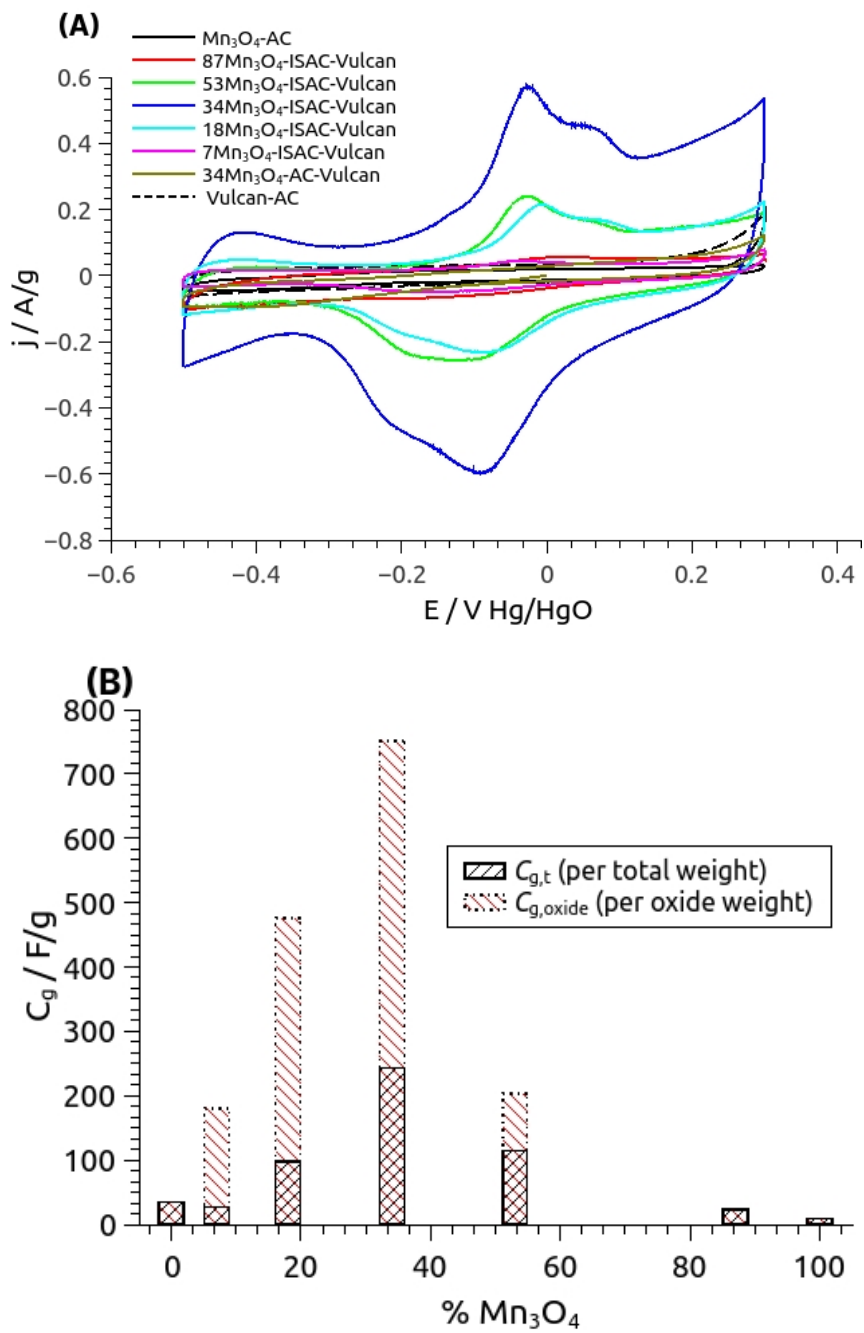


Figure 3.11: (A) The CV curves of the $\text{Mn}_3\text{O}_4/\text{C}$ composites with various compositions measured in 1M NaOH, 20 mV/s. (B) The dependence of the specific capacitance of the $\text{Mn}_3\text{O}_4/\text{C}$ composites in 1M NaOH on their composition [13].

posite containing 34%_{wt} of the oxide in Mn₃O₄/C (at 1 mV/s in 1M KOH). Further increase of the oxide content resulted in the rapid decrease of the total capacitance due to the agglomeration of the oxide particles. The cyclic voltammetry of the Mn₃O₄/C composites clearly showed several pairs of the quasi-reversible redox peaks, indicating the contribution of pseudocapacitance into the charge storage (Fig.3.11(A)).

By taking into account the specific capacitance of the carbon, measured separately, the specific capacitance of oxide particles can be calculated from the total capacitance of the composite. For the optimized composition the specific capacitance of the Mn₃O₄ nanoparticles was found to be equal to $C_g=754 \text{ F/g}_{\text{oxide}}$ at 1 mV/s and 439 F/g_{oxide} at 500 mV/s. The surface-related charge storage capacitance (including the EDL and the pseudocapacitance) for MnO₂ was estimated to be equal to 100 $\mu\text{F}/\text{cm}^2$ [155]. Using the SSA value for 34%_{wt} Mn₃O₄/C, the contribution of the surface related capacitance to the total capacitance was estimated to be equal to 114 F/g. Thus, it can be concluded that the bulk of the Mn₃O₄ nanoparticles strongly participates in the charge storage in the composite. Indeed, the maximal charge storage capacitance for Mn₃O₄ calculated by (3.2) is $Q_C = 1264 \text{ F/g}$. The experimental value of $C_g=754 \text{ F/g}_{\text{oxide}}$ indicates that more than a half of the bulk Mn atoms are involved in the charge storage at least at slow potential sweep rates.

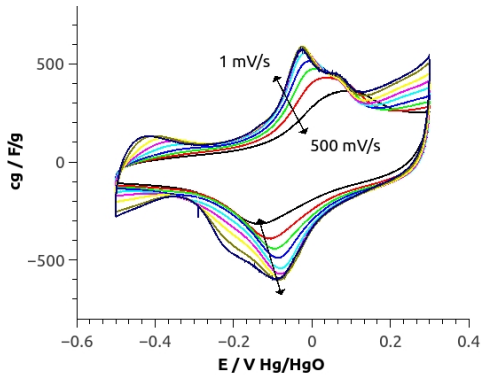


Figure 3.12: The dependence of the differential capacitance of the 34% Mn₃O₄/C composite on the potential sweep rate [13].

v is a sweep rate (in V/s) (Fig.3.12).

According to the Pourbaix diagram (Fig.3.6(D)), the peaks below -0.4V vs

The dependence of the charge storage potential profile on the charging rate can be analyzed by comparison of the CV curves measured at different sweep rates. For better comparison, the currents are recalculated to the specific differential capacitance c_g using the following equation:

$$c_g = \frac{i_m}{v}, \quad (3.13)$$

where i_m is the mass-specific current density measured by the CV (in A/g),

Hg/HgO (0.52V vs. SHE) can be attributed to the reduction of Mn^{3+} to Mn^{2+} . The peaks in the range -0.20..0.00V Hg/HgO (0.72 .. 0.92V SHE) can be attributed to the oxidation of Mn^{3+} to Mn^{4+} . As Fig.3.12 shows, the pseudocapacitance related to the $\text{Mn}^{3+}/\text{Mn}^{2+}$ transition is slower, and its contribution is decreasing faster with the potential sweep rate increase, in comparison to the decrease for the $\text{Mn}^{4+}/\text{Mn}^{3+}$ transition. The latter transition provides a significant contribution even at 500 mV/s.

A more detailed insight on the nature of the pseudocapacitance for the Mn_3O_4 particles was obtained from the measurements performed in the set of $\text{Na}_2\text{SO}_4 + \text{NaOH}$ electrolytes with various pH (Fig.3.13). It is important to note that the composition of electrolytes in [13] was adjusted to change the value of pH and keep a constant concentration of the Na^+ cation. The inset in Fig.3.13 shows the dependence of the open circuit potential E_{OCP} of the $\text{Mn}_3\text{O}_4/\text{C}$ electrode on pH. The systematic shift of E_{OCP} equal to 80 ± 20 mV/pH was detected. For all values of pH, the value of E_{OCP} was observed in the range of the Mn_2O_3 stability according to the Pourbaix diagram. This indicates that the Mn_3O_4 particles are partially oxidized, at least on the surface, during the preparation of the electrode.

The systematic decrease of the pseudocapacitance-related peaks of the CV with the decrease of pH (Fig.3.13(A)) was detected. This is in agreement with the above mentioned comparative studies of the MnO_2 capacitance in NaOH and Na_2SO_4 electrolytes, although for the $\text{Mn}_3\text{O}_4/\text{C}$ composites the effect is much stronger. The observed shift of the CV peaks with pH $dE/dpH \approx 70 \pm 10$ V/pH confirms that the pseudocapacitance in the manganese oxides can be attributed to the process described by (3.11). It can be concluded that OH^- plays an important role in this process. One may also detect that the capacitance decrease with the potential sweep rate increase gradually becomes more significant at lower pH (Fig.3.13). The separation between the anodic and cathodic peaks around 0.00V Hg/HgO also increases from 70 mV at pH=14 to 140 mV at pH=11. It allows to conclude that the pseudocapacitance processes become gradually slower with the pH decrease.

Spinel oxides electrode materials

It is interesting to compare the capacitancies reported in the literature for 3 spinel oxides: Mn_3O_4 , Co_3O_4 [172], Fe_3O_4 [173] (see Table 3.3). Mn_3O_4 has the smallest

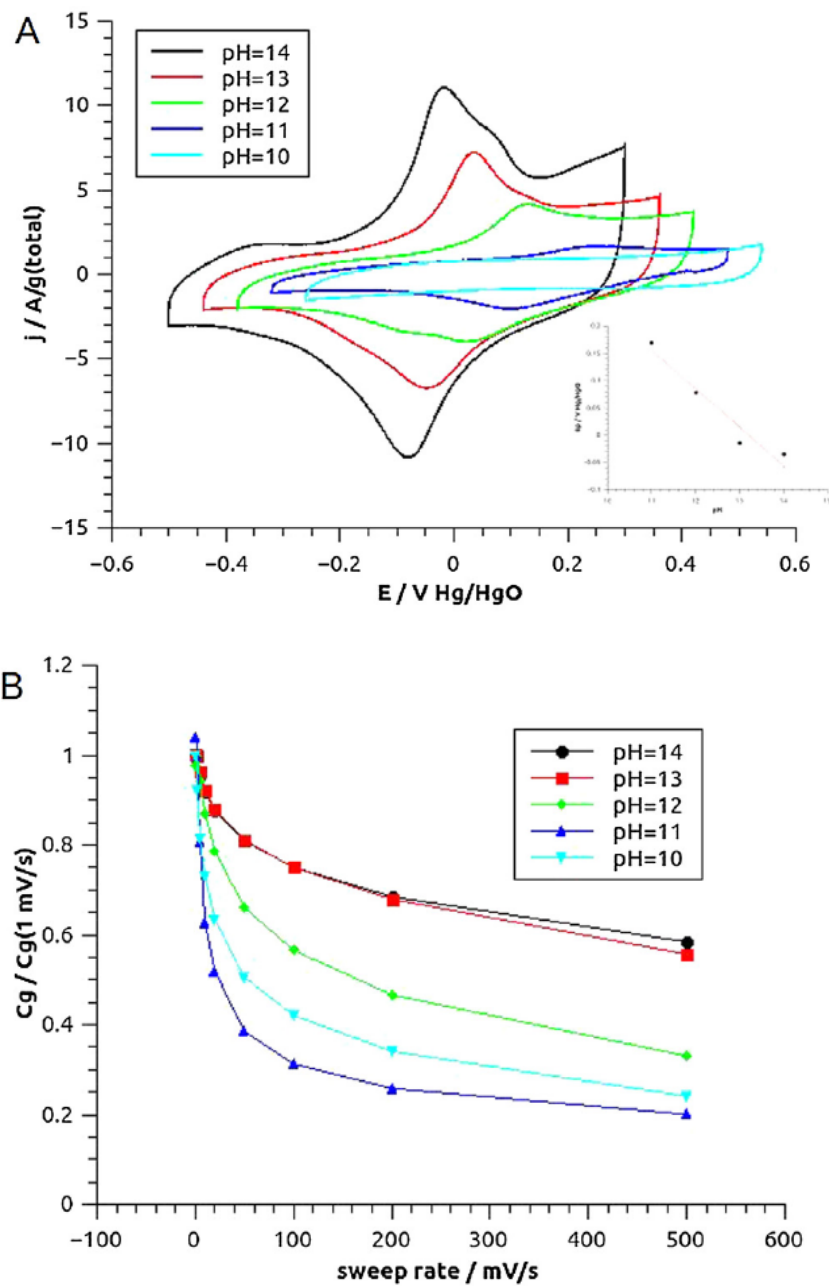


Figure 3.13: (A) The CV curves of the 34% Mn₃O₄/C composite at 20 mV/s measured at various pH. (B) The Decrease in the total specific capacitance with the potential sweep rate increase at various pH.

oxide	spinel	lattice parameter, Å	density, g/cm ³	specific capacitance, F/g	Ref.
Mn ₃ O ₄	normal	5.8	4.86	750	[13]
Co ₃ O ₄	normal	8.1	6.07	400	[172]
Fe ₃ O ₄	inverse	8.4	5.17	120	[173]

Table 3.3: The comparison of the structure and properties of the spinel oxides

lattice parameter and the most compact crystal structure (as evidenced by its lowest density). Mn₃O₄ has also the highest reported mass specific capacitance. However, it is hard to explain a higher capacitance of the Mn oxide by its more compact structure. In fact, as mentioned above, an increase in the interatomic spacing for the MnO₂ oxides resulted in a higher specific capacitance of α -MnO₂ comparing to β -MnO₂.

The ionic conductivity is claimed to be an important parameter, determining the efficiency of the charge storage. However, among the 3 spinel oxides, the conductivity decreases in the following order: Fe₃O₄ > Co₃O₄ > Mn₃O₄ [174], inversely to the increase in capacitance. Thus, the factors other than ionic conductivity play a more important role.

As discussed above, the redox transformation, which is responsible for the pseudocapacitance in Mn₃O₄, is a pH-dependent reaction (3.11). This reaction involves OH⁻ as a reagent. Thus, one can expect that the rate of reaction (3.11) depends on OH⁻ interaction energy with the oxide surface. It is interesting to note that Co₃O₄ and Mn₃O₄ are considered among the most promising catalysts for the oxygen electroreduction in the alkaline solutions [175]. The modeling of the interaction of water with the Mn₃O₄ cluster demonstrates, that the water molecules are significantly stronger and dissociatively adsorbed on the Mn²⁺ sites of Mn₃O₄ than on the Mn³⁺ sites [176]. This can explain a higher activity of the Mn₃O₄ oxide in the oxygen electroreduction in comparison to the MnO₂ and Mn₂O₃ oxides, and, more importantly for the present work, its higher pseudocapacitance in alkaline solutions. Moreover, a higher activity of the substituted spinel MnFe₂O₄ comparing to Fe₃O₄ in the oxygen electroreduction was reported [177], confirming that the reaction is facilitated in the presence of the Mn²⁺ sites, most probably, due to a stronger water adsorption. Similarly, a higher activity of the MnCo₂O₄ spinel comparing to Co₃O₄ was demonstrated [178].

It allows to suggest that the dissociative adsorption of water influences the rate of the process of pseudocapacitance in the TMO nanoparticle.

In Section 3.3.4 the impedance of $\text{Fe}_3\text{O}_4/\text{C}$ and $\text{Mn}_3\text{O}_4/\text{C}$ electrodes is discussed. These systems are considered as the examples of systems with significant contribution of pseudocapacitance to the total charge storage.

3.3.4 Impedance of porous electrode/electrolyte interface with pseudocapacitive behavior

The generalized staircase model of the impedance of porous electrodes is described in Section 1.3. This model predicts that the influence of the porous structure on the measured impedance can be detected at the low frequencies under the condition that the redox pseudocapacitance reaction is sufficiently fast. However, it is difficult to fit the measured EIS spectra quantitatively. As for the carbon electrodes, the macro-structure of the deposit of the material must be taken into account. Thus, only qualitative interpretation of the experimental Nyquist plots is given below.

The dependence of the impedance on the rate of the interfacial reaction is shown in Fig.1.22(A) in Section 1.3.

Fig.3.14 shows the impedance spectra for 2 various electrodes with the strong contribution of pseudocapacitance: the $\text{Fe}_3\text{O}_4/\text{FLG}$ 15-layered deposit with the PEDOT as a structurizing agent (Fig.3.14(A)) and the $\text{Mn}_3\text{O}_4/\text{C}$ deposit (Fig.3.14(B)). The spectra were measured at the potential of the open circuit, i.e. close to the equilibrium potential of the redox transition of the oxide materials (in the absence of other redox active components in the system).

In both cases the low frequency segments of the Nyquist plots show the straight inclined line, indicating the capacitive behavior. A slight inclination corresponds to the CPE constant $a = 0.90$ for $\text{Fe}_3\text{O}_4/\text{FLG}$ and $a = 0.80$ for $\text{Mn}_3\text{O}_4/\text{C}$ electrodes. Higher values of a for $\text{Fe}_3\text{O}_4/\text{FLG}$ are expected, because the $\text{Fe}_3\text{O}_4/\text{FLG}$ deposit has the ordered layered structure with the PEDOT interlayers, thus, having the open regular porous structure. In comparison to this material, the structure of $\text{Mn}_3\text{O}_4/\text{C}$ is more disordered, resulting in a lower a value.

At high frequencies a semi-circle segment of the Nyquist plot for $\text{Fe}_3\text{O}_4/\text{C}$ electrode is observed (Fig.3.14). This behavior is predicted by the generalized staircase impedance model (Fig.1.22(A)). The transition from the semi-circle to the

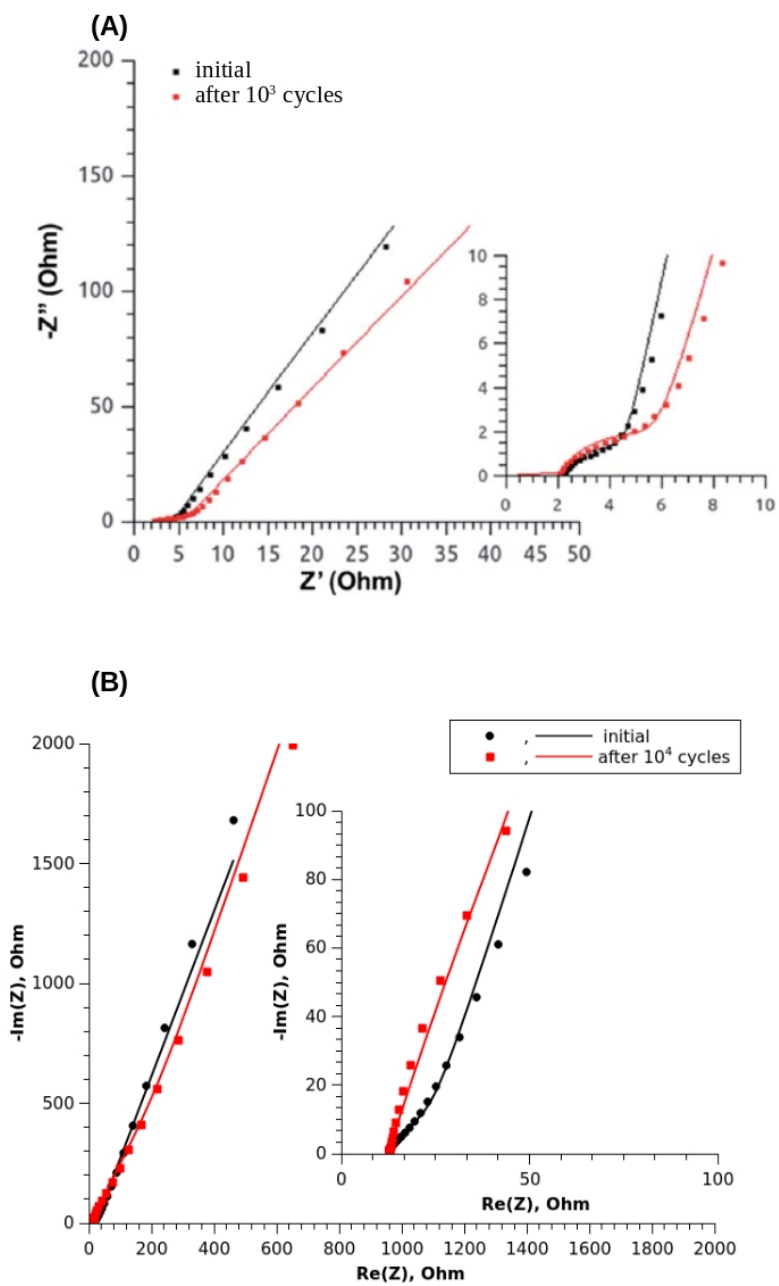


Figure 3.14: (A) The EIS spectra of the $(Fe_3O_4@FLG/PEDOT)_{15}$ electrodes in 0.5M Na_2SO_3 [12]. (B) The EIS spectra of the Mn_3O_4/C electrode in 1M NaOH [13]. The insets show the high frequency range of the EIS spectra.

straight inclined segment for $\text{Mn}_3\text{O}_4/\text{C}$ is observed at the higher frequencies than for $\text{Fe}_3\text{O}_4/\text{C}$. This difference indicates a faster kinetics of the pseudocapacitance reaction (i.e. a lower R_{ct}) for $\text{Mn}_3\text{O}_4/\text{C}$. This observation correlates well with the significantly higher values of C_g for $\text{Mn}_3\text{O}_4/\text{C}$ comparing to $\text{Fe}_3\text{O}_4/\text{C}$.

The application of 10000 charging cycles results in the strong loss of capacitance for the $\text{Mn}_3\text{O}_4/\text{C}$ electrodes due to low retention. This is in contrast with the high retention of the $\text{Fe}_3\text{O}_4/\text{C}$ electrodes under the similar conditions. This difference is reflected in the impedance spectra. For Mn_3O_4 , the strong increase of the diameter of semi-circle is detected, reflecting the increase of R_{ct} , i.e. the significant decrease in the rate the pseudocapacitance reaction. The semi-circle part of the EIS spectra for $\text{Fe}_3\text{O}_4/\text{C}$ barely changes, except the higher values of C_{dl} result in the transition to the capacitive behavior at the lower frequencies.

3.4 Conclusions

Due to the pseudocapacitance phenomena, the transition metal oxides are the promising materials for the application as electrodes in supercapacitors. The pseudocapacitance involves the redox reaction of the transition metal cation and the intercalation of the electrolyte cation (for example H^+ , or Na^+ , K^+). The tuning of the TMO structure allows to achieve a high utilisation of the charge storage capacity of the material. However, the following important points have to be taken into account.

- *Well crystallized oxides.* One of the factors limiting the efficiency of the TMO in supercapacitors is their low electronic conductivity. Electronic conductivity depends on the oxide structure and crystallinity: amorphous oxides are generally less conductive due to a higher resistance at the crystal grain boundaries. Thus, well crystallized oxides are preferable as the electrode materials for supercapacitors.
- *Oxide/carbon composites.* Even for relatively high intrinsic electronic conductivities, the interparticles resistance, related to the small area of contact between particles, results in the high serial resistance. Thus, the efficient strategy is to mix the TMO particles with a conductive material, in particular, with carbon. The TMO/C composites are among the most promising materials for supercapacitor electrodes. It is important that the TMO

nanoparticles are distributed uniformly over the carbon, in order to avoid the agglomeration and interparticle contacts.

- *A weak influence of the ionic conductivity.* Contrary to the frequent claims in the literature, the ionic conductivity of TMO seems to have little or even no influence on the TMO performance in supercapacitors. This fact is derived from the evaluations of the conditions for the ionic transport in the metal oxide particles under the uniform potential distribution. For this evaluation the solid state diffusion coefficient values reported in the literature were used.
- *The fast kinetics of interfacial charge transfer.* The important factor of the TMO performance as supercapacitor materials is the kinetics of the pseudocapacitance reaction, involving the interfacial charge transfer and preceding the ion intercalation. The impedance modeling (Section 1.3) demonstrates that the fast kinetics is necessary to observe a significant impact of the pseudocapacitance at the potential modulation rates typical for the supercapacitors utilization. This conclusion is supported by the frequent observation of the correlation between the capacitance of oxide materials and their electrocatalytic activities in the reactions with electrolyte components, such as the oxygen electroreduction.
- *Electrochemical stability.* Reversibility of the charge/discharge process is another important characteristic of the supercapacitors performance. Thus, the retention of initial capacitance at least 80% after 10^5 charging cycles is one of the crucial requirements. However, a significant decrease in the capacitance of the TMO electrodes with the cycling is often observed. This decrease is caused by the degradation of the TMO. The degradation can be related to the irreversible formation of an oxide phase with a lower conductivity or the formation of a soluble phase. The analysis of the stability of the oxide phase can be done using the Pourbaix diagrams (Fig.3.6). The most of TMO are stable in neutral or weak alkaline electrolytes, thus, limiting the choice of aqueous electrolytes. The oxides of Mn, Fe, Co and Ni are among the oxides, which show a sufficient stability in neutral/alkaline electrolytes and the reversible redox transition. From the viewpoint of sustainable development, the first two oxides in this group are of a special interest due to their high abundance and low toxicity.

- *Spinel oxides as electrode materials.* The spinel oxides Mn_3O_4 and Fe_3O_4 are the most interesting candidates among the binary oxides of Mn and Fe for using as supercapacitors electrode materials. This is due to their relatively high ionic and electronic conductivity. In particular, the $\text{Mn}_3\text{O}_4/\text{C}$ composite demonstrates the specific charge capacitance of the oxide particles above 750 F/g at 1 mV/s in 1M NaOH. Therefore, the Mn_3O_4 nanoparticles demonstrate the high efficiency of charge storage. The capacitance of the magnetite Fe_3O_4 is not very high, ca. 120 F/g. However, the magnetite is outstandingly stable: the retention of 114% of the initial capacitance was detected after 1500 cycles at 1A/g charging rate. The development of the composites with the substituted spinel oxides, based on the Mn and Fe spinels, such as MnFe_2O_4 , is a promising approach towards new electrode materials.

Chapter 4

Future projects

The transition towards the energy networks based on the renewable primary sources, such as solar energy and wind, is one of the most pressing challenges of our time. Considering the intermittent character of these sources, the efficient and reversible energy storage devices are necessary and important components of such network. The electrochemical energy storage devices, in particular batteries, supercapacitors and hybrid cells are known to provide an outstanding energy storage reversibility and efficiency, compact structure and zero operation emission. In particular, supercapacitors can provide the energy density above 10 W.h/kg at high power output (higher than 1 kW/kg) and keep at least 80% of their performance after 10^5 charging cycles.

The performance of supercapacitors is determined by the properties of electrode materials, such as electronic and ionic conductivity, specific surface area, accessibility for electrolyte, electrochemical stability and structural integrity during charging/discharging [1]. Thus, the development of supercapacitors with high performance requires the optimization of these properties of electrode materials.

Two classes of electrode materials play a key role in the development of supercapacitors: the carbon materials and the transition metal oxides. In the current section the author presents the planned projects which are the continuation of the current activities in the development of new materials for supercapacitor electrodes.

4.1 Bio-sourced activated carbon

The carbon materials have a high electronic conductivity and electrochemical stability. They are used as electrode materials in the electrochemical double layer capacitors (EDLC). Their performance is limited by a moderate charge storage capacitance, which is less than $15 \mu\text{F}/\text{cm}^2$. Thus, a high specific surface area (SSA), which is readily accessible for an electrolyte, is crucial for the high energy density.

The activated carbon (AC) materials provide outstanding SSA values (above $2000 \text{ m}^2/\text{g}$), resulting in high specific charge capacitances. The AC carbons are prepared by the physical (thermal) or chemical activation (see Section 2.4). The chemical activation provides a better control on the porosity of the final material and requires a lower energy input. Thus, the chemical activation is generally preferred for the AC synthesis. An additional advantage of the chemical activation method is that relatively cheap and abundant sources of carbon can be used for the mass-scale AC synthesis. For example, the AC electrodes with high charge capacitances (close to $300 \text{ F}/\text{g}$), excellent retention of capacitances with fast charging rates up to $20 \text{ A}/\text{g}$ and with charging cycles up to 10^4 were prepared from a fig fruit [10]. This approach is very useful from the viewpoint of the valorisation of bio-mass wastes: agricultural, agro-industrial, urban and wood production wastes [179, 180, 181].

In the recent years, the particular interest has been attracted to the microwave-assisted chemical carbon activation due to its high yield, short synthesis time, and low energy input [180, 181]. When the KOH/NaOH-etching approach is assisted by the microwave treatment, the AC with SSA large than $2000 \text{ m}^2/\text{g}$ and the high contribution of micropores are synthesized.

The tuning of the conditions of the microwave-assisted synthesis of the AC from biomass wastes requires careful study, considering the variability, complex structure and composition of biomass sources. This study is proposed as a part of the future project devoted to the development of new carbon electrode materials for supercapacitors.

In particular, the food waste treatment is very beneficial from the viewpoint of sustainable development [89]. The food waste is a renewable source, highly rich in cellulose and sugar. Contrary to agricultural wastes, the food waste is rich in the lignocellulose. The valorisation of food wastes decreases the landfill pressure. The

thermal pretreatment (in the air with $t^\circ < 300^\circ\text{C}$) is needed for standardization of waste sources and decrease of water content in the precursor.

The activation conditions must be tuned in order to obtain a desired AC structure with high SSA, controlled porosity, structural integrity and electrochemical stability. For example, the addition of NaCl in a certain proportion to the carbon source increased the graphitization of the final carbon product and its charge capacitance and electrochemical stability [11]. The control of the material porosity is important to provide the possibility of applying the final material as a carbon electrode in supercapacitors or using it as a component for the TMO/C composite materials. In the first case, the microporosity with the pore size $d < 1$ nm is favored in order to provide a high SSA. For the synthesis of the TMO/C composites, larger pores are required in order to provide the substrate for TMO nanoparticles growth.

Another important aspect of tuning of conditions for the AC synthesis is the optimization of its costs and energy input. Such optimization provides the potential for mass scale production of bio-sourced ACs for electrodes materials for supercapacitors.

4.2 TMO/C composite materials

The TMO materials are another most important class of materials for supercapacitor electrodes due to the TMO high energy density related to the phenomenon of pseudocapacitance. The pseudocapacitance involves a reversible redox transformation of the transition metal cation and/or intercalation of cation from an electrolyte into the sub-surface and the bulk of oxide phase. High rate and reversibility of charge storage reaction are crucial for the performance of supercapacitors. These requirements impose the necessity of shortening the ion diffusion path in the TMO bulk. Thus, the nanostructured TMO (nanoparticles, nanotubes, nanowhiskers, ...) are commonly used as electrode materials. For the nanoparticles, the optimal size is found in the range of 10-20 nm, providing a sufficiently large volume for the charge storage (high energy density) and a relatively short ion diffusion path (for high power output). The main factors, which limit the performance of the TMO as supercapacitor materials, are electronic conductivity (many TMO are semiconductors) and electrochemical stability.

The best performance in supercapacitors is reported for RuO_2 and related

oxides [115, 114, 110]: the charge capacitance larger than 900 F/g and the retention more than 80% after 10^5 cycles. However, these oxides are too expensive and toxic for wide commercialization. The Mn oxides (mostly MnO_2 , while lower oxidation degree oxides, such as Mn_2O_3 , Mn_3O_4 , MnOOH , have also been studied) also demonstrates the high charge capacitance larger than 600 F/g [9]. The high abundance and low toxicity of Mn make its oxides even more desirable from the viewpoint of sustainable development. In this context, the oxides of Fe are also considered as a promising candidate for supercapacitor electrodes materials. The low electrical conductivity of Fe_2O_3 prevents its utilisation in supercapacitors. However, a more conductive β - FeOOH was studied as an electrode material for supercapacitors [82, 150].

The spinel oxides, namely the oxides with the formula AB_2O_4 , where B is, most commonly, a trivalent transition metal, and A is a divalent metal cation, are of particular interest. These oxides often demonstrate a relatively high electronic conductivity and electrochemical stability. Namely, the spinels with $\text{B}=\text{Mn}^{3+}$, Fe^{3+} , and $\text{A}=\text{Mn}^{2+}$, Cu^{2+} , Mg^{2+} showed the high conductivity [174]. For example, the spinel Mn_3O_4 was studied as electrodes materials for supercapacitors, and the high charge capacitance was reported [182, 183].

High loading of electrode materials (above 100 mg/cm^2) requires relatively thick deposits of the TMO nanoparticles. Even for relatively conductive oxides, the interparticles resistance results in high serial resistance of such layers and requires the utilisation of a conductive additive, for example, the carbon. The carbon substrates with the well developed surface provide a possibility to immobilize the TMO particles and avoid their agglomeration. Thus, the development of the TMO/C composite materials is a promising strategy to obtain the electrodes materials with high performance in supercapacitors.

As mentioned above, the TMO nanoparticles with the size in the range of 10-20 nm are preferred. The well crystallized particles are expected to have a better performance, as the conductivity of the amorphous oxides is generally lower. Unfortunately, the preparation of the well crystallized TMO particles often require the thermal treatment at the elevated temperature, resulting in ripening, sintering, and agglomeration of the particles.

The solid state combustion (SSC) synthesis is a preparation method providing the possibility to form the crystallized TMO nanoparticles while avoiding the risk of the particles sintering. The SSC method was upgraded in the ICPEES for the

preparation of the TMO/C composites. In the upgraded method, the precursors of metal (nitrate or carbonate salts) are dissolved with a combustion additive (glycine, urea, or citric acid). After that, the carbon is ultrasonically dispersed in this solution. Then, the solvent is evaporated until the dry uniform mixture is obtained. At the next step, the fuel agent is ignited at a relatively low temperature ($100^\circ < t^\circ < 300^\circ\text{C}$), providing a local heat, which is necessary to decompose metal salts into a corresponding oxide. A fast evacuation of the heat allows to avoid the sintering of the TMO particles.

The upgraded SSC method was applied to synthesize the $\text{Mn}_3\text{O}_4/\text{C}$ composite with controlled structure and composition. This composite demonstrated a high charge capacitance (larger than $750 \text{ F/g}_{\text{oxide}}$) in 1M KOH, but a low capacitance retention (ca. 60% after 1000 cycles) [13]. The upgraded SSC method was also used for the preparation of the LaMnO_3/C composites for the oxygen electroreduction, proving that the composites with ternary oxides can be synthesized by the SSC.

In the planned project, the SSC method will further extended to the preparation of the spinel TMO/C composites with the general composition $\text{M}_x\text{Fe}_{2-x}\text{O}_4$, where $\text{M} = \text{Mn}^{2+}, \text{Cu}^{2+}, \text{Zn}^{2+}, \text{Ca}^{2+}$. The ferrite spinels are characterized by a high electrochemical stability (for example, the Fe_3O_4 oxide is used as a supercapacitor electrode [12]) and relatively high electronic conductivity. The capacitance of the MnFe_2O_4 oxide is reported to be higher than that of Fe_3O_4 [184, 185, 186] due to the stronger interaction of Mn^{2+} with water molecules and more facile cation insertion.

The extended SSC method will be applied to synthesize the $\text{M}_x\text{Fe}_{3-x}\text{O}_4$ oxides. The tuning of the ratio of metal precursors and combustion additives will be performed to ensure the control of the composition, including the substitution degree x and the crystal phase of the final oxide. After that, the method will be utilized to prepare the composites of $\text{M}_x\text{Fe}_{3-x}\text{O}_4/\text{C}$ with the controlled composition and structure of TMO particles. Both commercial carbon (for example, the XC-72 Vulcan) and the bio-sourced AC, prepared in the framework of the planned project, will be used for the composites.

4.3 Electrochemical study of supercapacitors performance

Firstly, the supercapacitors tests will include the utilisation of the model 3-electrode configuration with the electrode loadings below 1 mg/cm^2 . This will allow to avoid

the problems related to a possible non-uniformity of the thicker deposits. Also, the measurements in the 3-electrode cell allow to address more precisely the properties of the electrode material. This configuration also allows to avoid the complications related to the presence of a separator with low ionic conductivity comparing to a liquid electrolyte. In particular, the impedance spectroscopy in the optimal 3-electrode configuration allows to minimize the contributions of impedances of the counter electrode and the electrolyte.

The 3-electrode configuration will allow to determine the initial specific charge capacitance (from the CV measurements) and its dependence on charging rate and on the number of applied charging cycles (from the galvanostatic cycling). Using the EIS method, the mechanism of charge storage will be evaluated (EDL or pseudocapacitance). Moreover, the factors, which limit the contribution of pseudocapacitance for the TMO/C materials will be determined.

The 2-electrode configuration will allow to test the electrode materials in the conditions of a real supercapacitor, including high (above 1 mg/cm²) loadings of the electrodes. It will also allow to employ the physicochemical methods (XRD, XPS, SEM/TEM) to perform the post-mortem analysis of the electrode materials. This will allow to detect the changes in the materials composition and structure and provide the valuable information about degradation mechanisms.

The results of the EIS measurements in the 3-electrode configuration will be analyzed using the generalized staircase impedance model, developed in the current work. This will allow to have a deeper insight on the dependence of the electrochemical properties of the complex electrode materials (carbons and TMO/C composites) on the parameters of their porosity. On the other hand, the model will be also developed further in order to take into account the macrostructure of the thick deposits of the electrode materials. Ultimately, the generalized staircase model will be applied for the quantitative description of the impedance of thick electrode materials in both 3- and 2-electrode configurations.

Acknowledgments

First of all, I would like to express my deepest gratitude to the head of Electrocatalysis and Energy Conversion group of the ICPEES, **Prof. Elena R. Savinova**. During more than 15 years of our work together, she has been always giving me all the support and autonomy necessary to develop myself as an independent researcher and to work out my own scientific personality. I am both honored and privileged to work under the Elena's supervision.

I would like to thank most sincerely **Dr. Phamm-Huu Cuong**, who accepted the burden of being my garant for this work. I am also very grateful to Cuong for sparking my interest to the topic of electrode materials for EESD applications, for inviting me to participate in the projects related to this field, and for being always ready to share his experience and knowledge in the field of carbon materials.

I would like to express my appreciation to **Prof. Aziz Dinia (IPCMS, Strasbourg)**, **Dr. Frederick Favier (ICGM, Montpellier)**, **Dr. Camélia Matei Ghimbeu (IS2M, Mulhouse)** and **Prof. Philippe Serp (ENCI-ACET, Toulouse)** for their acceptance of being the members of my jury, for their attention to my work.

This work would not be possible without active participation of other members of ICPEES. I am grateful to **Dr. Gwénaëlle Kérangueven** for helping me to learn ISAC synthesis and working together on the further development of this synthetic route, pioneered out by her the ICPEES. I also have a privilege to work with very skillful and helpful colleagues of the group of Dr. Pham-Huu, namely **Housseinou Ba** and **Lai Truong Phuoc**, who are always ready to help, to share the ideas and their knowledge of carbon materials.

I am grateful to **Thierry Romero** for all the sessions of SEM/TEM analysis of our complicated samples. The analysis of our samples by XRD would not be possible without guidance of **Dr. Thierry Dintzer**, who is also always very

helpful and creative in solving all the problems related to informatics and fitness.

By this work I am strongly indebted to **Dr. Nina Shokina**, my wife. She has supported and helped me throughout the whole long period of the preparation of this work. She has also significantly contributed to this work. An excellent mathematician, she worked out and programmed the algorithm of the calculations by the generalized staircase model. This important part of my work would not be possible without her impact. She has also gladly volunteered to undertake a huge work on testing and improving the comprehensibility of the text of my thesis.

Finally, I would like to express my everlasting gratitude to my first tutor after my PhD, **Prof. Dr. Thomas Wandlowski**, who died too soon in the summer of 2015 at the age of 57. Besides having strongest impact on my development as a chemist and a researcher, Thomas was also a very devoted and honest friend, which will never be forgotten.

Bibliography

- [1] P. Simon and Y. Gogotsi, “Materials for electrochemical capacitors.,” *Nature materials*, vol. 7, pp. 845–54, nov 2008.
- [2] M. S. Whittingham and T. Zawodzinski, “Introduction: Batteries and Fuel Cells,” *Chemical Reviews*, vol. 104, pp. 4243–4244, oct 2004.
- [3] M. Noked, A. Soffer, and D. Arubach, “The electrochemistry of activated carbonaceous materials: Past, present, and future,” *Journal of Solid State Electrochemistry*, vol. 15, no. 7, pp. 1563–1578, 2011.
- [4] H. Lu and X. S. Zhao, “Biomass-derived carbon electrode materials for supercapacitors,” *Sustainable Energy and Fuels*, vol. 1, no. 6, pp. 1265–1281, 2017.
- [5] Q. Ke and J. Wang, “Graphene-based Materials for Supercapacitor Electrodes - A Review,” *Journal of Materiomics*, vol. 2, no. 1, pp. 37–54, 2016.
- [6] Y. Sun, Q. Wu, and G. Shi, “Graphene based new energy materials,” *Energy & Environmental Science*, vol. 4, no. 4, p. 1113, 2011.
- [7] L. L. Zhang, R. Zhou, and X. S. Zhao, “Carbon-based materials as supercapacitor electrodes,” *Journal of Materials Chemistry*, vol. 38, no. 29, pp. 2520–2531, 2009.
- [8] P. Simon, Y. Gogotsi, and B. Dunn, “Where Do Batteries End and Supercapacitors Begin?,” *Science*, vol. 343, no. 6176, pp. 1210–1211, 2014.
- [9] G. Wang, L. Zhang, and J. Zhang, “A review of electrode materials for electrochemical supercapacitors.,” *Chemical Society reviews*, vol. 41, pp. 797–828, jan 2012.

- [10] H. Ba, W. Wang, S. Pronkin, T. Romero, W. Baaziz, L. Nguyen-Dinh, W. Chu, O. Ersen, and C. Pham-Huu, “Biosourced Foam-Like Activated Carbon Materials as High-Performance Supercapacitors,” *Advanced Sustainable Systems*, vol. 1700123, p. 1700123, 2018.
- [11] H. Ba, W. Wang, G. Tuci, S. N. Pronkin, C. Weinberg, L. Nguyen-Dinh, G. Giambastiani, and C. Pham-Huu, “Tridimensional few-layer graphene-like structures from sugar-salt mixtures as high-performance supercapacitor electrodes,” *Materials Today Energy*, vol. 10, pp. 118–125, 2018.
- [12] E. Pardieu, S. Pronkin, M. Dolci, T. Dintzer, B. P. Pichon, D. Begin, C. Pham-Huu, P. Schaaf, S. Begin-Colin, and F. Boulmedais, “Hybrid layer-by-layer composites based on a conducting polyelectrolyte and Fe₃O₄ nanostructures grafted onto graphene for supercapacitor application,” *J. Mater. Chem. A*, vol. 3, pp. 22877–22885, 2015.
- [13] G. Kéranguéven, J. Faye, and S. N. P. Royer, Sébastien and, “Electrochemical properties and capacitance of Hausmannite Mn₃O₄ – carbon composite synthesized by in situ autocombustion method,” *Electrochimica Acta*, vol. 222, pp. 755–764, 2016.
- [14] E. E. Agency, “Overview of electricity production and use in Europe — European Environment Agency,” tech. rep., 2015.
- [15] K. Hansen, C. Breyer, and H. Lund, “Status and Perspectives on 100% Renewable Energy Systems,” *Energy*, vol. 175, pp. 471–480, 2019.
- [16] M. Diesendorf and B. Elliston, “The feasibility of 100% renewable electricity systems: A response to critics,” *Renewable and Sustainable Energy Reviews*, vol. 93, no. October 2017, pp. 318–330, 2018.
- [17] N. C. Figueiredo and P. P. da Silva, “The “Merit-order effect” of wind and solar power: Volatility and determinants,” *Renewable and Sustainable Energy Reviews*, vol. 102, no. November 2018, pp. 54–62, 2019.
- [18] C. Liu, F. Li, L.-P. Ma, and H.-M. Cheng, “Advanced materials for energy storage,” *Advanced materials (Deerfield Beach, Fla.)*, vol. 22, pp. E28–62, feb 2010.

- [19] Y. Gogotsi and P. Simon, “True Performance Metrics in Electrochemical Energy Storage,” *Science (New York, N.Y.)*, vol. 334, no. November, pp. 917–918, 2011.
- [20] J. Perrin and B. Multon, “Le stockage de l’énergie pour le vecteur électricité,” in *Colloque CNRS Energie*, (Montpellier), pp. 66–68, 2011.
- [21] W. Zuo, R. Li, C. Zhou, Y. Li, J. Xia, and J. Liu, “Battery-Supercapacitor Hybrid Devices: Recent Progress and Future Prospects,” *Advanced Science*, vol. 4, no. 7, pp. 1–21, 2017.
- [22] A. González, E. Goikolea, J. A. Barrena, and R. Mysyk, “Review on supercapacitors: Technologies and materials,” *Renewable and Sustainable Energy Reviews*, vol. 58, pp. 1189–1206, 2016.
- [23] B. B. Damaskin, O. A. Petrii, and G. A. Tsirlina, “Razvitie modelnykh predstavleniy o stroenii dvoynogo elektricheskogo sloya,” in *Elektrokhimiya*, pp. 350–353, Khimiya, 2001.
- [24] A. J. Bard and L. R. Faulkner, *Electrochemical methods, fundamentals and applications*, vol. 60. John Wiley and Sons Inc., 2nd ed., 2009.
- [25] T. Pajkossy, T. Wandlowski, and D. M. Kolb, “Impedance aspects of anion adsorption on gold single crystal electrodes,” *Journal of Electroanalytical Chemistry*, vol. 414, pp. 209–220, jan 1996.
- [26] J. Chmiola, P. L. T. Celine Largeot, P. Simon, and Y. Gogotsi, “Monolithic carbide-derived carbon films for micro-supercapacitors,” *Science*, vol. 328, no. 5977, pp. 480–483, 2010.
- [27] A. Lewandowski, A. Olejniczak, M. Galinski, and I. Stepniak, “Performance of carbon-carbon supercapacitors based on organic, aqueous and ionic liquid electrolytes,” *Journal of Power Sources*, vol. 195, no. 17, pp. 5814–5819, 2010.
- [28] H. Ji, X. Zhao, Z. Qiao, J. Jung, Y. Zhu, Y. Lu, L. L. Zhang, A. H. MacDonald, and R. S. Ruoff, “Capacitance of carbon-based electrical double-layer capacitors,” *Nature Communications*, vol. 5, no. 3317, pp. 1–7, 2014.

- [29] K. Kinoshita and J. A. Bett, “Potentiodynamic analysis of surface oxides on carbon blacks,” *Carbon*, vol. 11, no. 4, pp. 403–411, 1973.
- [30] A. Borenstein, O. Hanna, R. Attias, S. Luski, T. Brousse, and D. Aurbach, “Carbon-based composite materials for supercapacitor electrodes: A review,” *Journal of Materials Chemistry A*, vol. 5, no. 25, pp. 12653–12672, 2017.
- [31] M. J. Mostazo-López, R. Ruiz-Rosas, E. Morallón, and D. Cazorla-Amorós, “Generation of nitrogen functionalities on activated carbons by amidation reactions and Hofmann rearrangement: Chemical and electrochemical characterization,” 2015.
- [32] T. Kwon, H. Nishihara, H. Itoi, Q. H. Yang, and T. Kyotani, “Enhancement mechanism of electrochemical capacitance in nitrogen-boron-doped carbons with uniform straight nanochannels,” *Langmuir*, vol. 25, no. 19, pp. 11961–11968, 2009.
- [33] Z. R. Ismagilov, A. E. Shalagina, O. Y. Podyacheva, A. V. Ischenko, L. S. Kibis, A. I. Boronin, Y. A. Chesalov, D. I. Kochubey, A. I. Romanenko, O. B. Anikeeva, T. I. Buryakov, and E. N. Tkachev, “Structure and electrical conductivity of nitrogen-doped carbon nanofibers,” *Carbon*, vol. 47, no. 8, pp. 1922–1929, 2009.
- [34] Q. Wei, X. Tong, G. Zhang, J. Qiao, Q. Gong, and S. Sun, “Nitrogen-doped carbon nanotube and graphene materials for oxygen reduction reactions,” *Catalysts*, vol. 5, no. 3, pp. 1574–1602, 2015.
- [35] K. Gao, B. Wang, L. Tao, B. V. Cunniff, Z. Zhang, S. Wang, R. S. Ruoff, and L. Qu, “Efficient Metal-Free Electrocatalysts from N-Doped Carbon Nanomaterials: Mono-Doping and Co-Doping,” *Advanced Materials*, vol. 31, no. 13, pp. 1–11, 2019.
- [36] M. Inagaki, M. Toyoda, Y. Soneda, and T. Morishita, “Nitrogen-doped carbon materials,” *Carbon*, vol. 132, pp. 104–140, 2018.
- [37] Y. M. Volfkovich, D. A. Bograchev, A. A. Mikhailin, and V. S. Bagotsky, “Supercapacitor carbon electrodes with high capacitance,” *Journal of Solid State Electrochemistry*, vol. 18, no. 5, pp. 1351–1363, 2014.

- [38] Y. M. Volfkovich, D. A. Bograchev, A. Y. Rychagov, V. E. Sosenkin, and M. Y. Chaika, “Supercapacitors with carbon electrodes. Energy efficiency: modeling and experimental verification,” *Journal of Solid State Electrochemistry*, vol. 19, no. 9, pp. 2771–2779, 2015.
- [39] M. D. Levi and D. Aurbach, “Diffusion coefficients of lithium ions during intercalation into graphite derived from the simultaneous measurements and modeling of electrochemical impedance and potentiostatic intermittent titration characteristics of thin graphite electrodes,” *Journal of Physical Chemistry B*, vol. 101, no. 23, pp. 4641–4647, 1997.
- [40] M. D. Levi and D. Aurbach, “Frumkin intercalation isotherm - a tool for the description of lithium insertion into host materials: a review,” *Electrochimica Acta*, vol. 45, no. 1, pp. 167–185, 1999.
- [41] B. E. Conway, V. Birss, and J. Wojtowicz, “The role and utilization of pseudocapacitance for energy storage by supercapacitors,” *Journal of Power Sources*, vol. 66, no. 1–2, pp. 1–14, 1997.
- [42] T. Brousse, D. Bélanger, J. W. Long, D. Belanger, and J. W. Long, “To Be or Not To Be Pseudocapacitive?,” *J. Electrochemical Soc.*, vol. 162, no. 5, pp. A5185–A5189, 2015.
- [43] Y. Zhang, H. Feng, X. Wu, L. Wang, A. Zhang, T. Xia, H. Dong, X. Li, and L. Zhang, “Progress of electrochemical capacitor electrode materials: A review,” *International Journal of Hydrogen Energy*, vol. 34, pp. 4889–4899, jun 2009.
- [44] J. P. Zheng, “The Limitations of Energy Density for Electrochemical Capacitors,” *Journal of The Electrochemical Society*, vol. 144, no. 6, p. 2026, 1997.
- [45] J. M. Tarascon and M. Armand, “Issues and challenges facing rechargeable lithium batteries,” *Nature*, vol. 414, pp. 359–67, nov 2001.
- [46] L. E. Helseth, “Comparison of methods for finding the capacitance of a supercapacitor,” *Journal of Energy Storage*, vol. 35, no. December 2020, p. 102304, 2021.

- [47] D. D. MacDonald, "Reflections on the history of electrochemical impedance spectroscopy," *Electrochimica Acta*, vol. 51, no. 8-9, pp. 1376–1388, 2006.
- [48] L. Lopez, Y. Kim, L. Jierry, J. Hemmerle, F. Boulmedais, P. Schaaf, S. Pronkin, and N. A. Kotov, "Electrochemistry on Stretchable Nanocomposite Electrodes: Dependence on Strain," *ACS Nano*, vol. 12, no. 9, pp. 9223–9232, 2018.
- [49] F. Prieto, J. Alvarez-Malmagro, and M. Rueda, "Electrochemical Impedance Spectroscopy study of the adsorption of adenine on Au(111) electrodes as a function of the pH," *Journal of Electroanalytical Chemistry*, vol. 793, no. 111, pp. 209–217, 2017.
- [50] R. de Levie, "On the impedance of electrodes with rough interfaces," *Journal of Electroanalytical Chemistry*, vol. 261, no. 1, pp. 1–9, 1989.
- [51] Z. Kerner and T. Pajkossy, "On the origin of capacitance dispersion of rough electrodes," *Electrochimica Acta*, vol. 46, pp. 207–211, nov 2000.
- [52] C. L. Alexander, B. Tribollet, V. Vivier, and M. E. Orazem, "Contribution of Surface Distributions to Constant-Phase-Element (CPE) Behavior: 1. Influence of Roughness," *Electrochimica Acta*, vol. 251, pp. 416–424, 2017.
- [53] C. L. Alexander, B. Tribollet, V. Vivier, and M. E. Orazem, "Contribution of Surface Distributions to Constant-Phase-Element (CPE) Behavior: 2. Capacitance," *Electrochimica Acta*, vol. 251, pp. 566–573, 2017.
- [54] C. L. Alexander, B. Tribollet, V. Vivier, and M. E. Orazem, "Contribution of Surface Distributions to Constant-Phase-Element (CPE) Behavior: 3. Adsorbed Intermediates," *Electrochimica Acta*, vol. 251, pp. 99–108, 2017.
- [55] H. Keiser, K. D. Beccu, and M. A. Gutjahr, "Abschätzung der porenstruktur poröser elektroden aus impedanzmessungen," *Electrochimica Acta*, vol. 21, no. 8, pp. 539–543, 1976.
- [56] J.-P. Candy, P. Fouilloux, M. Keddam, and H. Takenouti, "The characterization of porous electrodes by impedance measurements," *Electrochimica Acta*, vol. 26, no. 8, pp. 1029–1034, 1981.

- [57] M. Eikerling, A. A. Kornyshev, and E. Lust, “Optimized structure of nanoporous carbon-based double-layer capacitors,” *JOURNAL OF THE ELECTROCHEMICAL SOCIETY*, vol. 152, no. 1, pp. E24–E33, 2005.
- [58] T. Soboleva, X. Zhao, K. Malek, Z. Xie, T. Navessin, and S. Holdcroft, “On the micro-, meso-, and macroporous structures of polymer electrolyte membrane fuel cell catalyst layers,” *ACS Applied Materials and Interfaces*, vol. 2, no. 2, pp. 375–384, 2010.
- [59] M. Eikerling, “Water Management in Cathode Catalyst Layers of PEM Fuel Cells,” *Journal of The Electrochemical Society*, vol. 153, no. 3, p. E58, 2006.
- [60] J. Chmiola, G. Yushin, Y. Gogotsi, C. Portet, P. Simon, and P. Taberna, “Anomalous Increase in Carbon Capacitance at Pore Sizes Less Than 1 Nanometer,” *Science*, vol. 313, pp. 1760–1763, 2006.
- [61] L. R. Radovic, “Physicochemical Properties of Carbon Materials: A Brief Overview,” in *Carbon Materials for Catalysis* (J. L. Figueiredo and P. Serp, eds.), pp. 1–44, John Wiley & Sons Inc., 2009.
- [62] A. Pandolfo and A. Hollenkamp, “Carbon properties and their role in supercapacitors,” *Journal of Power Sources*, vol. 157, no. 1, pp. 11–27, 2006.
- [63] C. Portet, G. Yushin, and Y. Gogotsi, “Electrochemical performance of carbon onions, nanodiamonds, carbon black and multiwalled nanotubes in electrical double layer capacitors,” *Carbon*, vol. 45, no. 13, pp. 2511–2518, 2007.
- [64] H. Pan, J. Li, and Y. P. Feng, “Carbon Nanotubes for Supercapacitor,” *Nanoscale Research Letters*, vol. 5, no. 3, pp. 654–668, 2010.
- [65] H. Pan, J. Li, and Y. P. Feng, “Carbon Nanotubes for Supercapacitor,” *Nanoscale Research Letters*, vol. 5, pp. 654–668, mar 2010.
- [66] Y. Zhu, S. Murali, W. Cai, X. Li, J. W. Suk, J. R. Potts, and R. S. Ruoff, “Graphene and graphene oxide: Synthesis, properties, and applications,” *Advanced Materials*, vol. 22, no. 35, pp. 3906–3924, 2010.
- [67] K. Chen, S. Song, F. Liu, and D. Xue, “Structural design of graphene for use in electrochemical energy storage devices,” *Chemical Society Reviews*, vol. 44, no. 17, pp. 6230–6257, 2015.

- [68] S. Pei and H. M. Cheng, “The reduction of graphene oxide,” *Carbon*, vol. 50, no. 9, pp. 3210–3228, 2012.
- [69] W. S. Hummers and R. E. Offeman, “Preparation of Graphitic Oxide,” *Journal of the American Chemical Society*, vol. 80, no. 6, p. 1339, 1958.
- [70] D. C. Marcano, D. V. Kosynkin, J. M. Berlin, A. Sinitskii, Z. Sun, A. S. Slesarev, L. B. Alemany, W. Lu, and J. M. Tour, “Improved Synthesis of Graphene Oxide,” *ACS Nano*, vol. 12, no. 2, pp. 2078–2078, 2018.
- [71] F. Li and Z. Chen, “Graphene-Based Materials,” *Science*, vol. 320, no. May, pp. 1170–1171, 2013.
- [72] M. P. Lavin-Lopez, J. L. Valverde, L. Sanchez-Silva, and A. Romero, “Solvent-Based Exfoliation via Sonication of Graphitic Materials for Graphene Manufacture,” *Industrial and Engineering Chemistry Research*, vol. 55, no. 4, pp. 845–855, 2016.
- [73] L. Yang, L. Zhang, and X. Jiao, “The electrochemical performance of reduced graphene oxide prepared from different types of natural graphites,” *RSC Advances*, vol. 11, pp. 4042–4052, 2021.
- [74] A. Das, B. Chakraborty, and A. K. Sood, “Raman spectroscopy of graphene on different substrates and influence of defects,” *Bulletin of Materials Science*, vol. 31, no. 3, pp. 579–584, 2008.
- [75] V. N. Popov and P. Lambin, “Theoretical Raman intensity of the G and 2D bands of strained graphene,” *Carbon*, vol. 54, pp. 86–93, 2013.
- [76] A. Ciesielski and P. Samorì, “Graphene via sonication assisted liquid-phase exfoliation,” *Chemical Society Reviews*, vol. 43, no. 1, pp. 381–398, 2014.
- [77] A. Bittner, M. Zhu, Y. Yang, H. Waibel, M. Konuma, U. Starke, and C. Weber, “Ageing of electrochemical double layer capacitors,” *Journal of Power Sources*, vol. 203, pp. 262–273, apr 2012.
- [78] D. Ihiawakrim, O. Ersen, F. Melin, P. Hellwig, I. Janowska, D. Begin, W. Baaziz, S. Begin-Colin, C. Pham-Huu, and R. Baati, “A single-stage functionalization and exfoliation method for the production of graphene in

- water: Stepwise construction of 2D-nanostructured composites with iron oxide nanoparticles,” *Nanoscale*, vol. 5, no. 19, pp. 9073–9080, 2013.
- [79] Z. Y. Xia, S. Pezzini, E. Treossi, G. Giambastiani, F. Corticelli, V. Morandi, A. Zanelli, V. Bellani, and V. Palermo, “The exfoliation of graphene in liquids by electrochemical, chemical, and sonication-assisted techniques: A nanoscale study,” *Advanced Functional Materials*, vol. 23, no. 37, pp. 4684–4693, 2013.
- [80] Z. Fan, J. Yan, L. Zhi, Q. Zhang, T. Wei, J. Feng, M. Zhang, W. Qian, and F. Wei, “A three-dimensional carbon nanotube/graphene sandwich and its application as electrode in supercapacitors,” *Advanced Materials*, vol. 22, no. 33, pp. 3723–3728, 2010.
- [81] Q. Cheng, J. Tang, J. Ma, H. Zhang, N. Shinya, and L. C. Qin, “Graphene and carbon nanotube composite electrodes for supercapacitors with ultra-high energy density,” *Physical Chemistry Chemical Physics*, vol. 13, no. 39, pp. 17615–17624, 2011.
- [82] Q. Cheng, J. Tang, J. Ma, H. Zhang, N. Shinya, and L.-C. Qin, “Graphene and nanostructured MnO₂ composite electrodes for supercapacitors,” *Carbon*, vol. 49, pp. 2917–2925, aug 2011.
- [83] Y. Wang, Y. Wu, Y. Huang, F. Zhang, X. Yang, Y. Ma, and Y. Chen, “Preventing graphene sheets from restacking for high-capacitance performance,” *Journal of Physical Chemistry C*, vol. 115, no. 46, pp. 23192–23197, 2011.
- [84] P. Yu, X. Zhao, Z. Huang, Y. Li, and Q. Zhang, “Free-standing three-dimensional graphene and polyaniline nanowire arrays hybrid foams for high-performance flexible and lightweight supercapacitors,” *J. Mater. Chem. A*, vol. 2, no. 35, pp. 14413–14420, 2014.
- [85] H. Wang, X. Sun, Z. Liu, and Z. Lei, “Creation of nanopores on graphene planes with MgO template for preparing high-performance supercapacitor electrodes,” *Nanoscale*, vol. 6, no. 12, pp. 6577–6584, 2014.
- [86] J. Yan, Q. Wang, T. Wei, L. Jiang, M. Zhang, X. Jing, and Z. Fan, “Template-Assisted low temperature synthesis of functionalized graphene for

- ultrahigh volumetric performance supercapacitors,” *ACS Nano*, vol. 8, no. 5, pp. 4720–4729, 2014.
- [87] L. Wei and G. Yushin, “Nanostructured activated carbons from natural precursors for electrical double layer capacitors,” *Nano Energy*, vol. 1, no. 4, pp. 552–565, 2012.
- [88] S. Yoo, S. S. Kelley, D. C. Tilotta, and S. Park, “Structural Characterization of Loblolly Pine Derived Biochar by X-ray Diffraction and Electron Energy Loss Spectroscopy,” *ACS Sustainable Chemistry and Engineering*, vol. 6, no. 2, pp. 2621–2629, 2018.
- [89] C. Senthil and C. W. Lee, “Biomass-derived biochar materials as sustainable energy sources for electrochemical energy storage devices,” *Renewable and Sustainable Energy Reviews*, vol. 137, no. xxxx, p. 110464, 2021.
- [90] Y. Zhang, Z. Gao, N. Song, and X. Li, “High-performance supercapacitors and batteries derived from activated banana-peel with porous structures,” *Electrochimica Acta*, vol. 222, pp. 1257–1266, 2016.
- [91] H. Y. Lee and J. B. Goodenough, “Supercapacitor Behavior with KCl Electrolyte,” *Journal of Solid State Chemistry*, vol. 223, pp. 220–223, 1999.
- [92] M. Majumder, R. B. Choudhary, and A. K. Thakur, “Hemispherical nitrogen-doped carbon spheres integrated with polyindole as high performance electrode material for supercapacitor applications,” 2019.
- [93] P. Cox, *Transition Metal Oxides. An introduction to their electronic structure and properties*. 1992.
- [94] S. I. Dutch, “Periodic Tables of Elemental Abundance,” *Journal of Chemical Education*, vol. 76, no. 3, pp. 356–358, 1999.
- [95] M. M. Thackeray, “Manganese oxides for lithium batteries,” *Progress in Solid State Chemistry*, vol. 25, no. 1-2, pp. 1–71, 1997.
- [96] C. De Las Casas and W. Li, “A review of application of carbon nanotubes for lithium ion battery anode material,” *Journal of Power Sources*, vol. 208, pp. 74–85, 2012.

- [97] D. Adler, “Mechanisms for metal-nonmetal transitions in transition-metal oxides and sulfides,” *Reviews of Modern Physics*, vol. 40, no. 4, pp. 714–736, 1968.
- [98] L. M. Falicov and B. Koiller, “Low temperature conductivity of transition-metal oxides,” *Journal of Solid State Chemistry*, vol. 12, no. 3-4, pp. 349–354, 1975.
- [99] C. Sanchez, R. Morineau, and J. Livage, “Electrical conductivity of amorphous V₂O₅,” *Physica Status Solidi (a)*, vol. 76, no. 2, pp. 661–666, 1983.
- [100] S. Walia, S. Balendhran, H. Nili, S. Zhuiykov, G. Rosengarten, Q. H. Wang, M. Bhaskaran, S. Sriram, M. S. Strano, and K. Kalantar-zadeh, “Transition metal oxides - Thermoelectric properties,” *Progress in Materials Science*, vol. 58, no. 8, pp. 1443–1489, 2013.
- [101] J. R. Smith and F. C. Walsh, “Electrodes based on Magnelli phase titanium oxide: the properties and applications of Ebonex (R) materials,” *Journal of Applied Electrochemistry*, vol. 28, no. 50, pp. 1021–1033, 1998.
- [102] J. Kang, A. Hirata, L. Kang, X. Zhang, Y. Hou, L. Chen, C. Li, T. Fujita, K. Akagi, and M. Chen, “Enhanced supercapacitor performance of MnO₂ by atomic doping,” *Angewandte Chemie - International Edition*, vol. 52, no. 6, pp. 1664–1667, 2013.
- [103] O. Ghodbane, J. L. Pascal, and F. Favier, “Microstructural effects on charge-storage properties in MnO₂-based electrochemical supercapacitors,” *ACS Applied Materials and Interfaces*, vol. 1, no. 5, pp. 1130–1139, 2009.
- [104] M. Toupin, T. Brousse, and D. Belanger, “Influence of Microstructure on the Charge Storage Properties of Chemically Synthesized Manganese Dioxide,” *Chemistry of Materials*, vol. 14, no. 9, pp. 3946–3952, 2002.
- [105] E. Beaudrouet, a. Le Gal La Salle, and D. Guyomard, “Nanostructured manganese dioxides: Synthesis and properties as supercapacitor electrode materials,” *Electrochimica Acta*, vol. 54, no. 4, pp. 1240–1248, 2009.
- [106] M. Pourbaix, *Atlas of electrochemical equilibria in aqueous solutions*. NACE International Cebelcor, 1974.

- [107] M. Łukaszewski, A. Zurowski, and A. Czerwiński, “Hydrogen in thin Pd-based layers deposited on reticulated vitreous carbon-A new system for electrochemical capacitors,” *Journal of Power Sources*, vol. 185, no. 2, pp. 1598–1604, 2008.
- [108] R. Feser, “Uniform Corrosion of Metals in Acid, Neutral and Alkaline Electrolytes,” in *Encyclopedia of Electrochemistry, v.4, Corrosion and Oxide Films*, ch. 2.1., p. 67, Wiley VCH, 2006.
- [109] C. Lokhande, T. Gujar, V. Shinde, R. S. Mane, and S.-H. Han, “Electrochemical supercapacitor application of perovskite thin films,” *Electrochemistry Communications*, vol. 9, pp. 1805–1809, jul 2007.
- [110] Q. Li, S. Zheng, Y. Xu, H. Xue, and H. Pang, “Ruthenium based materials as electrode materials for supercapacitors,” *Chemical Engineering Journal*, vol. 333, no. August 2017, pp. 505–518, 2018.
- [111] W. D. Ryden, A. W. Lawson, and C. C. Sartain, “Electrical transport properties of IrO₂ and RuO₂,” *Physical Review B*, vol. 1, no. 4, pp. 1494–1500, 1970.
- [112] L. F. Mattheiss, “Electronic structure of RuO₂, OsO₂, and IrO₂,” *Physical Review B*, vol. 13, no. 6, pp. 2433–2450, 1976.
- [113] Y.-Z. Zheng, H.-Y. Ding, and M.-L. Zhang, “Hydrous-ruthenium-oxide thin film electrodes prepared by cathodic electrodeposition for supercapacitors,” *Thin Solid Films*, vol. 516, pp. 7381–7385, sep 2008.
- [114] I.-H. Kim, J.-H. Kim, Y.-H. Lee, and K.-B. Kim, “Synthesis and Characterization of Electrochemically Prepared Ruthenium Oxide on Carbon Nanotube Film Substrate for Supercapacitor Applications,” *Journal of The Electrochemical Society*, vol. 152, no. 11, p. A2170, 2005.
- [115] B.-o. Park, C. Lokhande, H.-s. Park, K.-D. Jung, and O.-S. Joo, “Electrodeposited ruthenium oxide (RuO₂) films for electrochemical supercapacitors,” *Journal of Materials Science*, vol. 9, pp. 4313–4317, 2004.
- [116] H. Li, R. Wang, and R. Cao, “Physical and electrochemical characterization of hydrous ruthenium oxide/ordered mesoporous carbon composites as su-

- percapacitor,” *Microporous and Mesoporous Materials*, vol. 111, pp. 32–38, apr 2008.
- [117] D. V. Bavykin, J. M. Friedrich, and F. C. Walsh, “Protonated Titanates and TiO₂ Nanostructured Materials: Synthesis, Properties, and Applications,” *Advanced Materials*, vol. 18, pp. 2807–2824, nov 2006.
- [118] F. Fabregat-santiago, I. Mora-sero, and J. Bisquert, “Cyclic Voltammetry Studies of Nanoporous Semiconductors . Capacitive and Reactive Properties of Nanocrystalline TiO₂ Electrodes in Aqueous Electrolyte,” *J. Phys. Chem. B*, vol. 107, pp. 758–768, 2003.
- [119] J. M. Macak, L. V. Taveira, H. Tsuchiya, K. Sirotna, J. Macak, and P. Schmuki, “Influence of different fluoride containing electrolytes on the formation of self-organized titania nanotubes by Ti anodization,” *Journal of Electroceramics*, vol. 16, no. 1, pp. 29–34, 2006.
- [120] S. Yoriya, G. K. Mor, S. Sharma, and C. A. Grimes, “Synthesis of ordered arrays of discrete, partially crystalline titania nanotubes by Ti anodization using diethylene glycol electrolytes,” *Journal of Materials Chemistry*, vol. 18, no. 28, pp. 3332–3336, 2008.
- [121] T. Cottineau, N. Béalu, P. A. Gross, S. N. Pronkin, N. Keller, E. R. Savinova, and V. Keller, “One step synthesis of niobium doped titania nanotube arrays to form (N,Nb) co-doped TiO₂ with high visible light photoelectrochemical activity,” *Journal of Materials Chemistry A*, vol. 1, no. 6, pp. 2151–2160, 2013.
- [122] I. Savych, J. Bernard D’Arbigny, S. Subianto, S. Cavaliere, D. J. Jones, and J. Rozière, “On the effect of non-carbon nanostructured supports on the stability of Pt nanoparticles during voltage cycling: A study of TiO₂ nanofibres,” *Journal of Power Sources*, vol. 257, pp. 147–155, 2014.
- [123] T. Favet, V. Keller, T. Cottineau, and M. A. El Khakani, “Enhanced visible-light-photoconversion efficiency of TiO₂ nanotubes decorated by pulsed laser deposited CoNi nanoparticles,” *International Journal of Hydrogen Energy*, vol. 44, no. 54, pp. 28656–28667, 2019.

- [124] F. Fabregat-Santiago, E. M. Barea, J. Bisquert, G. K. Mor, K. Shankar, and C. a. Grimes, "High carrier density and capacitance in TiO₂ nanotube arrays induced by electrochemical doping," *Journal of the American Chemical Society*, vol. 130, pp. 11312–6, aug 2008.
- [125] H. Zhang, X. Deng, X. Wu, and R. Chen, "Electrochemical fabrication and characterization of highly-ordered titania nanotube arrays," *Advanced Materials Research*, vol. 148-149, pp. 1600–1606, 2011.
- [126] M. Salari, S. H. Aboutalebi, K. Konstantinov, and H. K. Liu, "A highly ordered titania nanotube array as a supercapacitor electrode," *Physical Chemistry Chemical Physics*, vol. 13, no. 11, pp. 5038–5041, 2011.
- [127] J. Yang, L. Lian, P. Xiong, and M. Wei, "Pseudo-capacitive performance of titanate nanotubes as a supercapacitor electrode," *Chemical Communications*, vol. 50, no. 45, pp. 5973–5975, 2014.
- [128] R. A. Aziz, I. I. Misnon, K. F. Chong, M. M. Yusoff, and R. Jose, "Layered sodium titanate nanostructures as a new electrode for high energy density supercapacitors," *Electrochimica Acta*, vol. 113, pp. 141–148, 2013.
- [129] M. Gillet, K. Aguir, C. Lemire, E. Gillet, and K. Schierbaum, "The structure and electrical conductivity of vacuum-annealed WO₃ thin films," *Thin Solid Films*, vol. 467, no. 1-2, pp. 239–246, 2004.
- [130] H. Peng, G. Ma, K. Sun, J. Mu, M. Luo, and Z. Lei, "High-performance aqueous asymmetric supercapacitor based on carbon nanofibers network and tungsten trioxide nanorod bundles electrodes," *Electrochimica Acta*, vol. 147, pp. 54–61, 2014.
- [131] S. Yoon, E. Kang, J. Kon Kim, C. Wee Lee, and J. Lee, "Development of high-performance supercapacitor electrodes using novel ordered mesoporous tungsten oxide materials with high electrical conductivity," *Chemical Communications*, vol. 47, no. 3, pp. 1021–1023, 2011.
- [132] L. L. Xing, K. J. Huang, and L. X. Fang, "Preparation of layered graphene and tungsten oxide hybrids for enhanced performance supercapacitors," *Dalton Transactions*, vol. 45, no. 43, pp. 17439–17446, 2016.

- [133] Y. Cai, Y. Wang, S. Deng, G. Chen, Q. Li, B. Han, R. Han, and Y. Wang, “Graphene nanosheets-tungsten oxides composite for supercapacitor electrode,” *Ceramics International*, vol. 40, no. 3, pp. 4109–4116, 2014.
- [134] W. Sugimoto, T. Ohnuma, Y. Murakami, and Y. Takasu, “Molybdenum oxide/carbon composite electrodes as electrochemical supercapacitors,” *Electrochemical and Solid-State Letters*, vol. 4, no. 9, pp. 145–147, 2001.
- [135] D. Hanlon, C. Backes, T. M. Higgins, M. Hughes, A. O’Neill, P. King, N. McEvoy, G. S. Duesberg, B. Mendoza Sanchez, H. Pettersson, V. Nicolosi, and J. N. Coleman, “Production of molybdenum trioxide nanosheets by liquid exfoliation and their application in high-performance supercapacitors,” *Chemistry of Materials*, vol. 26, no. 4, pp. 1751–1763, 2014.
- [136] Y. Zeng, M. Yu, Y. Meng, P. Fang, X. Lu, and Y. Tong, “Iron-Based Supercapacitor Electrodes: Advances and Challenges,” *Advanced Energy Materials*, vol. 6, no. 24, pp. 1–17, 2016.
- [137] S. Patapis, “Electrical resistivity of α -Fe₂O₃ and comparison to TEP at the first order Morin transition,” *Solid State Communications*, vol. 52, no. 11, pp. 925–928, 1984.
- [138] P. Kulal, D. Dubal, C. Lokhande, and V. Fulari, “Chemical synthesis of Fe₂O₃ thin films for supercapacitor application,” *Journal of Alloys and Compounds*, vol. 509, pp. 2567–2571, feb 2011.
- [139] C. Guan, J. Liu, Y. Wang, L. Mao, Z. Fan, Z. Shen, H. Zhang, and J. Wang, “Iron oxide-decorated carbon for supercapacitor anodes with ultrahigh energy density and outstanding cycling stability,” *ACS Nano*, vol. 9, no. 5, pp. 5198–5207, 2015.
- [140] Y. X. Zeng, Y. Han, Y. T. Zhao, Y. Zeng, M. H. Yu, Y. J. Liu, H. L. Tang, Y. X. Tong, and X. H. Lu, “Advanced Ti-Doped Fe₂O₃@PEDOT Core/Shell Anode for High-Energy Asymmetric Supercapacitors,” *Advanced Energy Materials*, vol. 5, no. 12, pp. 1–7, 2015.
- [141] D. S. Tannhauser, “Conductivity in iron oxides,” *Journal of Physics and Chemistry of Solids*, vol. 23, no. 1-2, pp. 25–34, 1962.

- [142] J. Chen, K. Huang, and S. Liu, "Hydrothermal preparation of octadecahedron Fe₃O₄ thin film for use in an electrochemical supercapacitor," *Electrochimica Acta*, vol. 55, no. 1, pp. 1–5, 2009.
- [143] E. Mitchell, R. K. Gupta, K. Mensah-Darkwa, D. Kumar, K. Ramasamy, B. K. Gupta, and P. Kahol, "Facile synthesis and morphogenesis of superparamagnetic iron oxide nanoparticles for high-performance supercapacitor applications," *New Journal of Chemistry*, vol. 38, no. 9, pp. 4344–4350, 2014.
- [144] M. Liu and J. Sun, "In situ growth of monodisperse Fe₃O₄ nanoparticles on graphene as flexible paper for supercapacitor," *Journal of Materials Chemistry A*, vol. 2, no. 30, pp. 12068–12074, 2014.
- [145] H. Antony, L. Legrand, L. Maréchal, S. Perrin, P. Dillmann, and A. Chaussé, "Study of lepidocrocite γ -FeOOH electrochemical reduction in neutral and slightly alkaline solutions at 25C," *Electrochimica Acta*, vol. 51, no. 4, pp. 745–753, 2005.
- [146] Y.-C. Chen, Y.-G. Lin, Y.-K. Hsu, S.-C. Yen, K.-H. Chen, and L.-C. Chen, "Novel Iron Oxyhydroxide Lepidocrocite Nanosheet as Ultrahigh Power Density Anode Material for Asymmetric Supercapacitors," *Small*, vol. 10, no. 18, pp. 3803–3810, 2014.
- [147] R. M. Cornell and U. Schwertmann, "Electronic, Electrical and Magnetic Properties and Colour," in *The Iron Oxides*, pp. 111–137, 2003.
- [148] Q. Shou, J. Cheng, L. Zhang, B. J. Nelson, and X. Zhang, "Synthesis and characterization of a nanocomposite of goethite nanorods and reduced graphene oxide for electrochemical capacitors," *Journal of Solid State Chemistry*, vol. 185, pp. 191–197, 2012.
- [149] H. Xu, Z. Hu, A. Lu, Y. Hu, L. Li, Y. Yang, Z. Zhang, and H. Wu, "Synthesis and super capacitance of goethite/reduced graphene oxide for supercapacitors," *Materials Chemistry and Physics*, vol. 141, no. 1, pp. 310–317, 2013.
- [150] R. Barik, B. K. Jena, and M. Mohapatra, "Metal doped mesoporous FeOOH nanorods for high performance supercapacitors," *RSC Advances*, vol. 7, no. 77, pp. 49083–49090, 2017.

- [151] W. Wei, X. Cui, W. Chen, and D. G. Ivey, "Manganese oxide-based materials as electrochemical supercapacitor electrodes," *Chem. Soc. Rev.*, vol. 40, pp. 1697–1721, mar 2011.
- [152] L. L. Zhang, T. Wei, W. Wang, and X. Zhao, "Manganese oxide–carbon composite as supercapacitor electrode materials," *Microporous and Mesoporous Materials*, vol. 123, pp. 260–267, jul 2009.
- [153] H. Pan, Y. Shao, P. Yan, Y. Cheng, K. S. Han, Z. Nie, C. Wang, J. Yang, X. Li, P. Bhattacharya, K. T. Mueller, and J. Liu, "Reversible aqueous zinc/manganese oxide energy storage from conversion reactions," *Nature Energy*, vol. 1, no. April, pp. 1–7, 2016.
- [154] M. M. Doeff, A. Anapolsky, L. Edman, T. J. Richardson, and L. C. De Jonghe, "A High-Rate Manganese Oxide for Rechargeable Lithium Battery Applications," *Journal of The Electrochemical Society*, vol. 148, no. 3, p. A230, 2001.
- [155] M. Toupin, T. Brousse, and D. Bélanger, "Charge storage mechanism of MnO₂ electrode used in aqueous electrochemical capacitor," *Chemistry of Materials*, vol. 16, no. 16, pp. 3184–3190, 2004.
- [156] T. Cottineau, M. Toupin, T. Delahaye, T. Brousse, and D. Bélanger, "Nanostructured transition metal oxides for aqueous hybrid electrochemical supercapacitors," *Applied Physics A: Materials Science and Processing*, vol. 82, pp. 599–606, nov 2005.
- [157] V. G. Bhide and R. H. Dani, "Electrical conductivity in oxides of manganese and related compounds," *Physica*, vol. 27, no. 9, pp. 821–826, 1961.
- [158] Z. Fan, J. Chen, B. Zhang, F. Sun, B. Liu, and Y. Kuang, "Electrochemically induced deposition method to prepare γ -MnO₂/multi-walled carbon nanotube composites as electrode material in supercapacitors," *Materials Research Bulletin*, vol. 43, no. 8-9, pp. 2085–2091, 2008.
- [159] Z. Fan, J. Chen, B. Zhang, B. Liu, X. Zhong, and Y. Kuang, "High dispersion of γ -MnO₂ on well-aligned carbon nanotube arrays and its application in supercapacitors," *Diamond and Related Materials*, vol. 17, no. 11, pp. 1943–1948, 2008.

- [160] T. Brousse, M. Toupin, R. Dugas, L. Athouël, O. Crosnier, and D. Bélanger, “Crystalline MnO₂ as Possible Alternatives to Amorphous Compounds in Electrochemical Supercapacitors,” *Journal of The Electrochemical Society*, vol. 153, no. 12, p. A2171, 2006.
- [161] D. A. Tompsett and M. S. Islam, “Surfaces of rutile MnO₂ are electronically conducting, whereas the bulk material is insulating,” *Journal of Physical Chemistry C*, vol. 118, no. 43, pp. 25009–25015, 2014.
- [162] X. Xie and L. Gao, “Characterization of a manganese dioxide/carbon nanotube composite fabricated using an in situ coating method,” *Carbon*, vol. 45, no. 12, pp. 2365–2373, 2007.
- [163] T. Nguyen, M. João Carmezim, M. Boudard, and M. Fátima Montemor, “Cathodic electrodeposition and electrochemical response of manganese oxide pseudocapacitor electrodes,” *International Journal of Hydrogen Energy*, vol. 40, pp. 16355–16364, dec 2015.
- [164] T. Yousefi, A. N. Golikand, M. H. Mashhadizadeh, and M. Aghazadeh, “High temperature and low current density synthesis of Mn₃O₄ porous nano spheres: Characterization and electrochemical properties,” *Current Applied Physics*, vol. 12, no. 2, pp. 544–549, 2012.
- [165] J. Jiang and A. Kucernak, “Electrochemical supercapacitor material based on manganese oxide: preparation and characterization,” *Electrochimica Acta*, vol. 47, pp. 2381–2386, jun 2002.
- [166] C.-K. Lin, K.-h. Chuang, C.-y. Lin, C.-y. Tsay, and C.-y. Chen, “Manganese oxide films prepared by sol–gel process for supercapacitor application,” *Surface and Coatings Technology*, vol. 202, pp. 1272–1276, 2007.
- [167] T. Tsumura, K. Tsumori, G. Shimizu, and M. Toyoda, “Electrochemical properties of spinel-type manganese oxide/porous carbon nanocomposite powders in 1 M KOH aqueous solution,” *Journal of Physics and Chemistry of Solids*, vol. 73, no. 2, pp. 237–244, 2012.
- [168] K. C. Patil, S. T. Aruna, and T. Mimani, “Combustion synthesis: An update,” *Current Opinion in Solid State and Materials Science*, vol. 6, no. 6, pp. 507–512, 2002.

- [169] S. T. Aruna and A. S. Mukasyan, "Combustion synthesis and nanomaterials," *Current Opinion in Solid State and Materials Science*, vol. 12, no. 3-4, pp. 44–50, 2008.
- [170] A. Varma, A. S. Mukasyan, A. S. Rogachev, and K. V. Manukyan, "Solution Combustion Synthesis of Nanoscale Materials," *Chemical Reviews*, vol. 116, no. 23, pp. 14493–14586, 2016.
- [171] G. Kéranguéven, S. Royer, and E. Savinova, "Synthesis of efficient Vulcan-LaMnO₃ perovskite nanocomposite for the oxygen reduction reaction," *Electrochemistry Communications*, vol. 50, pp. 28–31, 2015.
- [172] K. Deori, S. K. Ujjain, R. K. Sharma, and S. Deka, "Morphology controlled synthesis of nanoporous Co₃O₄ nanostructures and their charge storage characteristics in supercapacitors," *ACS Applied Materials and Interfaces*, vol. 5, no. 21, pp. 10665–10672, 2013.
- [173] D. Guan, Z. Gao, W. Yang, J. Wang, Y. Yuan, B. Wang, M. Zhang, and L. Liu, "Hydrothermal synthesis of carbon nanotube/cubic Fe₃O₄ nanocomposite for enhanced performance supercapacitor electrode material," *Materials Science and Engineering B: Solid-State Materials for Advanced Technology*, vol. 178, no. 10, pp. 736–743, 2013.
- [174] A. Petric and H. Ling, "Electrical conductivity and thermal expansion of spinels at elevated temperatures," *Journal of the American Ceramic Society*, vol. 90, no. 5, pp. 1515–1520, 2007.
- [175] W. Xia, A. Mahmood, Z. Liang, R. Zou, and S. Guo, "Earth-Abundant Nanomaterials for Oxygen Reduction," *Angewandte Chemie - International Edition*, vol. 55, no. 8, pp. 2650–2676, 2016.
- [176] P. R. Garcês Gonçalves, H. A. De Abreu, and H. A. Duarte, "Stability, Structural, and Electronic Properties of Hausmannite (Mn₃O₄) Surfaces and Their Interaction with Water," *Journal of Physical Chemistry C*, vol. 122, no. 36, pp. 20841–20849, 2018.
- [177] H. Zhu, S. Zhang, Y.-x. Huang, L. Wu, and S. Sun, "Monodisperse MxFe_{3-x}O₄ (M=Fe,Cu,Co,Mn) Nanoparticles and Their Electrocatalysis for Oxygen Reduction Reaction," *Nano letters*, vol. 4, pp. 3–7, 2013.

- [178] Y. Liang, H. Wang, J. Zhou, Y. Li, J. Wang, T. Regier, and H. Dai, "Covalent hybrid of spinel manganese-cobalt oxide and graphene as advanced oxygen reduction electrocatalysts," *Journal of the American Chemical Society*, vol. 134, no. 7, pp. 3517–3523, 2012.
- [179] A. M. Abioye and F. N. Ani, "Recent development in the production of activated carbon electrodes from agricultural waste biomass for supercapacitors: A review," *Renewable and Sustainable Energy Reviews*, vol. 52, pp. 1282–1293, 2015.
- [180] E. Koseolu and C. Akmil-Bacsar, "Preparation, structural evaluation and adsorptive properties of activated carbon from agricultural waste biomass," *Advanced Powder Technology*, vol. 26, no. 3, pp. 811–818, 2015.
- [181] K. S. Ukanwa, K. Patchigolla, R. Sakrabani, E. Anthony, and S. Mandavgane, "A review of chemicals to produce activated carbon from agricultural waste biomass," *Sustainability (Switzerland)*, vol. 11, no. 22, pp. 1–35, 2019.
- [182] B. J. Rani, M. Ravina, G. Ravi, S. Ravichandran, V. Ganesh, and R. Yuvakkumar, "Synthesis and characterization of hausmannite (Mn₃O₄) nanostructures," *Surfaces and Interfaces*, vol. 11, no. July 2017, pp. 28–36, 2018.
- [183] H. U. Shah, F. Wang, A. M. Toufiq, S. Ali, Z. U. H. Khan, Y. Li, J. Hu, and K. He, "Electrochemical properties of controlled size Mn₃O₄ nanoparticles for supercapacitor applications," *Journal of Nanoscience and Nanotechnology*, vol. 18, no. 1, pp. 719–724, 2018.
- [184] S. L. Kuo and N. L. Wu, "Electrochemical characterization on MnFe₂O₄/carbon black composite aqueous supercapacitors," *Journal of Power Sources*, vol. 162, no. 2 SPEC. ISS., pp. 1437–1443, 2006.
- [185] S.-L. Kuo, J.-F. Lee, and N.-L. Wu, "Study on Pseudocapacitance Mechanism of Aqueous MnFe₂O₄ Supercapacitor," *Journal of The Electrochemical Society*, vol. 154, no. 1, p. A34, 2007.
- [186] B. Li, Y. Fu, H. Xia, and X. Wang, "High-performance asymmetric supercapacitors based on MnFe₂O₄/graphene nanocomposite as anode material," *Materials Letters*, vol. 122, pp. 193–196, 2014.